Doctoral Dissertation
Doctoral Program in Electrical, Electronics and Communications Engineering
(33.rd cycle)

Physical Layer Aware Open Optical Networking

Alessio Ferrari
* * * * * *

Supervisor
Prof. Vittorio Curri

Doctoral Examination Committee:
Prof. Erik Agrell, Referee, Chalmers University of Technology
Prof. Robert Killey, Referee, University College of London
Dr. Davide Calonico, INRIM
Dr. Filippo Cugini, CNIT
Dr. Florian Frank, Orange Labs

Politecnico di Torino
2021

I hereby declare that, the contents and organisation of this dissertation constitute my own original work and does not compromise in any way the rights of third parties, including those relating to the security of personal data.

. . . . . .

Alessio Ferrari

Turin, 2021

Summary

This thesis discusses the topic of physical layer aware open optical networking.

Modern optical communications involve transparent networks where the optical signals travel through intermediate nodes without being received and retransmitted, i.e. without being regenerated. In this context, the physical layer cannot be approached as a simple set of point-to-point optical connections but a holistic approach that considers the entire network is necessary. In this framework, the telecom operators target the reduction of the costs while maximizing the network capacity. For this reason, they are pushing the market towards open and disaggregated solutions where the equipment is compatible with open and standard APIs. For the same reason, promising solutions such as multi-band transmission are under investigations as they enable a capacity upgrade without deploying new fiber cables. Additionally, online and offline network analysis tools able to provide the meaningful performance metrics are fundamental to effectively tackle the network design. Finally, the automation of the network operations is an essential aspect of the network management as it allows a reliable and scalable management of the infrastructure.

The second chapter provides the theoretical background over which the rest of the thesis is structured. In detail, the physical modelling of the network elements is provided and the methodology for evaluating the generalized signal-to-noise ratio is described. Moreover, the impairment-aware network abstraction is introduced to represent the physical layer of a network. Finally, the basics of routing and wavelength assignment are summarized.

Based on this, GNPy, an open source quality-of-transmission estimator (QoT-E), is introduced and described. Then, the most significant experimental validation campaigns have been reported: the validation over a commercial line system hosted in the Microsoft labs and the subsequent validation over a segment of the Microsoft core network.

In the following chapter, the multi-band transmission has been investigated and analyzed. Such a technology raises the interest of the operators as it targets the increase of the capacity by extending number of channels transmitted along the same fiber without requiring the deployment of new fibers and, therefore, reducing the costs of a capacity upgrade. In this thesis, a simple but effective power optimization

strategy aiming at improving the quality-of-transmission has been proposed. Then, the capacity of a fully loaded multi-band communication considering several applications (data center interconnect, metro and regional networks) has been assessed. The outcomes show how multi-band transmission can potentially accommodate 7 to 10 times more traffic than a state-of-the-art single-band C-band line system.

Subsequently, two network design tools have been introduced: an offline physical layer assessment (OPLA) tool and a statistical network assessment process (SNAP). In detail, the OPLA tool has been adopted to address some infrastructural upgrades to effectively increase the network capacity and to reduce the regenerators deployed in the network and therefore the costs. Then, SNAP has been used to compare the network benefit of several SDM solutions and multi-band transmission.

Lastly, a QoT-E has been integrated into the ProNET network orchestrator in order to enable a physical layer aware automation while the orchestrator operates the network. This integration has been experimentally validated as well.

Acknowledgements

This thesis and all the work behind it would not be possible without the support and help of many individuals, to which I would like to extend a heartfelt gratitude.

Fist, I would like to express my deep and sincere gratitude to my supervisor Vittorio Curri for having given me the opportunity to enjoy the unique experience that the PhD provides. Beyond having taught me all the technical knowledge, he trusted me, recognized my abilities and my potential, and was a real leader as well as a mentor.I am very grateful to him for the unique research environment in which I had the opportunity to thrive. Then, I want to warmly thank Mattia Cantono for being a colleague as well as an example to follow. In addiction, I am thankful to all my fellow colleagues for their friendship and all the moments that we shared together, in particular to Dario Pilori, Emanuele Virgillito, Ihtesham Khan, Andrea D'Amico, Giacomo Borraccini, Elliot London, Rasoul Sadeghi and Bruno Vinícius. I wish to thank the entire OptCom group and the Links Foundation team for their passion for research and for all the stimulating discussions that we had. I want also to thank all the members of the OSA student chapter Torino for all the amazing experiences that we shared.

My gratitude goes, as well, to all the people with whom I collaborated through these years from external organizations and companies, and in particular to the Cisco team, the PSE working group, the Microsoft team, Antonio Napoli and all the Infinera team, the OpNeAR team in UT-Dallas, and to Nicola Sambo.

A special thanks goes to my long-term friends Lorenzo, Michele, Giammarco, Nicholas and Luchas for all the carefree moments spent together. I warmly would like to share my gratitude toward Giovanni for all of his support and for the infinite number of hints that he gave me. I want to thank all my family for all the support and the trust, and the family of Valeria for being a second family in Torino.

I am so grateful for the unconditional love of my dog Bender.

Last and most important is Valeria with whom I have been sharing my life. I feel lucky for having met her and for the love we have for each other. I am also deeply grateful for all her support, and I want to thank her for being always present.

Contents

List of Tables IX

List of Figures X

List of Abbreviations XVII

List of Scientific Contributions XVIII
Peer-Reviewed International Journals xviii
International Conferences xix
Activities and Collaborations xxii

1 Introduction 1

2 An introduction to the network optical layer 5
2.1 Modelling the physical layer of an optical network 5
2.1.1 The transmitter 5
2.1.2 Modelling the amplifier propagation 7
2.1.3 Modelling the fiber propagation 8
2.1.4 Modelling the ROADM 12
2.1.5 The receiver 13
2.1.6 An impairment-aware network abstraction 15
2.2 Routing and wavelength assignment 16
2.3 Outline of the remainder of the thesis 17

3 GNPy: an open source software to abstract Open Optical Networks 19
3.1 General Structure of GNPy 20
3.2 Simulative validation through split-step simulation 22
3.2.1 System description 22
3.2.2 Results and discussion 25
3.3 Experimental Validation Campaign 26
3.3.1 Methodology 26

3.3.2 Experimental multi-vendor validation in the Microsoft laboratory . . . 29
3.3.3 Experimental Validation of the Microsoft production network 37

4 Multi-band optimization and assessment 41
4.1 C+L Power Optimization . . . 41
4.1.1 Methodology and Results . . . 41
4.2 Multi-band point-to-point analysis . . . 46

5 Physical layer aware optical networking assessments 57
5.1 Offline Physical Layer Assessment . . . 58
5.1.1 Selection of Amplifier Upgrades Addressed by OPLA . . . 59
5.1.2 Technological solutions for OEO regenerator removal . . . 62
5.2 Statistical Network Assessment Process . . . 68
5.2.1 The structure of SNAP . . . 68
5.2.2 Networking Merit of SDM Technologies . . . 70
5.2.3 A Networking comparison of SDM and multi-band transmission 72

6 Network orchestration and automation 81
6.1 The PROnet SDN orchestrator architecture . . . 82
6.2 The network structure . . . 83
6.3 The QoT-E integration and validation . . . 85

7 Conclusions and Future Works 89
7.1 Summary . . . 89
7.2 Next Steps . . . 90

A The Raman scattering 93

B Fiber Parameters, Reference Topologies and Multi-Band parameters 97
B.1 Fiber Parameters . . . 97
B.2 Network Topologies . . . 97
B.3 Parameters used for Multi-Band transmission . . . 98

Bibliography 105

List of Tables

3.1 Fiber Parameters. 23
3.2 Parameters of the Raman amplifier's pumps. 24
3.3 Fiber parameters. 29
3.4 Fiber parameters. 37
4.1 Parameters of the Raman amplifier's pumps. 43
4.2 O-band Raman pump configuration. 48
4.3 Spectral efficiency of each scenario [bps/Hz]. 50
4.4 Maximum capacity [Tb/s]. 52
4.5 Gain factor with respect to full C-band and full C+L. 54
5.1 Benefits of DBP and PS. 65
5.2 BDM bandwidth occupation. 74
5.3 N_{M}, N_{BDM} and N_{SDM} of each investigated upgrades. 75
B.1 Fiber parameters. 98
B.2 Summary parameters of the network topologies. 100
B.3 Per band parameters. 103

List of Figures

2.1 Block diagram of an optical communication system. 6
2.2 General structure of a transmitter. 6
2.3 A sample of fix- and flex-grid coherent WDM comb. 7
2.4 Equivalent block diagram of a fiber span. 12
2.5 General structure of a receiver. 13
2.6 A possible arrangement of the 90° optical hybrid. 14
2.7 Physical layer abstraction of an optical network. 15
3.1 The structure of GNPy. 20
3.2 Simulated system. 23
3.3 Transmitted C+L spectrum (a) and received constellation after 10 spans (b). L-band channels are depicted in yellow, while C-band channels are depicted in green. 24
3.4 (a): Raman gain, including inter-channel SRS and Raman gain, at the end of the 80 km span. C-band is depicted in green, and L-band is depicted in yellow. (b): Power evolution across a span of three WDM channels. 25
3.5 Comparison of simulation results vs GGN-model estimation after 5 spans (blue) and after 10 spans (red). 26
3.6 Example of NF-vs-gain and P_{out} curves – the plot is for illustration purpose only and does not refer to any real amplifier –. 27
3.7 Qualitative example of the B2B BER-vs-OSNR characteristic of the transponder and the derivation of GSNR from a BER measurement - the curve is for illustration purpose only and do not refer to any real transceiver -. 27
3.8 The block diagram of the Microsoft test-bed. 29
3.9 An OSA measurement of the transmitted WDM comb. Channels from different vendors and the ASE noise are reported with different colors. 30
3.10 A photo of the network equipment. 30
3.11 Comparison of the measured and the estimated OSNR and GSNR for the PM-8QAM @2000 km 31

3.12 GSNR comparison of the estimation and the measurement in a power sweep for PM-8QAM. The legend shown in (c) applies to all three graphs. 32
3.13 Comparison of the estimation with the measurement for PM-8QAM. 33
3.14 Comparison of the estimation with the measurement for PM-QPSK. 34
3.15 Comparison of the estimation with the measurement for PM-16QAM. 34
3.16 Comparison of the estimation with the measurement for PM-8QAM with Raman amplifiers turned off. 34
3.17 Error distribution grouped by distance: 400 km (a), 800 km (b), 1200 km (c), 1600 km (d), 2000 km (e) and 4000 km (f). 35
3.18 Error distribution grouped by modulation format: PM-QPSK (a), PM-8QAM (b) and PM-16QAM (c). 35
3.19 Error histogram over all measured points in the lab network. 36
3.20 Layout of the analyzed network portion. Fiber types and lengths are described as well as amplifiers' type. Red and and blue dashed lines show the two analyzed paths. 38
3.21 Measured (triangles) and estimated (solid lines) for the set of channels over the two analyzed paths. ± 1 dB confidence intervals are shown as colored background. The red line and the green triangles belong to the path A-B and the orange triangles and the blue line belong to the path A-C. 39
3.22 Error histogram over all measured points in the production network. 40
4.1 Layout of the system under analysis. 42
4.2 Equivalent block scheme of the optical system. 42
4.3 Brute force tilt strategies of the transmitted power per channel (a) and the corresponding GSNR curves after one span (b). 44
4.4 The GSNR after 5 and 10 spans computed both by means of the SSFM and the GGN-model without pre-compensating the fiber tilt (a), pre-compensating 100% of the tilt (b), pre-emphasis 50% of the tilt (c) and with the optimum tilt pre-compensation (d). 45
4.5 Considered system configurations: (a) Full multi-band transmission; (b) O-band off; (c) O-band off, Raman in O-band, E → L-band. . . 46
4.6 Layout of the multi-band system under analysis. 47
4.7 Equivalent block diagram of a span. 48
4.8 Signal power at the beginning of the fiber ($z = 0$) in blue and at the end ($z = L_S$) in red, for L_S =50 km (a) and L_S =75 km (b). 49
4.9 Single span GSNR, $\mathrm{SNR_{ASE}}$ and $\mathrm{SNR_{NL}}$ in case all bands are used for channel transmission with $L_s = 75$ km. 51

4.10 Net bit-rate per wavelength for each scenario when considering two different span lengths. Each row reports different span lengths – $L_s = 50$ km the first and $L_s = 75$ km the second one. Each column refers to different bandwidth uses: full O→L the first, E→L without Raman amplification the second and E→L with Raman amplification the last one. 52
4.11 Maximum capacity per transmission band. Each row refers to a different reach: DCI (75 km) the first, metro (150 km) the second, extended metro (300 km) the third and regional (600 km) the last one. Left-hand side: 50 km spans; and right-hand side: 75 km spans. 53
5.1 The structure of OPLA. 58
5.2 Average GSNR for the brute force, the smart brute force and the minimum degradation approach. 61
5.3 The percentage of ULP enabled by OEO, hybrid OEO+DSP and DSP (a); the percentage of removed OEO regenerators (b); and the number of upgraded DSPs in the Pan-European network. 64
5.4 The percentage of ULP enabled by OEO, hybrid OEO+DSP and DSP (a); the percentage of removed OEO regenerators (b); and the number of upgraded DSPs in the USNET network. 65
5.5 The percentage of ULP enabled by OEO, hybrid OEO+HFA and HFA (a); the percentage of removed OEO regenerators (b); and the number of upgraded amplifiers in the Pan-European network. . . . 66
5.6 The percentage of ULP enabled by OEO, hybrid OEO+HFA and HFA (a); the percentage of removed OEO regenerators (b); and the number of upgraded amplifiers in the USNET network. 67
5.7 The flowchart of SNAP. 69
5.8 Blocking probability vs. allocated traffic normalized to the number of fibers/cores for a different number of cores and SDM solution. . . 71
5.9 Relative gain respect to the reference UFR with JoS at blocking probability equal to 0.01. 72
5.10 Network performances in the German topology by varying the multiplexing cardinality N_M: 2 (a), 3 (b), 4 (c), 6 (d) and 12 (e). 76
5.11 Network performances in the USNET topology by varying the multiplexing cardinality N_M: 2 (a), 3 (b), 4 (c), 6 (d) and 12 (e). 77
5.12 Total traffic per MUX cardinality @blocking probability 10^{-3} in German (a) and US-NET (b) topologies. 79
6.1 The software and hardware architecture. 82
6.2 Detailed scheme of the PROnet optical domain. 84
6.3 A photo of the commercial equipment hosted in the OpNeAR in the UTDallas campus (a) and in ViaWest (b). 84
6.4 The PSD with equal power per channel (a) and equal peak power spectral density (b). 86

6.5 The GSNR varying the transmitted power with equal power per channel (a) and equal power spectral density (b). 86
B.1 The German network topology. 98
B.2 The Pan-European network topology. 99
B.3 The USNET network topology. 99
B.4 The histogram of the link length for the German (a), the Pan-European (b) and the USNET (c) networks. 101
B.5 Fiber attenuation and dispersion of a SSMF from 1260 nm up to 1620 nm. 102
B.6 Raman efficiency of SSMF. 102

List of Abbreviations

API	application program interface
ASE	amplified spontaneous emission
B2B	back-to-back
BDM	band-division multiplexing
BER	bit-error-rate
BPD	balanced photodetector
BST	booster
Capex	capital expenditure
CCC	core-continuity constrain
CD	chromatic dispersion
CUT	channels-under-test
DBP	digital back-propagation
DCF	dispersion-compensating fiber
DCI	data center interconnect
DFA	doped-fiber amplifiers
DGE	dynamic gain equalizer
DSP	digital signal processor
DWDM	dense wavelength division multiplexing
EDFA	erbium-doped fiber amplifier
ELEAF	enhanced large effective area fiber
FEC	forward error correction
FH	Fault Handler
FL	Floodlight
FWM	four-wave mixing
GFF	gain-flattening filter

GGN	generalized Gaussian noise
GN	Gaussian noise
GSNR	generalized signal-to-noise ratio
HFA	hybrid Raman-EDFA fiber amplifier
ILA	in-line amplifier
ISI	inter-symbol interference
InS	independent switching
JoS	joint switching
JSON	JavaScript object notation
KSP	k-shortest path
LEAF	large effective area fiber
LLDP	link layer discovery protocol
LMS	least-mean-square
LOGO	local-optimum global-optimum
LP	lightpath
MB	multi-band
MC	media-channels
NDSF	non-dispersion-shifted fiber
NE	network element
NETCONF	network configuration protocol
NF	noise figure
NLI	non-linear interference
NLSE	nonlinear Schrödinger equation
NSR	noise-to-signal ratio
NZDSF	non-zero dispersion-shifted fiber
OA	optical amplifier
OADM	optical add-drop multiplexer
OEO	optical-electrical-optical
ODE	ordinary differential equations
ODL	OpenDaylight
ODTN	open disaggregated transport network
OFN	optical fiber network

OLSC open line system controller
ONOS open network operating system
Opex operational expenditure
OPLA offline physical layer assessment
OSA optical spectrum analyzer
OSNR optical signal-to-noise ratio
OTDR optical time domain reflectometer
OvS Open vSwitch
PBS polarized beam splitter
PDL polarization dependent loss
PM polarization multiplexed
PMD polarization mode dispersion
PRBS pseudo-random binary sequence
PROnet programmable optical network
PS probabilistic shaping
PSD power spectral density
PSE physical simulation environment
OpNeAR Open Networking Advanced Research
QAM quadrature amplitude modulation
QoS quality of service
QoT quality of transmission
QoT-E quality of transmission estimator
REST representational state transfer
ROADM re-configurable optical add-drop multiplexer
SDN software defined network
SNAP statistical network assessment process
SNR signal-to-noise ratio
RM resource management
RRC root-raised cosine
RWA routing and wavelength assignment
SC service catalog
SCF silica core fiber

SCMCF	strongly-coupled multi-core fiber
SDM	space division multiplexing
SOA	semiconductor optical amplifiers
SP	service provisioning
SRS	stimulated Raman scattering
SSFM	split-step Fourier method
SSMF	standard single mode fiber
TCO	total cost of ownership
TIP	Telecom Infra Project
TL1	transaction language 1
TWRS	TrueWave RS
TX	transmitter
UFR	uncoupled fiber ribbon
UI	user interface
ULP	under-performing lightpath
UTDallas	University of Texas at Dallas
VOA	variable optical attenuator
WDM	wavelength division multiplexing
WSS	wavelength selective switching

List of Scientific Contributions

The list of scientific contributions carried out during the PhD is here reported as well as a list of activities and collaborations.

Peer-Reviewed International Journals

[1] A. Ferrari, M. Filer, K. Balasubramanian, Y. Yin, E. Le Rouzic, J. Kundrát, G. Grammel, G. Galimberti, and V. Curri, "GNPy: an open source application for physical layer aware open optical networks". In: *Journal of Optical Communications and Networking* 12.6 (2020), pp. C31-C40.

[2] A. Ferrari, K. Balasubramanian, M. Filer, Y. Yin, E. Le Rouzic, J. Kundrát, G. Grammel, G. Galimberti, and V. Curri, "Assessment on the in-field lightpath QoT computation including connector loss uncertainties". In: *Journal of Optical Communications and Networking* 13.2 (2020), pp. A156-A164. [Invited from top scored OFC 2020 contribution]

[3] A. Ferrari, E. Virgillito, and V. Curri, "Band-Division vs. Space-Division Multiplexing: A Network Performance Statistical Assessment". In: *Journal of Lightwave Technology* 38.5 (2020), pp. 1041-1049.

[4] A. Ferrari, A. Napoli, J. K. Fischer, N. M. S. Da Costa, A. D'Amico, J. Pedro, W. Forysiak, E. Pincemin, A. Lord, A. Stavdas, J. P. F.-P. Gimnez, G. Roelkens, N. Calabretta, S. Abrate, B. Sommerkorn-Krombholz, and V. Curri, "Assessment on the Achievable Throughput of Multi-band ITU-T G. 652. D Fiber Transmission Systems". In: *Journal of Lightwave Technology* 38.16 (2020), pp. 4279-4291.

[5] N. Sambo, A. Ferrari, A. Napoli, N. Costa, J. Pedro, B. Sommerkorn-Krombholz, P. Castoldi, and V. Curri, "Provisioning in Multi-Band Optical Networks". In: *Journal of Lightwave Technology* 38.9 (2020), pp. 2598-2605. [Invited from higly scored ECOC 2019 contribution]

[6] M. Cantono, A. Ferrari, D. Pilori, E. Virgillito, J.L. Augé, and V. Curri, "Physical layer performance of multi-band optical line systems using Raman

amplification". In: *Journal of Optical Communications and Networking* 11.1 (2019), pp. A103-A110. [Invited from top-scoring OFC 2018 contribution]

[7] D. Pilori, M. Cantono, A. Ferrari, A. Carena, and V. Curri, "Observing the effect of polarization mode dispersion on nonlinear interference generation in wide-band optical links". In: *OSA Continuum* 2.10 (2019), pp. 2856-2863.

[8] T. Zhang, A. Samadian, A. Shakeri, B. Mirkhanzadeh, C. Shao, M. Razo, M. Tacca, A. Ferrari, M. Cantono, and V. Curri, "A WDM network controller with real-time updates of the physical layer abstraction". In: *Journal of Lightwave Technology* 37.16 (2019), pp. 4073-4080.

[9] A. Ferrari, M. Cantono, A. Ahmad, and V. Curri, "Physical layer strategies to save lightpath regenerators". In: *Journal of Optical Communications and Networking* 10.9 (2018), pp. 703-711.

[10] M. Cantono, D. Pilori, A. Ferrari, C. Catanese, J. Thouras, J.L. Augé, and V. Curri, "On the interplay of nonlinear interference generation with stimulated Raman scattering for QoT estimation". In: *Journal of Lightwave Technology* 36.15 (2018), pp. 3131-3141.

[11] M. Filer, M. Cantono, A. Ferrari, G. Grammel, G. Galimberti, and V. Curri, "Multi-vendor experimental validation of an open source QoT estimator for optical networks". In: *Journal of Lightwave Technology* 36.15 (2018), pp. 3073-3082.

International Conferences

[1] A. Ferrari, M. Filer, K. Balasubramanian, Y. Yin, E. Le Rouzic, J. Kundrát, G. Grammel, G. Galimberti, and V. Curri, "Experimental validation of an open source quality of transmission estimator for open optical networks". In: *Optical Fiber Communication Conference (OFC)*. 2020. [Top-scored OFC paper]

[2] A. Ferrari, K. Balasubramanian, M. Filer, Y. Yin, E. Le Rouzic, J. Kundrát, G. Grammel, G. Galimberti, and V. Curri, "Softwarized Optical Transport QoT in Production OpticalNetwork: a Brownfield Validation". In: *European Conference on Optical Communication (ECOC)*. 2020.

[3] A. Ferrari, J. Kundrát, E. Le Rouzic, M. Filer, A. Campanella, A. D'Amico, K. Balasubramanian, Y. Yin, O. Havliš, M. Hažlinský, J. Vojtěch, J.L. Augé, G. Grammel, G. Galimberti, and V. Curri "The GNPy Open Source Library of

Applications for Software Abstraction of WDM Data Transport in Open Optical Networks". In: *IEEE Conference on Network Softwarization (NetSoft)*. 2020.

[4] A. Ferrari, E. Virgillito, and V. Curri, "Networking merit of spatial-division and band-division multiplexing: A statistical assessment". In: *International Conference on Transparent Optical Networks (ICTON)*. 2020. [Invited]

[5] A. Ferrari, M. Filer, E. Le Rouzic, J. Kundrát, B. Correia, K. Balasubramanian, Y. Yin, G. Grammel, G. Galimberti, and V. Curri, "GNPy: an open source planning tool for open optical networks". In: *International Conference on Optical Network Design and Modeling (ONDM)*. 2020.

[6] E. Virgillito, R. Sadeghi, A. Ferrari, G. Borraccini, and V. Curri, "Network Performance Assessment of C+ L Upgrades vs. Fiber Doubling SDM Solutions". In: *Optical Fiber Communication Conference (OFC)*. 2020.

[7] J. Kundrát, A. Campanella, E. Le Rouzic, A. Ferrari, O. Havliš, M. Hažlinský, G. Grammel, G. Galimberti, and V. Curri, "Physical-layer awareness: GNPy and ONOS for end-to-end circuits in disaggregated networks". In: *Optical Fiber Communication Conference (OFC)*. 2020.

[8] S. Barzegar, E. Virgillito, M. Ruiz, A. Ferrari, A. Napoli, V. Curri, and L. Velasco, "Soft-Failure Localization and Device Working Parameters Estimation in Disaggregated Scenarios". In: *Optical Fiber Communication Conference (OFC)*. 2020.

[9] G. Borraccini, A. Ferrari, S. Straullu, A. Nespola, A. D'Amico, S. Piciaccia, G. Galimberti, A. Tanzi, S. Turolla, and V. Curri, "Softwarized and Autonomous Raman Amplifiers in Multi-Band Open Optical Networks". In: *International Conference on Optical Network Design and Modeling (ONDM)*. 2020.

[10] E. Virgillito, R. Sadeghi, A. Ferrari, A. Napoli, B. Correia, and V. Curri, "Network performance assessment with uniform and non-uniform nodes distribution in C+ L upgrades vs. fiber doubling SDM solutions". In: *International Conference on Optical Network Design and Modeling (ONDM)*. 2020.

[11] G. Borraccini, S. Straullu, A. Ferrari, S. Piciaccia, G. Galimberti, and V. Curri, "Flexible and Autonomous Multi-band Raman Amplifiers". In: *IEEE Photonics Conference (IPC)*. 2020.

[12] A. Ferrari, D. Pilori, E. Virgillito, and V. Curri, "Power control strategies in C+ L optical line systems". In: *Optical Fiber Communication Conference (OFC)*. 2019.

[13] A. Ferrari, A. Napoli, N. Costa, J. K. Fischer, J. Pedro, W. Forysiak, A. Richter, E. Pincemin, and V. Curri, "Multi-band optical systems to enable ultra-high speed transmissions". In: *The European Conference on Lasers and Electro-Optics (CLEO)*. 2019.

[14] A. Ferrari, A. Napoli, J. K. Fischer, N. Costa, J. Pedro, N. Sambo, E. Pincemin, B. Sommerkohrn-Krombholz, and V. Curri, "Upgrade capacity scenarios enabled by multi-band optical systems". In: *International Conference on Transparent Optical Networks (ICTON)*. 2019. [Invited]

[15] A. Ferrari, G. Borraccini, and V. Curri, "Observing the generalized SNR statistics induced by gain/loss uncertainties". In: *European Conference on Optical Communication (ECOC)*. 2019.

[16] D. Zibar, A. Ferrari, V. Curri, A. Carena, "Machine learning-based Raman amplifier design". In: *Optical Fiber Communication Conference (OFC)*. 2019.

[17] J. K. Fischer, P. W. Berenguer, B. Shariati, A. Napoli, E. Pincemin, A. Ferrari, V. Curri, N. Costa, and J. Pedro, "Optical multi-band networks: maximizing lifetime of deployed fiber infrastructure". In: *Photonic Networks and Devices*. 2019.

[18] E. Virgillito, A. D'Amico, A. Ferrari, and V. Curri, "Observing and Modeling Wideband Generation of Non-Linear Interference". In: *International Conference on Transparent Optical Networks (ICTON)*. 2019.

[19] N. Sambo, A. Ferrari, A. Napoli, N. Costa, J. Pedro, B. Sommerkohrn-Krombholz, P. Castoldi, and V. Curri, "Provisioning in multi-band optical networks: A C+ L+ S-band use case". In: *European Conference on Optical Communication (ECOC)*. 2019. [Highly scored paper]

[20] A. Ferrari, M. Cantono, and V. Curri, "A networking comparison between multicore fiber and fiber ribbon in WDM-SDM optical networks". In: *European Conference on Optical Communication (ECOC)*. 2018.

[21] A. Ferrari, M. Cantono, B. Mirkhanzadeh, Z. Lu, A. Shakeri, C. Shao, M. Tacca, M. Razo, A. Fumagalli, and G. Martinelli, G. M. Galimberti, and V. Curri "A two-layer network solution for reliable and efficient host-to-host transfer of big data". In: *International Conference on Transparent Optical Networks (ICTON)*. 2018.

[22] A. Ferrari, M. Cantono, and V. Curri, "Coupled vs. Uncoupled SDM Solutions: A Physical Layer Aware Networking Comparison". In: *International Conference on Transparent Optical Networks (ICTON)*. 2018.

[23] M. Cantono, D. Pilori, A. Ferrari, A. Carena, and V. Curri, "Observing the interaction of PMD with generation of NLI in uncompensated amplified optical links". In: *Optical Fiber Communication Conference (OFC)*. 2018.

[24] B. Mirkhanzadeh, A. Ferrari, Z. Lu, A. Shakeri, C. Shao, M. Tacca, M. Razo, M. Cantono, and V. Curri, and G. Martinelli, "Two-layer network solution for reliable and efficient host-to-host transfer of big data". In: *Photonic Networks and Devices*. 2018.

[25] E. Ghillino, E. Virgillito, P. V. Mena, R. Scarmozzino, R. Stoffer, D. Richards, A. Ghiasi, A. Ferrari, M. Cantono, A. Carena, and V. Curri, "The Synopsys Software Environment to Design and Simulate Photonic Integrated Circuits: A Case Study for 400G Transmission". In: *International Conference on Transparent Optical Networks (ICTON)*. 2018.

[26] H. Ali, A. Ahmad, A. Ferrari, and V. Curri, "Impact of Fiber Type on Regenerator Placement in Reconfigurable DWDM Transparent Optical Networks". In: *Photonics in Switching and Computing (PSC)*. 2018.

[27] A. Ferrari, M. Cantono, U. Waheed, A. Ahmad, and V. Curri, "Networking benefits of advanced DSP techniques and hybrid fiber amplification". In: *International Conference on Transparent Optical Networks (ICTON)*. 2017.

[28] A. Ferrari, M. Cantono, and V. Curri, "Networking benefits of advanced DSP techniques". In: *Fotonica*. 2017.

[29] M. Cantono, A. Ferrari, U. Waheed, A. Ahmad, S.M. H. Zaidi, A. Bianco, and V. Curri, "Networking benefit of hybrid fiber amplification for lightpath regenerators saving". In: *Optical Fiber Communication Conference (OFC)*. 2017.

Activities and Collaborations

- Collaboration with Cisco Photonics on innovative design strategies for transparent optical networks - *2017 - ongoing*
- Collaboration with the Physical Simulation Environment group of the Telecom Infra Project on the development of GNPy: a vendor-agnostic QoT estimator - *2017 - ongoing*
- Collaboration with Microsoft for the validation campaigns of GNPy - *2018 - ongoing*

- Collaboration with OpNear Lab at the University of Texas at Dallas on the development of a Quality of transmission estimation module to be integrated into the ProNet multilayer orchestrator - *2017*
- Collaboration with Lumentum on the control and automation of open and disaggregated line systems - *2020* - *ongoing*

Chapter 1

Introduction

The history of optical communication [4, 6] started in 1792 with Claude Chappe, who invented the optical telegraph. However, the absence of a coherent optical source and an appropriate optical medium made the development of modern optical communication systems as we know them today impossible. Then, in 1960 the laser was invented, and, also in that period, optical fibers started to spread around. However, optical fibers were not seriously taken into account for telecommunication applications because of their high loss, which made the communication along more that few meters impossible. This view prevailed until the 1966, when it was observed that the loss of the fibers could be drastically reduced by removing the impurities of the silica glass making the optical fiber the best medium for communication systems [93]. Consequently, the scientific community took up the challenge and started investigating this possibility. In 1970, among others the American company Corning demonstrated the capability of reducing the attenuation of the fibers below 20 dB/km around 630 nm [94]. Subsequently, Corning demonstrated a further reduction of the attenuation down to 4 dB/km by using germanium to dope the core of the fibers. Eventually, in 1979, the NTT Ibaraki Electrical Communication Laboratory attained an attenuation loss of 0.2 dB/km at 1550 nm [113], which is very close to the theoretical limit.

In tandem with these developments, also the research on laser technologies evolved to obtain sources able to operate at the optical frequencies at room temperature. Such a milestone was achieved with GaAs semiconductor lasers contemporary, proposed by the Ioffe Physica-Technical Institute, Russia [5], and by the Bell Laboratories [82].

Owing to the availability of compact optical sources and a low attenuation media, in the 70s, the first generation of optical communication systems has been developed to operate at the rate of 45 Mbps at 850 nm for a maximum reach of 10 km. Therefore, in 1980, the first generation of optical communication systems started to be commercialized and deployed.

Since then, several technological generations have passed. The first generation

was characterized by the adoption of GaAs based coherent sources, and therefore the signals were transmitted at the wavelength of 850 nm by exploiting the so called *first window*. In order to overcome the limits of the first generation, a lot of effort has been invested to move the wavelength of the optical source around 1300 nm, the so called *second window* or O-band, since therein the fiber attenuation was significantly smaller. In what followed, the third generation targeted operating around 1550 nm in the so called *third window* or C-band, by adopting InGaAsP semiconductor lasers. The reason being is that at that wavelength the attenuation of the fiber is at its lowest. However, the large dispersion of the C-band compared to the O-band made the adoption of such a window difficult. In order to overcome this issue, dispersion shifted fibers were developed to reduce the fiber dispersion in the C-band. Afterwards, the fourth generation focused on the replacement of repeaters with optical amplifiers, the periodic compensation of the fiber dispersion by using special fibers called dispersion-compensating fiber (DCF), and the adoption of the wavelength division multiplexing (WDM) technology consisting of multiplexing together the signals, generated by different optical sources operating at different wavelengths in order to propagate them through the same fiber. Then, the fifth generation focused on improving the efficiency of the transceivers by replacing the on-off key schemes based on modulating only by turning the light on and off, with the more complex quadrature amplitude modulation (QAM) modulation schemes able to modulate not only the amplitude of the signal, but also the phase and the polarization. This new structure allows higher spectral efficiency as well as the removal of DCFs since the dispersion can now be digitally compensated at the receiver by means of the digital signal processor (DSP). This led to a significant revolution in the structure of the optical networks, by enabling the paradigm of transparent optical networks, where the optical signals are not received and re-transmitted at each node, but they can pass through them transparently through optical add-drop multiplexer (OADM) devices. This new paradigm has revolutionized the way of approaching the optical layer, as now it requires a holistic approach considering the whole notwork as a single system and no more as just a set of independent point-to-point connections. Therefore, this resulted in an increase in the design and management complexity of the optical layer, and this required the automation of the optical layer to simplify the operations on the network and to reduce the human error. Moreover, to simplify the network management and to scale down the costs of upgrading the infrastructure, the operators are pushing the market toward the paradigm of *open* and *disaggregated* optical networks, where each network element can be interfaced through open and standard APIs according to common data models and it can be replaced without the need for other changes in the rest of the infrastructure. This leads to a multi-vendor and multi-generation environment. In this view, initiatives such as OpenConfig [121], OpenROADM [12] and the Telecom Infra Project [1] were created.

Moreover, in order to further enhance the network capacity, C+L systems have

been recently proposed [174] and made available on the market. Such systems aim at increasing the number of channels per fiber pair by extending the occupied bandwidth to the L-band (1565 nm to 1625 nm). Other technologies exploring the possibility to increase the capacity include the use of multi-band systems targeting the further extension of the used band to include all the low-loss optical bands, the use of advanced DSP techniques such as digital back-propagation (DBP) and probabilistic shaping (PS) and the use of space division multiplexing (SDM) techniques employing ribbons of parallel single mode fibers, multi-core fibers and few-mode fibers.

Chapter 2

An introduction to the network optical layer

This chapter introduces the fundamental concepts of the optical network describing the physical impairments of an optical communication system and the process of allocating the network resources to accommodate the required traffic according to a routing and wavelength assignment (RWA).

2.1 Modelling the physical layer of an optical network

A modern communication system, as depicted in Fig. 2.1, involves a set of transmitters encoding the digital data in N_{ch} channels, frequency multiplexed together by a WDM multiplexer. The signals are properly switched toward the proper node degree by a re-configurable optical add-drop multiplexer (ROADM) node. Then, the signals are propagated through an optical cable through a cascade of optical amplifiers and N_s fiber spans. The first amplifier is called the booster (BST) and it sets the transmitted power P_{TX}. The BST amplifier is followed by a cascade of fibers and amplifiers (called in-line amplifier (ILA)s). Finally, a pre-amplifier concludes the transmission line and the ROADM node takes care of routing each signal to the proper node degree, or to the node de-multiplexer toward the receiver. Finally, the receivers demodulate the signals and retrieve the original digital data.

2.1.1 The transmitter

State-of-the-art optical transmitters [98] are coherent multi-level modulation format transceivers, which encode the information in the in-phase and quadrature components of the electric signal and make use of both the polarization states. This

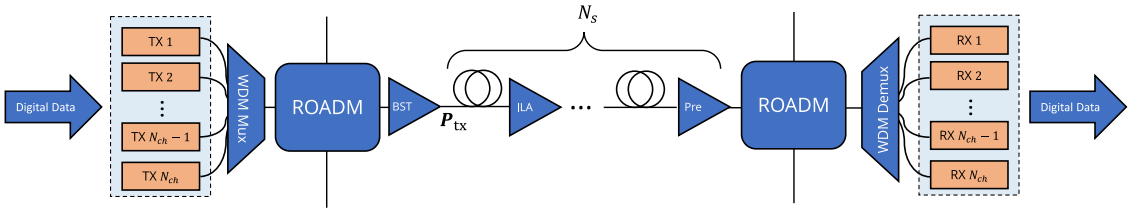

Figure 2.1: Block diagram of an optical communication system.

is done by making use of a polarization multiplexed (PM)-QAM format having root-raised cosine (RRC) shape.

The structure of a modulator is depicted in Fig. 2.2. Firstly, the data is encoded by using two separate encoders. These encoders map the bits into an electrical signal, that is then used to drive an optical modulator. Subsequently, a laser source generates a 45° linearly polarized beam $\mathbf{E}_{\mathrm{L}}(t)$, which is separated by a polarized beam splitter (PBS) into a vertically polarized beam and a horizontally polarized one. Then, each of the two beams is modulated according to an M-QAM modulation scheme. In this way, a vertically polarized and a horizontally polarized modulated electric field - $E_x(t)\hat{\mathbf{x}}$ and $E_x(t)\hat{\mathbf{y}}$ are obtained, respectively. Finally, the transmitted electric field $\mathbf{E}_{\mathrm{TX}}(t)$ is obtained by combining $E_x(t)\hat{\mathbf{x}}$ and $E_x(t)\hat{\mathbf{y}}$, using a PBS, as:

$$\mathbf{E}_{\mathrm{TX}}(t) = E_x(t)\hat{\mathbf{x}} + E_y(t)\hat{\mathbf{y}} = \left[E_{p,x}(t) + E_{q,x}(t)\right]\hat{\mathbf{x}} + \left[E_{p,y}(t) + E_{q,y}(t)\right]\hat{\mathbf{y}} \qquad (2.1)$$

where $E_{p,x}(t)$ and $E_{q,x}(t)$ are respectively the in-phase and quadrature components of the x polarization state and $E_{p,y}(t)$ and $E_{q,y}(t)$ are for the y polarization state.

In this way, the resulting optical signal has RRC power spectral density, centered around the laser frequency f_{c}.

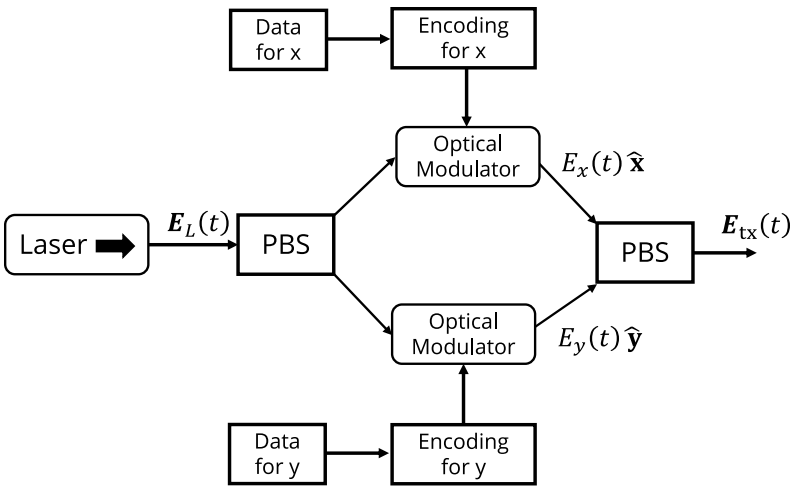

Figure 2.2: General structure of a transmitter.

In a modern optical network, signals are multiplexed together by using a WDM

technique, as shown in Fig. 2.3, where the optical spectrum is divided in *spectral slots* and each slot is dedicated to a specific channel. This can be obtained by tuning the laser of each transmitter around different central frequencies (f_c). The grid can be fixed or flexible [143]. Each grid can be characterized by a total bandwidth (B_{opt}), a resolution grid Δf that defines the dimension of a frequency slot and the central frequency of the comb f_0. If the grid is fixed, each channel uses only one slot and Δf also indicates the frequency offset between the two adjacent channels. For a fix-grid, Δf is typically 50, 75 or 100 GHz. On the contrary, in the case of a flex-grid, the channels may occupy more than one frequency slot and Δf is 12.5 GHz.

The result is a WDM comb, which is the sum of N_{ch} channels:

$$G_{\text{WDM}}(f) = \sum_{i=1}^{N_{\text{ch}}} G_{\text{ch},i}(f - f_{\text{c},i}) \ , \tag{2.2}$$

where $G_{\text{WDM}}(f)$ is the power spectral density (PSD) [10] of the WDM comb, $G_{\text{ch},i}(f)$ is the PSD of the base-band [10] signal generated by the i-th transmitter and $f_{\text{c},i}$ is the laser frequency of the i-th transmitter and, consequently, the central frequency of the transmitted signal.

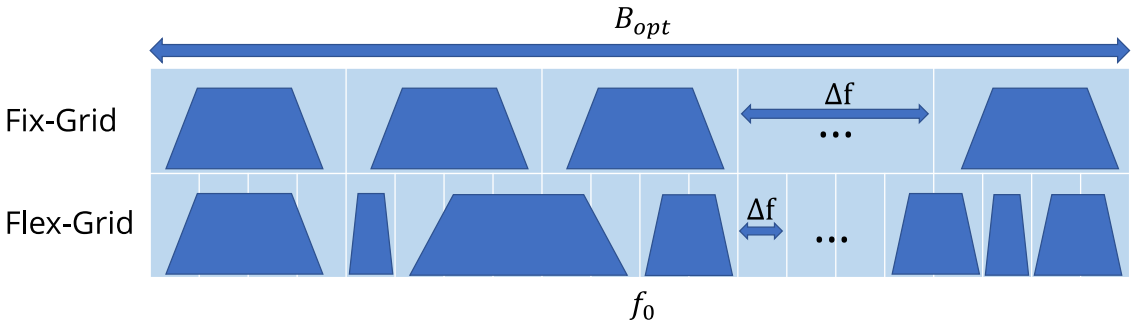

Figure 2.3: A sample of fix- and flex-grid coherent WDM comb.

2.1.2 Modelling the amplifier propagation

An optical amplifier is a device aiming at restoring the signal power after some attenuation due to the fiber propagation or to other passive optical modules such as, for example, the ROADM nodes. Optical amplifiers can be lumped amplifiers, such as semiconductor optical amplifiers (SOA) [35] or doped-fiber amplifiers (DFA) [44] or distributed amplifiers, such as the Raman amplifiers [18].

SOAs use the semiconductor as the active medium to amplify the signal. However, they are little used because of their strong non-linear response.

The most common amplification technique used is erbium-doped fiber amplifier (EDFA), which consists in a spool of fiber doped with Erbium, in order to make the

fiber an active medium [44]. Some 980 nm pumps are used to reach the population inversion condition, which makes the stimulated emission of photons possible, and thus the amplification. However, together with the stimulated emission responsible for the gain, the population inversion produces also the spontaneous emission, which has the net effect of generating the amplified spontaneous emission (ASE) noise disturbance.

Raman amplifiers are an effective amplification technique based on the injection of the so called Raman pumps[1] into the fiber which make the fiber an active medium, however, an extensive use of the Raman amplifiers would enhance dramatically the Kerr effect in the fiber and, subsequently, it would highly enhance the signal disturbance. For this reason, Raman amplifiers are operated in the so called moderate pumping regime [38], and they are jointly used with EDFAs to obtain the so called hybrid Raman-EDFA fiber amplifier (HFA)s. HFAs are optical amplifiers using in cascade a Raman amplifier with counter-propagating Raman pumps followed by an EDFA. The main advantage of using HFAs instead of the only EDFA is a strong reduction in the overall noise impact of the amplification site. Thus, each amplifier can be described by the system parameters, such as the gain $G(f)$ and the noise figure $F(f)$. Therefore, given the i-th signal with power $P_{\mathrm{in},i}$ at the input of the amplifier, the output power will be

$$P_{\mathrm{out},i} = P_{\mathrm{in},i}\, G(f_{\mathrm{c},i}) \tag{2.3}$$

where $f_{\mathrm{c},i}$ is the central frequency of the i-th channel. Moreover, as the only disturbance introduced by the amplifier is the ASE noise, the generalized signal-to-noise ratio (GSNR) degradation introduced by an optical amplifier will be:

$$\mathrm{GSNR}_{\mathrm{OA}} = \mathrm{SNR}_{\mathrm{ASE,OA}} = \frac{P_{\mathrm{out},i}}{P_{\mathrm{ASE}}(f_{\mathrm{c},i})} = \frac{P_{\mathrm{in},i}\, G(f_{\mathrm{c},i})}{P_{\mathrm{ASE}}(f_{\mathrm{c},i})} \tag{2.4}$$

where the ASE noise power P_{ASE} is computed as:

$$P_{\mathrm{ASE}}(f) = hf(G(f) - 1)F(f)B_{\mathrm{ref}} \tag{2.5}$$

where h is the Planck constant and B_{ref} is the reference noise bandwidth which, in this thesis, will be always equal to the channel symbol rate R_{s} , unless otherwise specified.

2.1.3 Modelling the fiber propagation

The fiber is a passive medium made of glass, which guides the light along the way. The propagation of a WDM comb through a fiber span is characterized

[1] A complete description on how to model the Raman amplification is described in the appendix A

by the linear impairments, such as the attenuation, the chromatic dispersion (CD), the polarization mode dispersion (PMD) and the polarization dependent loss (PDL) and by the non-linear impairments, such as the Raman scattering and the non-linear interference (NLI), generated by the Kerr effect [95, 96].

The attenuation is the simplest of the propagation effects and it causes a linear reduction of the power of the light propagating through the fiber. Such an effect is caused by three main factors: the infrared and ultraviolet absorption, the Rayleigh scattering and the absorption due to the presence of ions [3, 175]. The fiber attenuation is fully described by an attenuation coefficient (α). Moreover, in general, the attenuation is frequency dependent and thus, when a wide range of frequencies is involved, it is mandatory to consider it as a function of the frequency: $\alpha(f)$.

In detail, the power attenuation $A(f)$ of a fiber span having length L_s is:

$$A(f) = e^{-2\alpha(f)L_\mathrm{s}} \ , \tag{2.6}$$

where $\alpha(f)$ is the attenuation coefficient. Accordingly, the power of the i-th channel at the output of a fiber span is:

$$P_{\mathrm{out},i} = P_{\mathrm{in},i} \times A(f_{\mathrm{c},i}) \tag{2.7}$$

where $P_{\mathrm{in},i}$ is the power of the i-th channel at the input of the fiber and $A(f_{\mathrm{c},i})$ is the fiber attenuation evaluated at the central frequency of the i-th channel.

The CD is a propagation phenomenon caused by the dependence of the velocity of the light on the wavelength [3]. This impairment causes a linear distortion in the signal and it can be modeled with an equivalent filter [47] having a transfer function $H_{CD}(f)$:

$$H_{CD}(f) = e^{-j\beta(f)L_\mathrm{s}} \tag{2.8}$$

where $\beta(f)$ is the dispersion parameter of the fiber and L_s is the fiber length. Generally, the Taylor series of $\beta(f)$ at f_0 is used:

$$\beta(f) = \beta_0 + 2\pi\beta_1(f - f_0) + 2\pi^2\beta_2(f - f_0)^2 + \frac{4}{3}\pi^3\beta_3(f - f_0)^3 \ . \tag{2.9}$$

Furthermore, as the terms β_0 and β_1 are related to the phase delay and to the group delay, respectively, they do not affect the quality of transmission (QoT). Therefore, they can be safely neglected and the equation 2.1.3 becomes:

$$H_{CD}(f) = e^{-j\left(2\pi^2\beta_2(f-f_0)^2+\frac{4}{3}\pi^3\beta_3(f-f_0)^3\right)L_\mathrm{s}} \tag{2.10}$$

Both the PMD [42] and the PDL [108] are due some non-perfect cylindrical symmetry of the fiber, while the PMD is a random difference in the group velocity [3, 78, 99, 104] between the polarization states, the PDL is a random difference in the attenuation experienced by the two polarizations. However, in most of the cases,

the performance of modern multi-level modulation based signals is not impaired by the CD, the PMD and the PDL, since the DSP of the receiver compensates them [86, 181].

Raman scattering [18, 142] involves the stimulated Raman scattering (SRS) and spontaneous Raman scattering. The SRS is an inelastic scattering of an optical signal travelling in the silica, which causes an energy transfer from the higher frequency channels to the lower frequency channels together with the emission of phonons. The net effect on a WDM comb propagating through a fiber is a tilt in the spectrum. Moreover, such a phenomenon is exploited by Raman amplifiers which inject some high frequency pumps - the so-called Raman pumps - into the fiber to amplify the WDM signals while travelling along the fiber. In this case, the spontaneous Raman scattering is triggered by the light travelling in the silica, which generates a spontaneous emission at the lower frequencies. The net effect is a generation of ASE noise, which is generated by every channel and every pump. However, the power of the channels is typically small enough that only the ASE noise generated by the Raman pumps is assessed while evaluating the propagation performances of the channels. Raman scattering in silica is characterized by the Raman gain spectrum. The mathematical description of Raman scattering is described in detail in appendix A and the Raman gain spectrum of the standard single mode fiber (SSMF) is depicted in Fig. 3.4a in appendix B.

Lastly, the non-linear Kerr effect [95, 96] is a variation in the refractive index depending on the optical power travelling into the fiber, which causes NLI. Such effect is included in the nonlinear Schrödinger equation (NLSE) [3, 126], which describes the propagation of an optical signal travelling through the fiber. Later, the Manakov [3, 104] equation was derived by averaging the PMD in order to decouple the equations of the two polarization states. In state-of-the-art modern optical networks coherent multi-level modulated signals travel along an uncompensated optical link and, in this case, the net effect of the NLI on the signal can be described as an introduction of phase noise plus additive Gaussian noise. It has been shown that the phase noise component has long correlation [41] and thus, the DSP can exploit it to remove the phase noise [131, 134]. For this reason, over the years, many studies have been proposed to model the PSD of this equivalent additive Gaussian noise (GN) [13, 14, 31, 88, 89, 135, 153, 177]. The GN-model is based on three main assumptions: the signals are considered as Gaussian distributed, the NLI acts as an additive Gaussian noise and the non-linearity is a "perturbation" of the propagating electric field. Given these assumptions, starting from the Manakov equation, the GN-model [133] provides an equivalent PSD of the NLI ($G_{NLI}(f)$).

For a single fiber span, the GN-model [133, 137] provides the following formula:

$$G_{\mathrm{NLI}}(f) = \frac{16}{27}\gamma^2 \int_{-\infty}^{\infty}\int_{-\infty}^{\infty} G_{\mathrm{WDM}}(f_1)\, G_{\mathrm{WDM}}(f_2)\, G_{\mathrm{WDM}}(f_1+f_2-f)\cdot \left|\frac{1-e^{2\alpha L_{\mathrm{s}}} e^{4\pi^2\beta_2 L_{\mathrm{s}}(f_1-f)(f_2-f)}}{2\alpha - j4\pi^2\beta_2(f_1-f)(f_2-f)}\right|^2 df_1 df_2 \tag{2.11}$$

where γ is the non-linear coefficient of the fiber, $G_{\mathrm{WDM}}(f)$ is the PSD of the WDM comb at the input of the fiber, L_{s} is the fiber span length and β_2 is the dispersion coefficient of the fiber.

This model can be generalized from a single span system to a multi-span system by introducing the phased array factor as shown in eq. (1) in [133]. However, the NLI accumulation can also be considered incoherent as shown in eq. (18) in [133] by considering the NLI generation of each fiber as independent on the other fibers as, increasing the number of channels, the gap between the coherent and the incoherent model reduces.

As experimentally demonstrated [116, 117], the GN-model provides reliable and accurate predictions of the NLI. However, when the occupied bandwidth increases, the SRS becomes dominant and, for this reason, the GN-model has been recently generalized to include the SRS [21, 24, 26, 147, 156]. The generalized Gaussian noise (GGN)-model starts again from the Manakov equations and follows the same steps of the GN-model by including a frequency dependent attenuation and the SRS. The resulting NLI PSD is

$$G_{\mathrm{NLI}}(f) = \frac{16}{27}\gamma^2\rho(z,f)^2 \int_{-\infty}^{\infty}\int_{-\infty}^{\infty} G_{\mathrm{WDM}}(f_1)\, G_{\mathrm{WDM}}(f_2)\, G_{\mathrm{WDM}}(f_1+f_2-f)\cdot \left|\int_0^{L_{\mathrm{s}}} \frac{\rho(\zeta,f_1)\rho(\zeta,f_2)\rho(\zeta,f_1+f_2-f)}{\rho(\zeta,f)}\, e^{j4\pi^2(f_1-f)(f_2-f)[\beta_2+\pi\beta_3(f_1+f_2)\zeta]} d\zeta\right|^2 \mathrm{d}f_1 \mathrm{d}f_2 \tag{2.12}$$

where $\rho(z,f)$ is the gain/loss profile which can be evaluated as shown in appendix A and β_3 is the dispersion slope of the fiber. Then, the equivalent power of the NLI disturbance on the i-th channel can be evaluated as:

$$P_{\mathrm{NLI},i} = \int_{f_{\mathrm{c},i}-\frac{R_{\mathrm{s}}}{2}}^{f_{\mathrm{c},i}+\frac{R_{\mathrm{s}}}{2}} G_{\mathrm{NLI}}(f)\,\mathrm{d}f \tag{2.13}$$

where R_{s} is the symbol rate of the i-th channel. It has to be noted that the model does not depend on the modulation format of the signals. This is due to the conservative assumption of considering the channels as Gaussian distributed. This is also useful for designing an optical system independently of the modulation format of the signals, and for making a modulation format decision strategy independent of the modulation format itself, thereby making the algorithm much easier.

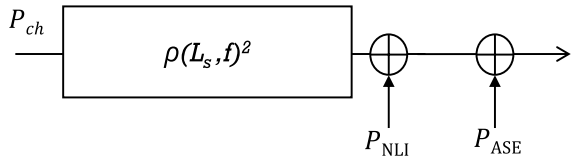

Figure 2.4: Equivalent block diagram of a fiber span.

The equivalent model of a fiber span, including the SRS, the NLI and the ASE noise generated by the spontaneous Raman scattering is depicted in Fig. 2.4. Thus, the overall GSNR contribution of a fiber span is:

$$\mathrm{GSNR}_{\mathrm{F}} \triangleq \frac{P_{\mathrm{out},i}}{P_{\mathrm{NLI},i} + P_{\mathrm{ASE}}(L_{\mathrm{s}}, f_{\mathrm{c},i})} = \frac{P_{\mathrm{in},i}\,\rho(L_{\mathrm{s}}, f_{\mathrm{c},i})^2}{P_{\mathrm{NLI},i} + P_{\mathrm{ASE}}(L_{\mathrm{s}}, f_{\mathrm{c},i})}\,. \tag{2.14}$$

In absence of Raman pumps, the ASE noise produced by the Raman amplification can be neglected.

2.1.4 Modelling the ROADM

The OADM is a crucial network element (NE) since it enables the transparent switching of an optical channel through the intermediate nodes without receiving and re-transmitting the signal at every node. The consequent reduction in the number of transceivers deployed in a network bring to the operators a significant reduction in the power consumption and in the expenditures of the infrastructure, which leads to a reduction in the network capital expenditure (Capex) and operational expenditure (Opex). Moreover, the dynamic re-configuration introduced by the ROADMs eases the network planning and management, enabling a dynamic approach to the allocation of the network resources [152, 161].

However, the ROADMs introduce some propagation effects that have to be properly considered, such as the PMD, the PDL and the filtering effects and the cross-channel cross-talk. Exactly as the fiber propagation, the ROADMs introduce a PMD and a PDL which introduces a random variation in the group velocity and in the loss of the two polarizations which, in modern optical systems, are compensated by the DSP. Moreover, the add-drops have to filter the WDM combs to separate every channel or media-channel to re-route them toward different directions. However, the optical filters are not ideal and therefore, they introduce a linear distortion, which leads to the generation of inter-symbol interference (ISI). This disturbance can not be easily modeled since, in general, it depends on the spectral shape of the signal, the filter transfer function and on the specific DSP implementation [75, 154, 168]. These aspects make the accurate modelling of the filtering penalty complicated. For this reason, the penalty is usually evaluated by means of lab experiments or simulations [84, 123, 141, 171]. Otherwise, the filtering penalty is considered by imposing a limit in the maximum number of ROADM

nodes that a path can traverse [165] before experiencing significant penalties.

2.1.5 The receiver

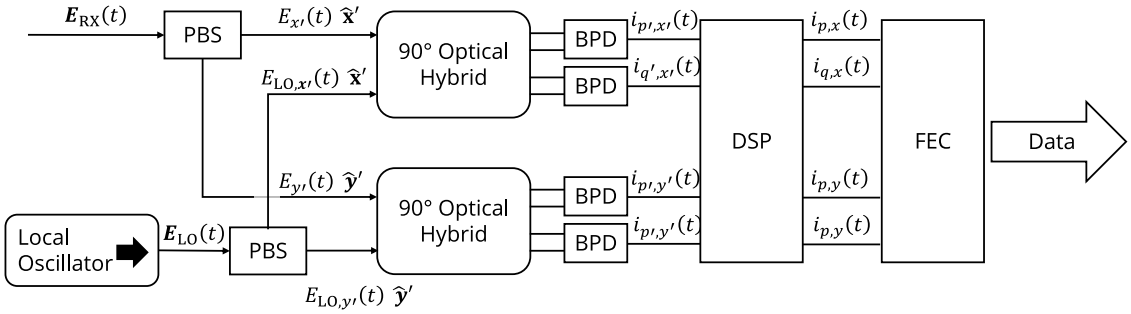

Figure 2.5: General structure of a receiver.

The general structure of the receiver is outlined in Fig. 2.5. The aim of a receiver is to decompose and demodulate each polarization and phase component from the received electric field

$$\begin{aligned}\mathbf{E}_{\mathrm{RX}}(t) &= E_{\mathrm{RX},x'}(t)\hat{\mathbf{x}}' + E_{\mathrm{RX},y'}(t)\hat{\mathbf{y}}' \\ &= \left[E_{\mathrm{RX},p',x'}(t) + E_{\mathrm{RX},q',x'}(t)\right]\hat{\mathbf{x}}' + \left[E_{\mathrm{RX},p',y'}(t) + E_{\mathrm{RX},q',y'}(t)\right]\hat{\mathbf{y}}' \,.\end{aligned} \tag{2.15}$$

$E_{\mathrm{RX},p',x'}(t)$ and $E_{\mathrm{RX},q',x'}(t)$ are respectively the in-phase and quadrature component on the x' polarization and $E_{\mathrm{RX},p',y'}(t)$ and $E_{\mathrm{RX},q',y'}(t)$ are the ones on the y polarization. It has to be noted that here the two orthogonal polarizations are called x' and y' in order to differentiate them from the ones at the transmitter side. This is because, unless polarization-maintaining fibers are used, typically the polarization reference is not the same. For similar reasons, the in-phase and quadrature components are here indicated with p' and q',respectively.

Inside the receiver, a laser acts as a local oscillator generating an electric field $\mathbf{E}_{\mathrm{LO}}(t)$, is separated into two orthogonal polarization states by a PBS along a $\hat{x}'$ and $\hat{y}'$ axis. The resulting fields are $E_{\mathrm{LO},x'}(t)\,\hat{\mathbf{x}}'$ and $E_{\mathrm{LO},y'}(t)\,\hat{\mathbf{y}}'$, respectively. Another PBS acts similarly on the received electric field, by separating it into $E_{\mathrm{RX},x'}(t)\,\hat{\mathbf{x}}'$ and $E_{\mathrm{RX},y'}(t)\,\hat{\mathbf{y}}'$. Then, for each of the two polarization states, both the received electric field $E_{\mathrm{RX},x'}(t)\,\hat{\mathbf{x}}'$ and the local oscillator $E_{\mathrm{LO},x'}(t)\,\hat{\mathbf{x}}'$ are mixed together by means of a 90° optical hybrid. The optical hybrid (Fig. 2.6) is a passive optical device having two main input ports and four output ports, and it is made of 3 dB couplers and a 90° phase rotator. For the x' polarization, the electric field at the output of each of the four ports ($E_{1,x'}(t)\,\hat{\mathbf{x}}'$, $E_{2,x'}(t)\,\hat{\mathbf{x}}'$, $E_{3,x'}(t)\,\hat{\mathbf{x}}'$ and $E_{4,x'}(t)\,\hat{\mathbf{x}}'$) will be a sum of the two input electric fields with a relative phase rotation of 0°,

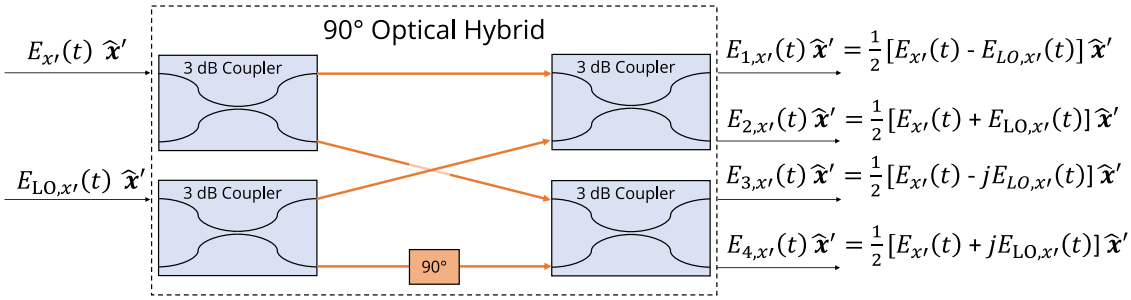

Figure 2.6: A possible arrangement of the 90° optical hybrid.

+180°, +90° and -90°, which results in

$$\begin{cases} E_{1,x'}(t) = \frac{1}{2}\left[E_{\mathrm{RX},x'}(t) - E_{\mathrm{LO},x'}(t)\right] \\ E_{2,x'}(t) = \frac{1}{2}\left[E_{\mathrm{RX},x'}(t) + E_{\mathrm{LO},x'}(t)\right] \\ E_{3,x'}(t) = \frac{1}{2}\left[E_{\mathrm{RX},x'}(t) - jE_{\mathrm{LO},x'}(t)\right] \\ E_{4,x'}(t) = \frac{1}{2}\left[E_{\mathrm{RX},x'}(t) + jE_{\mathrm{LO},x'}(t)\right] \end{cases} . \tag{2.16}$$

After the 90° optical hybrid, as drawn in Fig. 2.5, two balanced photodetector (BPD) are used to couple the electric fields $E_{1,x'}(t)$ and $E_{2,x'}(t)$ together and the electric fields $E_{3,x'}(t)$ and $E_{4,x'}(t)$ together. This process allows to extract the in-phase and the quadrature components of the x polarization state. In detail, the BPD extracting the in-phase component gives out an electric current ($i_{x',p'}(t)$) such that

$$\begin{aligned} i_{p',x'}(t) &= R\left(|E_{1,x'}(t)|^2 - |E_{2,x'}(t)|^2\right) \\ &= 4R\sqrt{P_{\mathrm{LO}}}\,E_{\mathrm{RX},p',x'}\,\cos\left(\phi_{\mathrm{LO}}\right) \end{aligned} \tag{2.17}$$

where R is a real number and it is the BPD responsivity, P_{LO} is the power of the local oscillator and ϕ_{LO} is the phase of the local oscillator.

Similarly, for $E_{3,x'}(t)$ and $E_{4,x'}(t)$, the corresponding current at the output of the second BPD will be

$$i_{q',x'}(t) = 4R\sqrt{P_{\mathrm{LO}}}\,E_{\mathrm{RX},q',x'}\,\sin\left(\phi_{\mathrm{LO}}\right) . \tag{2.18}$$

Then, by considering both the polarization states, the four electric currents at the output of the four BPD are

$$\begin{cases} i_{p',x'}(t) = 4R\sqrt{P_{\mathrm{LO}}}\,E_{\mathrm{RX},p',x'}\,\cos\left(\phi_{\mathrm{LO}}\right) \\ i_{q',x'}(t) = 4R\sqrt{P_{\mathrm{LO}}}\,E_{\mathrm{RX},q',x'}\,\sin\left(\phi_{\mathrm{LO}}\right) \\ i_{p',y'}(t) = 4R\sqrt{P_{\mathrm{LO}}}\,E_{\mathrm{RX},p',y'}\,\cos\left(\phi_{\mathrm{LO}}\right) \\ i_{q',y'}(t) = 4R\sqrt{P_{\mathrm{LO}}}\,E_{\mathrm{RX},q',y'}\,\sin\left(\phi_{\mathrm{LO}}\right) \end{cases} . \tag{2.19}$$

Then, the receiver first performs an analog-to-digital conversion of the four electric currents and, starting from these, the DSP recovers the phase and polarization and it also compensates for the chromatic dispersion and the PMD [75, 154, 168]. An accurate estimation of the disturbances due to the non-idealities of the transceiver is not always possible because vendors usually hide the implementative details of the transceiver and, in particular, the description of the implemented DSP algorithm. However, it is possible to perform a back-to-back (B2B) characterization of the device. In this way, all the internal impairments due to the specific transceiver implementation are included. Finally, in case a soft-forward error correction (FEC) is used, the recovered samples $i_{p,x}(t)$, $i_{p,x}(t)$, $i_{p,x}(t)$ and $i_{p,x}(t)$ are provided to the FEC module; otherwise, in presence of a hard-FEC, a threshold decision is performed on the recovered samples, and the bits are provided to the FEC module.

Finally, as long as the overall GSNR is above a certain threshold, the FEC module is able to correct most of the errors. It has to be remarked that, depending on the modulation format adopted, the threshold signal-to-noise ratio (SNR) will be different and this value depends on the specific DSP implementation and on the adopted FEC scheme.

2.1.6 An impairment-aware network abstraction

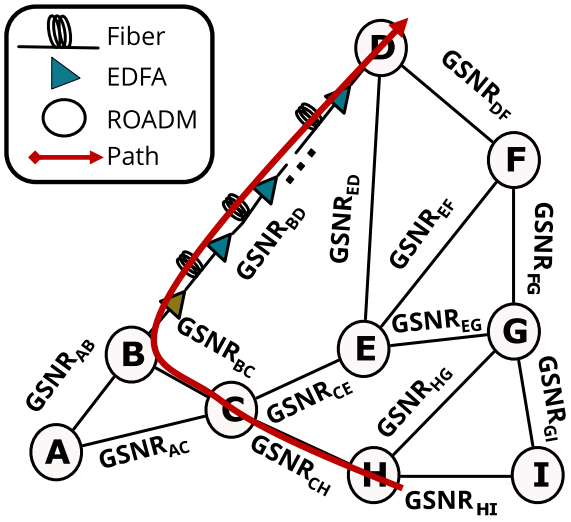

Figure 2.7: Physical layer abstraction of an optical network.

As shown in [70, 92], the GSNR is the metric for the QoT of a lightpath (LP) quantifying the propagation performance of an optical channel and it is defined as

$$\mathrm{GSNR} = \frac{P_s}{P_{\mathrm{ASE}} + P_{\mathrm{NLI}}} = (\mathrm{SNR}_{\mathrm{ASE}}^{-1} + \mathrm{SNR}_{\mathrm{NLI}}^{-1})^{-1} \tag{2.20}$$

where SNR_{ASE} is the SNR degradation caused by the amplifiers generating ASE noise and SNR_{NLI} is the SNR degradation caused by the NLI. Moreover, the overall GSNR of a LP can be decomposed in the contribution of each traversed link as:

$$\text{GSNR} = \left(\sum_{(i,j)\in \text{LP}} \text{GSNR}_{i,j}^{-1} \right)^{-1} \tag{2.21}$$

where $\text{GSNR}_{i,j}$ is the GSNR contribution of the link connecting the node i-th to the j-th node and it can be calculated by considering the GSNR contribution of each network element of the link as:

$$\text{GSNR}_{i,j} = \left(\sum_{k\in(i,j)} \text{GSNR}_{NE,k}^{-1} \right)^{-1} \tag{2.22}$$

where $\text{GSNR}_{NE,k}$ is the GSNR contribution of the k-th element of the link.

For this reason, the optical network can be abstracted by means of a weighted graph, as reported in Fig. 2.7, in which each node represents a ROADM node, while each edge represents a link that is weighted with the GSNR contribution of the link. This network abstraction can be used to evaluate the source-to-destination GSNR by accumulating the contribution of all the links along the path according to equation 2.21.

2.2 Routing and wavelength assignment

The RWA [122, 162] is the procedure of accommodating a request for a data connection between two nodes by tuning on a LP in the network, i.e., by dedicating some available spectral resources along a route to an optical signal.

The RWA problem can be approached in one-step as shown in [34, 122, 162], where both the routing and the wavelength assignment are treated as a single problem. However, the so called multistep methodologies treating separately the two problems are usually faster while leading to similar results [34] when the network is not heavily loaded (See Section 5.11 in [162] for more details). For this reason, this thesis will focus solely on multistep RWA methods.

In a multistep RWA, first the routing space is computed, i.e., the set of explored paths, and then the wavelength assignment is attempted. In detail, in this thesis the routing space is always pre-computed according to a k-shortest path (KSP) algorithm [164], which provides a set of k paths that are sorted from the shortest to the longest. As the paths are computed over a weighted graph, different metrics can be used as weight of the edges; common strategies are: uniform weight in which every link has weight 1, the link length and the GSNR degradation for impairment awareness purposes as described in Section 2.1.6. In detail, the uniform weight has

the main advantage of minimizing the probability of wavelength contention since it attempts to minimize the number of traversed ROADM nodes; while, when the link length is used, the routing algorithm aims at minimizing the travelled distance and therefore, at minimizing the latency; finally, the GSNR degradation allows an impairment-aware RWA [29, 73, 140] which targets the maximization of the GSNR of the paths and consequently the maximization the capacity of each LP.

Moreover, many wavelength assignment strategies have been proposed [162]. The most popular ones are the *first-fit* strategy in which all the wavelengths are attempted from the lowest to the highest and the *most-used* strategy, where the wavelengths are explored from the most used in the network to the less used. However, all the wavelength assignment methodologies present similar performances while the first-fit preserves the advantage of not requiring any global knowledge about the current state of the network [162]. For this reason, the results of this thesis are based on the first-fit approach.

Therefore, the RWA algorithm used to obtain the results depicted in this thesis is structured as follows:

1. at the beginning the routing space of the network is pre-computed;
2. every time a new request for connection arrives, the allocation of a LP is attempted, exploring the wavelength availability from the shortest path to the longest one according to the first-fit strategy;
3. if the network resources are available and the path is feasible the LP is allocated, otherwise the request is blocked.

This strategy is based on a wave-plane heuristic algorithm for RWA [160].

2.3 Outline of the remainder of the thesis

This thesis focuses on the topic of physical layer aware open optical networking. Therefore, it is introduced the QoT estimation in an open and disaggregated optical network, by investigating several physical layer technologies to enhance the network capacity, and by presenting analysis and experiments on the network design, planning and automation. In detail, chapter 3 first, introduces the open source Python software called GNPy [61] whose core is a vendor-agnostic quality of transmission estimator (QoT-E) for open optical networks and then, it reports the stimulative and the experimental validation campaign of this QoT-E conducted first in the Microsoft laboratory and then over a portion of the Microsoft core network. Chapter 4 focuses on analyzing the multi-band transmission technology by first proposing a simplified power optimization strategy for a C+L line system and then by assessing the capacity enhancement led by multi-band transmission in point-to-point scenarios. Then, chapter 5 focuses on network analysis and design by using

an offline tool (offline physical layer assessment (OPLA) [65]) and a dynamic traffic allocation based tool (statistical network assessment process (SNAP) [22, 37]). In detail, chapter 5 focuses first on an offline strategy for deploying Raman amplification in order to enhance the QoT of the paths and consequently, the network capacity. Then, the chapter analyses the benefit of employing Raman amplification and advanced DSP techniques to reduce the costs of the network by reducing the number of optical-electrical-optical (OEO) regenerators in the network. Afterwards, chapter 5 reports some comparison among different technological solutions by means of SNAP. First, different SDM technologies are compared with each other and then, SDM has been compared with multi-band transmission. Moreover, chapter 6 reports the integration and the subsequent validation of a QoT-E in the programmable optical network (PROnet) orchestrator [111] in order to enable physical layer aware multi-layer network orchestration and automation. Finally, in chapter 7 the closing conclusions are drawn.

The main contributions of the thesis include:

- the development of the GNPy QoT-E and its validation campaign;
- the multi-band optimization strategy and the multi-band capacity assessment;
- the development offline network analysis tool called OPLA and the related analysis;
- all the comparative analysis on physical layer technologies;
- the integration and validation of the QoT-E into the PROnet orchestrator.

Chapter 3

GNPy: an open source software to abstract Open Optical Networks

Over the years, many open source projects and open platforms for physical-layer assessment have been developed. In [41], together with an extensive numerical validation, the source code to estimate the non-linear interference is provided. Furthermore, the source code of the inter-channel SRS GN-model [155] is available on GitHub [157]. Moreover, the QAMpy [151] project provides an open source Python library to simulate the DSP of an optical communication system. The DSP library [129] provides similar fucntionalities for Matlab users. In addition, the Claude [90] library provides Python functions and machine-learning models for optical communications. Finally, BOW [16, 185], a real-time open source optimizer for optical networks, has recently been announced and published.

This chapter focuses on GNPy [2, 61], which is an open source Python software developed by the physical simulation environment (PSE) working group[1] for assessing the physical layer propagation performances of an optical network by means of its QoT-E. Also, GNPy is the *driving force* of all the analysis done in this thesis.

This chapter is structured as follows: section 3.1 describes the structure of GNPy, section 3.2 reports the stimulative validation of the QoT-E [28] adopted by GNPy by comparing it to a split-step Fourier method (SSFM) simulation [130] over a C+L HFA amplified line system. Then, section 3.3 describes the experimental validation of the GNPy QoT-E first, over a commercial network in the Microsoft laboratory [60], and then, over a network segment of the Microsoft backbone network [66].

The material reported in this chapter was previously published in [28, 59, 60, 61].

[1] As part of the PSE working group within the Telecom Infra Project (TIP), I have been part of the development team of GNPy.

3.1 General Structure of GNPy

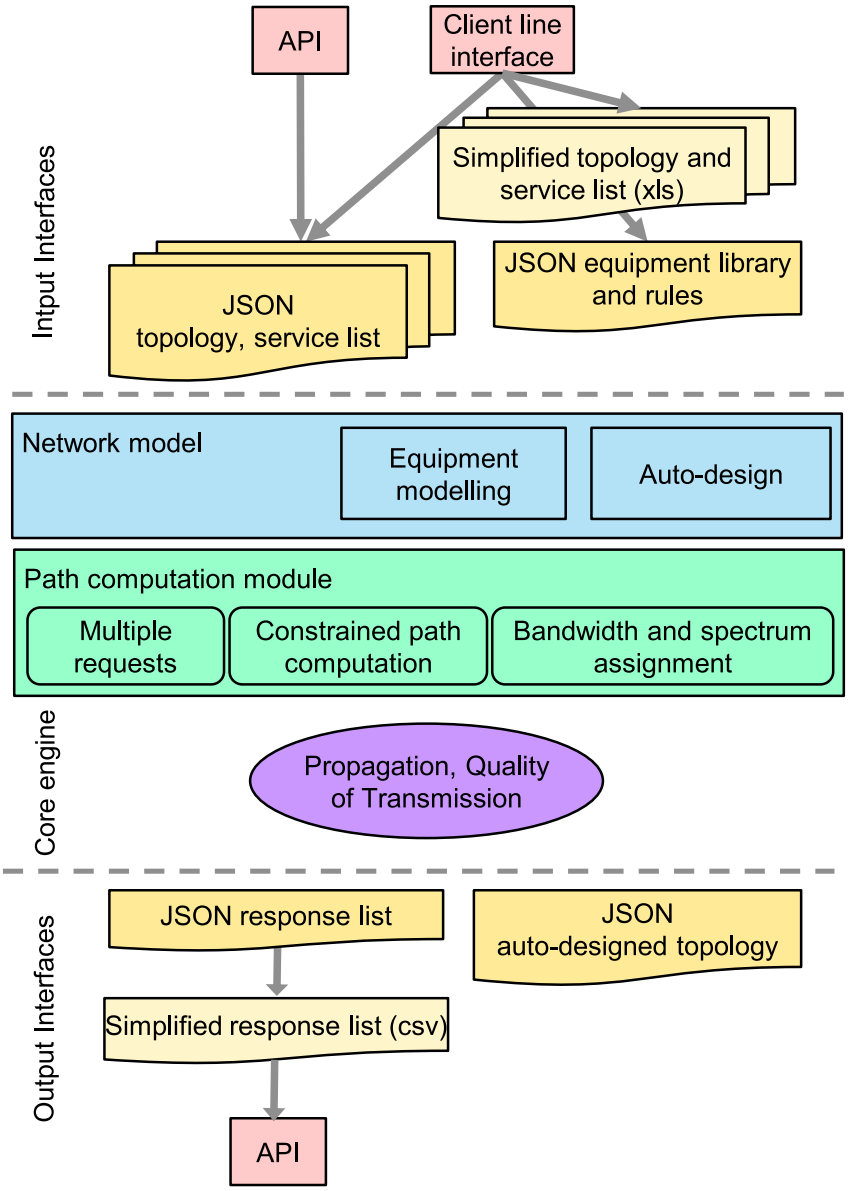

Figure 3.1: The structure of GNPy.

The general structure of GNPy is depicted in Fig. 3.1. GNPy requires a set of input files describing the topology of the network, the equipment characteristics and the list of services to be provisioned. These parameters can be provided either in JavaScript object notation (JSON) format, or as a set of XLS files that are then internally mapped into the equivalent JSON structure.

The topology file contains the list of *network elements* (transceivers, ROADM

nodes, fibers and amplifiers) and a description of how the elements are connected together to describe the network you want to represent. The *network model module* uses the topology file together with the equipment file to create a digital twin of the represented network by using a DiGraph object from the NetworkX Python library [80]. Each network element is defined by its physical parameters. Thus, a fiber element requires the knowledge on the fiber length, the attenuation coefficient, the dispersion coefficient, the non-linear coefficient, the Raman efficiency, the PMD coefficient and the input and output connector losses. Moreover, in the presence of Raman amplification, it is possible to define also the power and the frequency of the Raman pumps injected into the fiber. The amplifiers may be described according to four different models [9] depending on the level of knowledge of the device:

1. a *detailed* model that allows the user to define a precise noise figure (NF) versus gain curve and the gain/NF tilt and ripple;

2. a *variable-gain model* that can be used when the knowledge is limited to a small amount of NF-gain values, then, the actual NF is computed according to a dual stage model [9].

3. a simple *fixed-gain model* that requires only the actual gain and the actual NF;

4. a *black-box model* proposed in the OpenROADM amplifier working group [12], for the cases in which the attenuation of the output variable optical attenuator (VOA) is unavailable and thus, the actual amplifier gain can not be retrieved and, the NF vs gain characterization can not be used. In this case, GNPy uses a polynomial NF vs input power (P_{in}), that includes the VOA optimization algorithm.

This capability of supporting different amplifier models is a key to enable a multi-vendor application. The ROADM elements are defined by the wavelength selective switching (WSS) output power per channel and the add/drop optical signal-to-noise ratio (OSNR) contribution. Finally, the parameters of the transceiver elements include the frequency range and the transceiver operation modes witch define the modulation format used, the baud rate and the required GSNR necessary to consider the mode as feasible. Based on these equipment models, a user can define a configuration provided that the whole set of attributes are available. However, such a precise description may be unavailable. For this reason, the network model module offers an *auto-design* tool able to determine the amplifier configuration for a possible deployment according to a set of design rules and heuristics that are described in [9].

The *path computation module* uses the list of services to enable the propagation of multiple requests on the same simulated network using the same configuration of equipment and it make use of the QoT-E to compute the path feasibility. Typical

planning constraints are supported such as path disjunction, mandatory nodes to be crossed, spectrum assignment and transponder mode selection. The interface to this feature is a JSON file whose structure is inspired by [19].

The GNPy features are structured around its QoT-E which is the core engine taking care of simulating the propagation of a WDM comb along a path in the network and then, it returns the GSNR of each channel together with the accumulated dispersion and the PMD. This information is used to determine the feasibility of each operating mode of the transceivers.

The GSNR, is computed as depicted in chapter 3 and, in particular, the NLI is evaluated according to the GGN-model.

The path computation module enables the development of an application program interface (API) for the integration with a line system controller. For instance, an API was recently featured in an open disaggregated transport network (ODTN) [20] demonstration [101] with the Czech Light Open Line System [100]. Moreover, in Sodium-SR2 release of the TransportPCE controller project [51] the path feasibility estimation has been delegated to GNPy.

3.2 Simulative validation through split-step simulation

The first step was to validate the QoT-E of GNPy via simulation. This step is necessary since a QoT-E using the GGN-model for computing the NLI was not yet validated for multi-band systems and in presence of Raman amplification [28]. For this purpose, the GGN-model is compared to the SSFM simulation of a C+L transmission link with hybrid EDFA-Raman amplification. The simulations are performed by solving the Manakow equation via full time-domain SSFM as described in [130].

3.2.1 System description

The schematic of the simulated setup is shown in Fig. 3.2. 161 WDM channels are generated in the 50 GHz dense wavelength division multiplexing (DWDM) grid: 83 C-band channels and 78 L-band channels. The two bands are separated by a 300 GHz guard-band and thus, the total optical bandwidth is 8.3 THz. Fig. 3.3a shows the normalized optical power spectral density of the transmitted signal, divided into the C- (green) and the L-band (yellow).

Each WDM channel is PM-16QAM modulated with 15% roll-off RRC spectrum and the symbol rate is 32 GBaud. The WDM comb thus generated is propagated through 10 80 km long spans of SSMF, whose parameters are reported in table 3.1. Given the large occupied bandwidth, the attenuation was not considered flat in

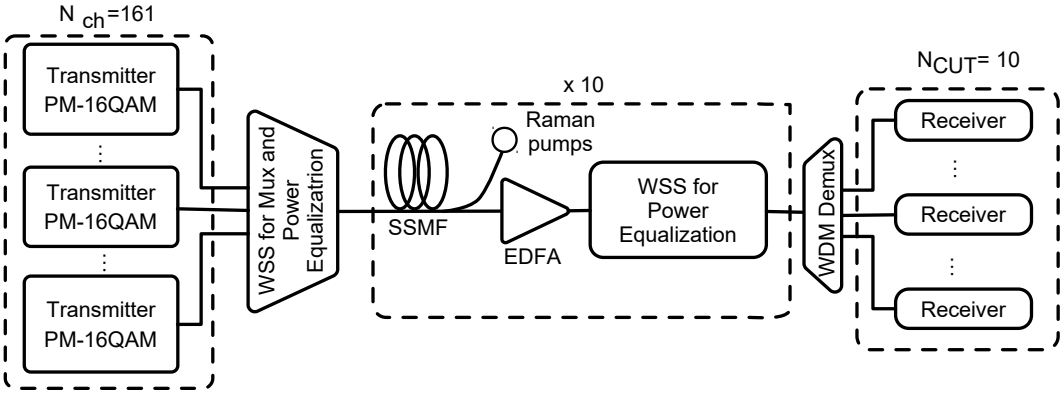

Figure 3.2: Simulated system.

Table 3.1: Fiber Parameters.

Parameter	**Value**
Span length	$L_s = 80$ km
Maximum number of spans	$N_s = 10$
Chromatic dispersion	$D = 16.7$ ps/nm/km
Nonlinear coefficient	$\gamma = 1.3$ 1/W/km
Polarization Averaged Raman Coefficient	$C_r = 0.39$ 1/W/km
Polynomial coefficients of $\alpha(f)$ with $f_0 = 193.6$ THz	$\alpha_0 = 0.19$ dB/km $\alpha_1 = 5.97 \times 10^{-5}$ dB/km/THz $\alpha_2 = 8.3 \times 10^{-4}$ dB/km/THz^2

frequency, but it changes according to

$$\alpha(f) = \alpha_0 + \alpha_1(f - f_0) + \frac{1}{2}\alpha_2(f - f_0)^2 \quad [\text{dB/km}] \,. \tag{3.1}$$

The parameters are reported in table 3.1. Since the dispersion slope introduces considerable computational overheads in the SSFM simulation, we did not include it in our analysis. Moreover, as shown in [155], the impact of the dispersion slope in the generation of the NLI is completely overcame by the SRS.

The transmitted WDM spectrum has been considered flat, with a transmitted power per-channel of -3 dBm, which gives an overall total launch power of 19.1 dBm. After each span, an ideal - the insertion loss is neglected - WSS equalizes the power per-channel to restore the transmitted spectrum.

The amplification site is made of a Raman amplifier - using 5 counter-propagating Raman pumps - and an EDFA amplifier having a NF of 4 dB. The frequency and

Table 3.2: Parameters of the Raman amplifier's pumps.

	Pump 1	**Pump 2**	**Pump 3**	**Pump 4**	**Pump 5**
Power	250 mW	300 mW	150 mW	150 mW	150 mW
Frequency	201.07 THz	202.43 THz	203.11 THz	203.80 THz	204.50 THz

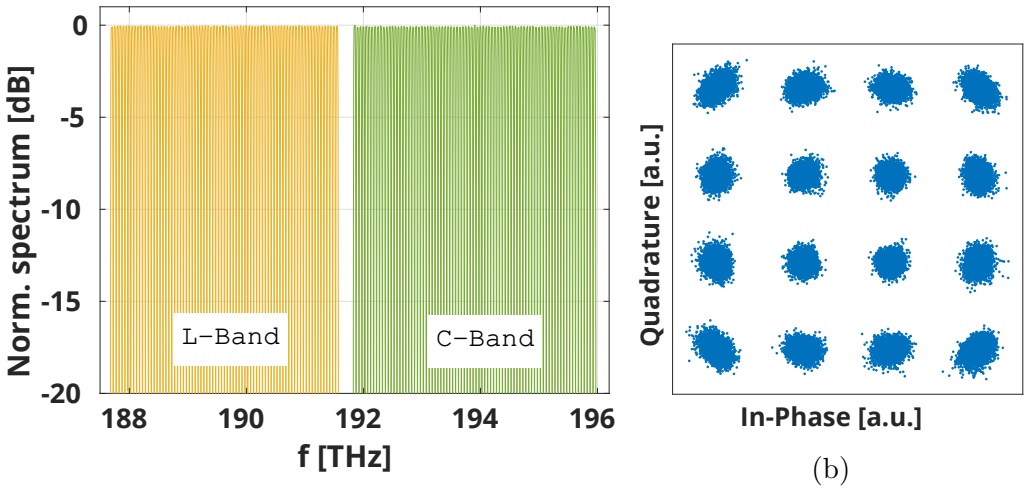

(a) (b)

Figure 3.3: Transmitted C+L spectrum (a) and received constellation after 10 spans (b). L-band channels are depicted in yellow, while C-band channels are depicted in green.

the power of the pumps are reported in the table 3.2. The overall Raman gain is shown on Fig. 3.4a. Notably, that the Raman gain is not flat, introducing a tilt of ~ 8 dB. We assume that the EDFA and the WSS are able to recover for the power non flatness by equalizing the channel powers in order to achieve span transparency. In this way the PSD of the signal at the beginning of each span is always the same.

Fig. 3.4b reports the power evolution of three channels spread across the WDM comb (at 187.9 THz, 191.3 THz and 195.7 THz), highlighting how different frequencies undergo different power variations. For all channels, first, power decreases due to fiber attenuation, then, towards the end of the span, it increases due to the Raman amplification. L-band channels achieve transparency. The C-band channel, instead, does not fully achieve transparency, as they get depleted by SRS, transferring power to the L-band channels.

At the receiver, 10 channels-under-test (CUT)s are filtered and received simulating a coherent receiver. The central frequencies (f_c) of the CUTs are: 187.7 THz, 189.65 THz, 191.55 THz, 191.85 THz, 193.9 THz and 195.95 THz. The CUTs are generated by repeating 6 times 2^{14} pseudo-random binary sequence (PRBS)

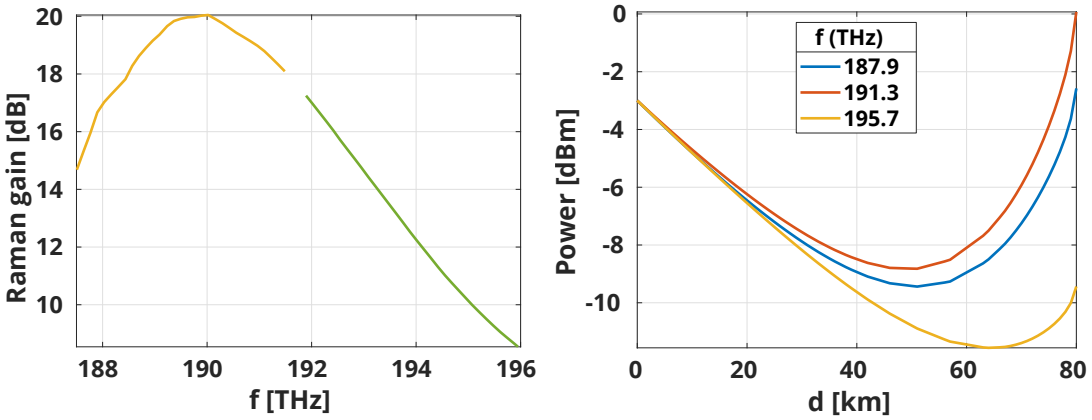

(a) (b)

Figure 3.4: (a): Raman gain, including inter-channel SRS and Raman gain, at the end of the 80 km span. C-band is depicted in green, and L-band is depicted in yellow. (b): Power evolution across a span of three WDM channels.

sequences, while the other channels are generated with random PM-16QAM symbols. The receiver uses a fully-data-aided fractionally-spaced 17-tap least-mean-square (LMS) based adaptive equalizer, and the GSNR is evaluated on the received constellation. A received constellation, without ASE noise, is shown in Fig. 3.3b. As the lasers are assumed ideal, the phase recovery is not applied and thus, it can be observed a slight amount of phase noise caused by the NLI. Nevertheless, in the presence of ASE noise, this small phase noise does not significantly affect noise statistics, keeping the GSNR estimation reliable [134].

3.2.2 Results and discussion

Fig. 3.5 compares the GSNR resulting from the numerical simulation (diamond markers) against estimations (solid lines) computed using the GGN-model after the 5^{th} (blue) and the 10^{th} (red) span. Moreover, the light color bars represent a 1 dB margin, which are positive-only as the model slightly overestimates the NLI power [136] because of the signal Gaussianity assumption on which the model is based.

Outcomes show larger NLI in the L-band with respect to the C-band. This is due to the SRS that causes a power transfer from the C-band channels toward the L-band channels, and this enhances the NLI generation in the L-band. For the same reason, the C-band performance is limited mainly by the ASE noise.

The GGN-model gives a good and conservative prediction and thus, the GSNR is accurately predicted across the full WDM comb, as all the results are inside the 1 dB margins. Moreover, the GGN-model properly predicts the GSNR variation across the spectrum, delivering consistent QoT estimations across the channel

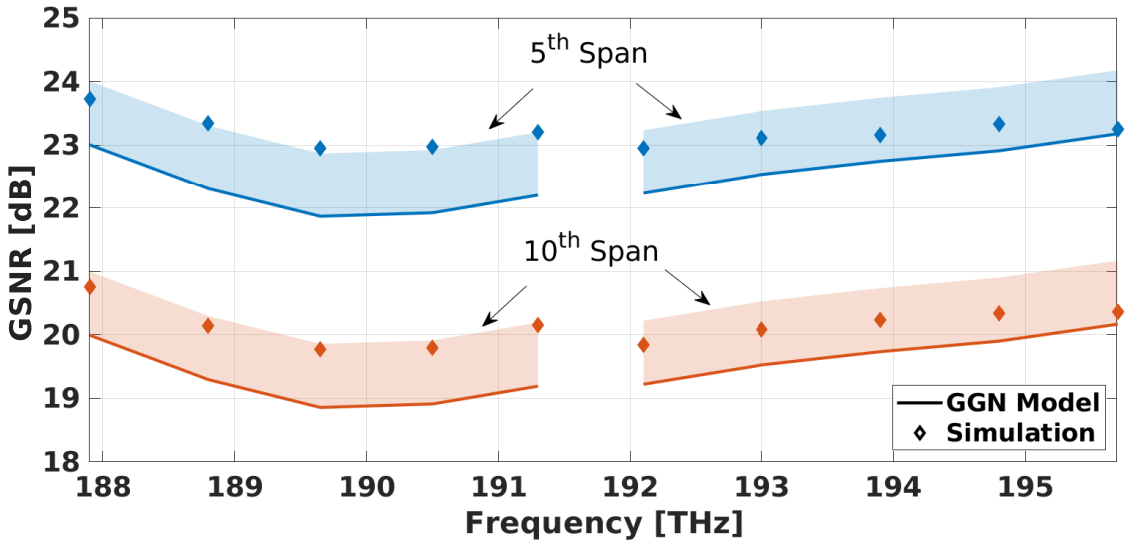

Figure 3.5: Comparison of simulation results vs GGN-model estimation after 5 spans (blue) and after 10 spans (red).

comb. Furthermore, the model predictions are closer to the simulation results for the 10 spans case, as the signal gets closer to the Gaussian-distributed assumption because of the chromatic dispersion.

3.3 Experimental Validation Campaign

Many validations of GNPy have been held [57, 60, 66, 70, 79, 167]. Among them, here are reported the one held in the Microsoft laboratory [60] as it is the most extensive and complete and the validation over the Microsoft core network as it is the only one carried out on a production network. In what follows, there is described the validation methodology, followed by the description of the two validations.

3.3.1 Methodology

The goal of the validation campaign aims at proving the prediction capability of GNPy for real commercial line systems by comparing the actual GSNR measured by the transceivers and the GSNR estimated by GNPy relying only on measurements provided by the network equipment and the parameters provided by the data-sheets of the network equipment.

In order to obtain all the information describing the state of the network required by GNPy to compute the GSNR estimation, it is necessary to know the power per channel of each ROADM node right after the WSS. Such information

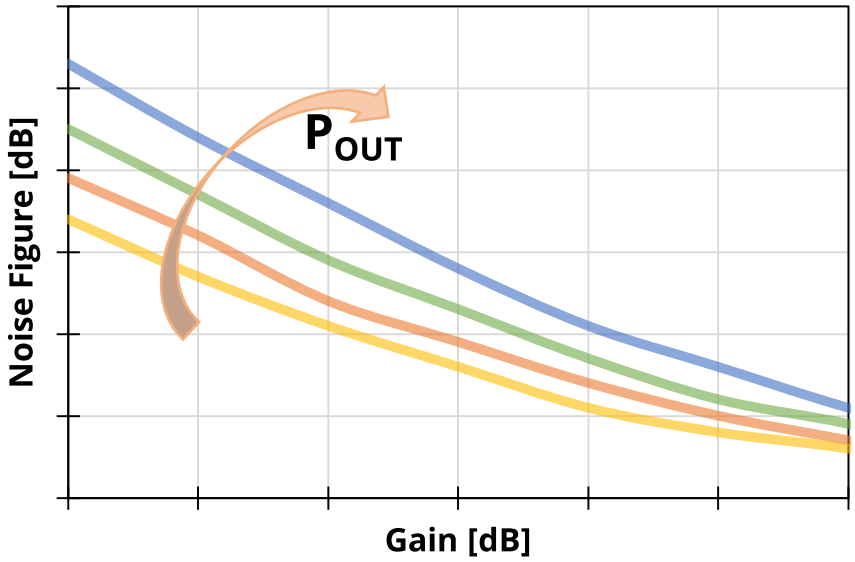

Figure 3.6: Example of NF-vs-gain and P_{out} curves – the plot is for illustration purpose only and does not refer to any real amplifier –.

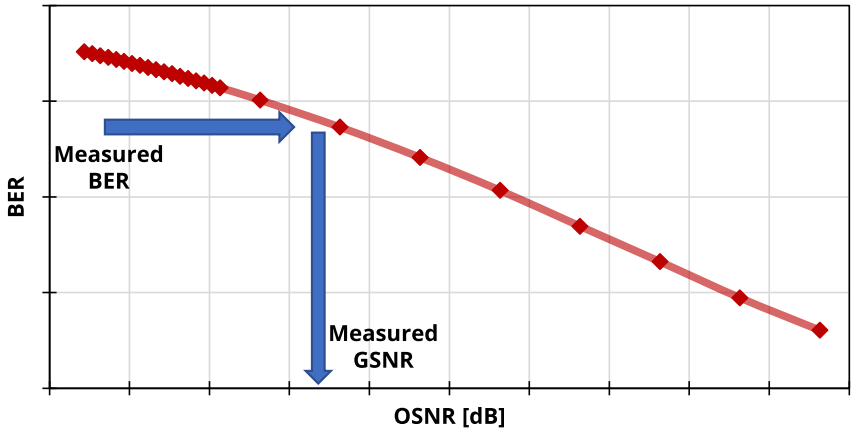

Figure 3.7: Qualitative example of the B2B BER-vs-OSNR characteristic of the transponder and the derivation of GSNR from a BER measurement - the curve is for illustration purpose only and do not refer to any real transceiver -.

can be retrieved from the total input power measured by each BST amplifier divided by the number of optical channels. Then, each optical amplifier (OA), including BSTs, ILAs and pre-amplifiers, requires the actual gain, the tilt target and the NF characterization. The gain and the tilt can be retrieved probing the Microsoft software defined network (SDN) line system monitoring tool via representational state transfer (REST) [69] query or directly by the equipment via network configuration protocol (NETCONF) [49], whereas the NF characterization, describing the NF depending on the amplifier gain and the output power (P_{out}) can be obtained by the amplifier data-sheet. A qualitative example of NF-vs-gain and P_{out} is shown

in Fig. 3.6. In order to fully describe each fiber span connecting two consecutive OAs it is necessary to known the fiber type, the fiber length (L_F), the attenuation coefficient (α) and the losses of the connectors. Moreover, in presence of Raman amplifiers, it is also necessary to know the parameters of the Raman pumps and the fiber temperature. GNPy provides already the propagation parameters for the following fiber types: SSMF (ITU-T G.652 [33]), the non-zero dispersion-shifted fiber (NZDSF) (ITU-T G.655 [32]), the large effective area fiber (LEAF). However, the library of fiber types can be easily extended by introducing new types. To achieve that, it is necessary to know the dispersion coefficient (D), the non-linear coefficient (γ), and the Raman efficiency (C_r). The length L_F can be obtained by the optical fiber network (OFN) deployment report if available or by the network equipment by measuring the propagation time between the two OAs if possible or by computing the geographical distance between the amplification sites. Furthermore, the attenuation coefficient can be derived knowing the fiber type or it can be read from the data-sheet. Moreover, the losses of the connectors can be derived knowing the overall span loss (A_s), which can be computed knowing the power at the output of the previous OA and the one at the input of the next OA measured by the on-board photodiodes. Thus, knowing A_s, the total splice-plus-connector loss (A_c) can be derived knowing L_s and α as:

$$A_c = A_s - A_F = A_s - \alpha \times L_F \ , \tag{3.2}$$

where A_F is the loss introduced by the fiber itself. Then, the proper partition of these losses is crucial since the connector loss determines the NLI that is generated by the fiber propagation. The best way would be to use an optical time domain reflectometer (OTDR) trace providing the measurement of the losses along the fiber but this is not always available. Because of that, it is necessary to make an assumption on the value of the input connector loss. In our analysis we use 0.75 dB as it is a typical value as reported in [166] and it was used in [57, 70]. The remaining loss is then assumed to be at the end of the fiber span. Moreover, the fiber temperature, if not known, can simply be assumed equal to 295 K room temperature. Finally, the Raman amplification has to be described through the power and the frequency of each Raman pump. The pump frequency can be found in the data-sheet of the Raman amplifier while the pump power can be retrieved by performing a query to the Raman amplifier. This procedure has been followed for each ROADM node, each OA and each fiber in the network and the resulting information has been provided to GNPy to compute the GSNR of each path and each channel.

In order to measure the actual OSNR we used the built in functionality of the optical spectrum analyzer (OSA) when it was available. In particular, the actual ASE noise is estimated by measuring the power at the left and at the right side of the channel and then by computing the average as shown in [43].

In order to obtain the actual GSNR we queried each transponder to retrieve the actual bit-error-rate (BER) and then, by inverting the B2B BER-vs-OSNR characterization of the transceiver as qualitatively depicted in Fig. 3.7. Such procedure has been carried out taking into account the modulation format as the B2B curve depends on it.

In conclusion the error on each estimation has been defined as the difference between the measurement and the estimation. In such a way, positive errors are conservative and negative errors are non-conservative.

3.3.2 Experimental multi-vendor validation in the Microsoft laboratory

In this subsection, the lab validation setup and results are reported and commented on.

Test-bed Description

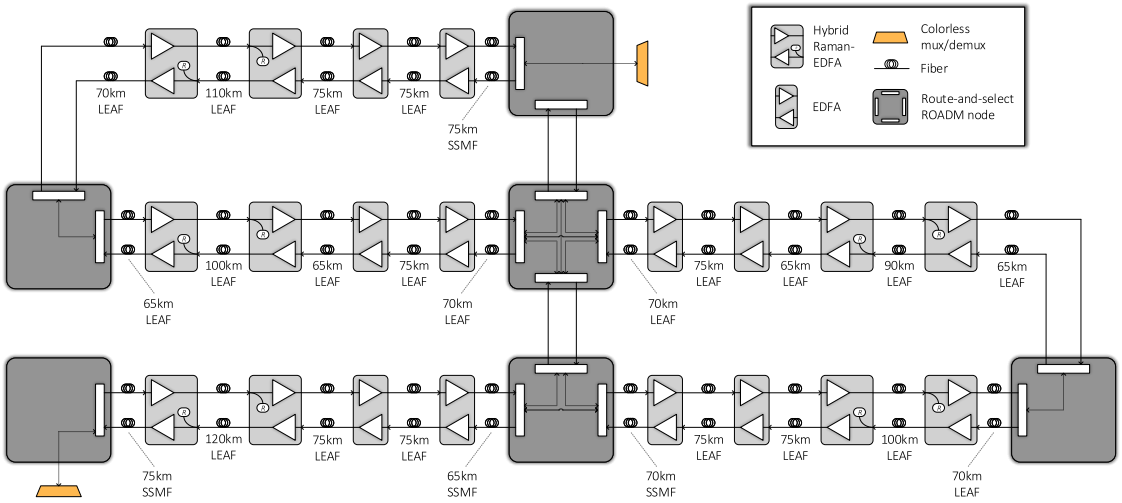

Figure 3.8: The block diagram of the Microsoft test-bed.

Table 3.3: Fiber parameters.

Fiber type	α (dB/km)	D (ps/nm/km)	γ (1/W/km)
SSMF	0.2	16.7	1.27
NZDSF	0.222	3.8	1.45

Fig. 3.8 depicts the test-bed which emulates a commercial network. It includes six ROADM nodes, five amplified links and colorless mux/demux used to insert

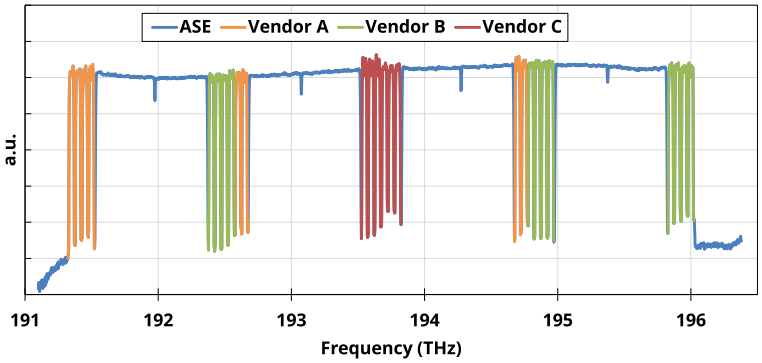

Figure 3.9: An OSA measurement of the transmitted WDM comb. Channels from different vendors and the ASE noise are reported with different colors.

Figure 3.10: A photo of the network equipment.

and extract the signals from the network. The longest bidirectional path in this network is 2000 km. The transponders comes from three different vendors (Vendor A, B and C), while the line system comes from a fourth vendor (Vendor D).

Each ROADM node includes a booster amplifier and a pre-amplifier for each node degree. Each amplified link is ∼400 km long and it includes tree lumped EDFAs and one HFA. The network involves both ITU-T G.652 [33] SSMFs and LEAF fibers which propagation parameters are reported in table 3.3. Moreover, the fiber span length varies from 65 km to 120 km. The exact location of each OA type, the fiber type and the span length are reported in detail in Fig. 3.8. Furthermore, each amplifier and ROADM have been configured for optimal performance by the vendor proprietary controller.

The normalized PSD of the transmitted WDM comb is shown in Fig. 3.9 and it has a bandwidth occupation of 4.7 THz, between 191.3 THz and 196 THz. The commercial transponders generates a total of 26 channels grouped into five media-channels (MC): three MCs made of six channels and two MCs made of four channels. The channels fit into the 50 GHz WDM grid and are distributed as follows: two MCs at the edges of the spectrum, a third MC in the middle and the last two MCs in the midpoints between the central MC and the external ones. The remaining portion of the spectrum has been filled with ASE noise as shown in [48] to reach the full spectral load. The signals are RRC shaped having a symbol rate of 34.16 GBaud and the roll-off is 0.2. All the transponders support the PM-QPSK, the PM-8QAM and the PM-16QAM modulation formats.

To collect the needed data from the network, the network equipment has been probed by means of the Microsoft SDN line system monitoring tool which is based on REST [69].

Several combinations of distances and modulation formats are investigated: PM-QPSK at 2000 km and 4000 km, PM-8QAM at 400 km, 800 km, 1200 km, 1600 km and 2000 km and PM-16QAM at 400 km, 800 km and 1200 km, both in forward and in backward directions. In order to obtain a 4000 km path, the signals have been looped back over the 2000 km path. Furthermore, the 2000 km path with PM-8QAM has been tested also without Raman amplification. In this case the EDFAs gain has been adjusted to compensate for the absence of Raman gain.

Results and discussion

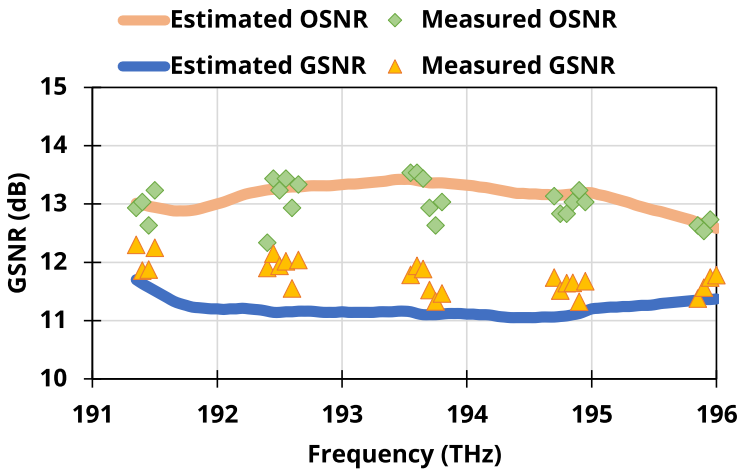

Figure 3.11: Comparison of the measured and the estimated OSNR and GSNR for the PM-8QAM @2000 km

The first observed case is the 2000 km in forward direction with PM-8QAM modulated signals. For this scenario, Fig. 3.11, both the estimated OSNR (orange line) and the GSNR (blue line) are compared to the measurements (diamond markers and triangular markers, respectively). The OSNR has been measured with an OSA by means of its built-in OSNR estimation program, while the GSNR has been measured by inverting the B2B curve of the transceivers as described in section 3.3.1. This first result shows a good accuracy in the estimations as, except for the outliers at 192.4 THz and at 193.75 THz, the estimated OSNR has an error within 0.4 dB and the estimated GSNR has an error within 1 dB. Moreover, the estimations show a good capability in predicting the frequency variation of both the OSNR and the GSNR. It can also be noted that the GSNR prediction is always conservative as expected by the GGN-model for which the NLI estimation is the worst case.

Later, a power sweep has been performed, i.e., the transmitted power has been swept by a power offset between -3 dB and +1 dB and the GSNR has been measured. The results of the power sweep are reported in Fig. 3.12, where the measured

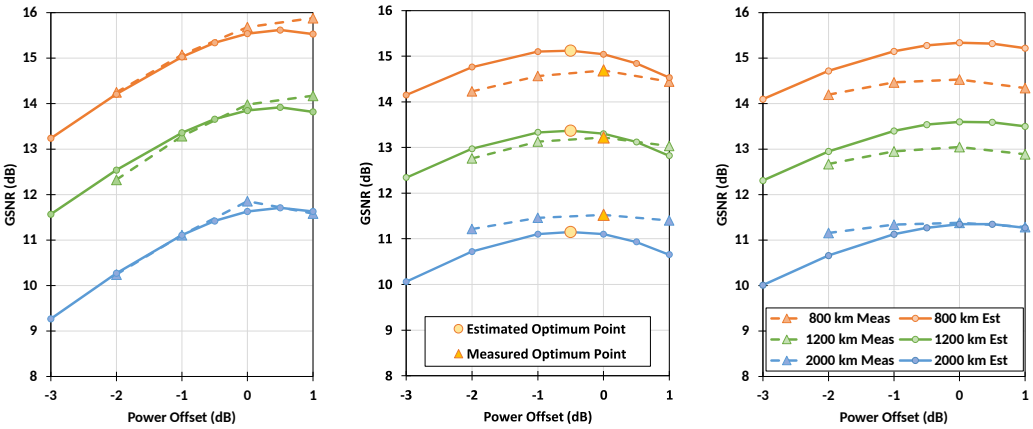

(a) Channel #2 at 191.4 THz.

(b) Channel #48 at 193.6 THz.

(c) Channel #92 at 195.9 THz.

Figure 3.12: GSNR comparison of the estimation and the measurement in a power sweep for PM-8QAM. The legend shown in (c) applies to all three graphs.

GSNR (solid lines) and the estimated GSNR (dashed lines) are compared for the channels #2 (Fig. 3.12a), #48 (Fig. 3.12b) and #92 (Fig. 3.12c) at 191.4 THz, 193.6 THz and 195.9 THz respectively - the two at the edges and the one in the middle of WDM comb -. The power sweep has been performed at 800 km (orange), 1200 km (green) and 2000 km (blue). Fig. 3.12b also reports the estimated optimum power (yellow circular marker) and the measured one (yellow triangular marker) defined as is the power maximizing the GSNR of the central channel according to the local-optimum global-optimum (LOGO) [138].

In this case, GNPy demonstrates good accuracy in predicting the GSNR, even when the network is in the linear regime - the transmitted power is smaller than the optimum - and in non-linear regime - the transmitted power is larger than the optimum -. Moreover, the error in the predicted optimum power is always within 0.5 dB, demonstrating that GNPy can also be used by a line system controller to optimize the network.

Figs. 3.13, 3.14 and 3.15 show the estimated GSNR (blue line) and the measured GSNR (orange markers) for PM-8QAM, PM-QPSK and PM-16QAM respectively. The results are reported for several distances and for both the forward and the backward paths. Moreover, Figs. 3.16 report the results when the Raman amplification is disabled. It can be noted that, for each path, the estimated GSNR is the same for all the modulation formats. This is due to the GGN-model, which neglects the impact of the modulation format. However, as shown by the measurements, the modulation format does not impact significantly the GSNR. The 400 km paths, (Figs. 3.13a, 3.13f, 3.15a and 3.15d) present a larger inaccuracy the middle of the band. Then, increasing the distance the error decreases since the GSNR reduction

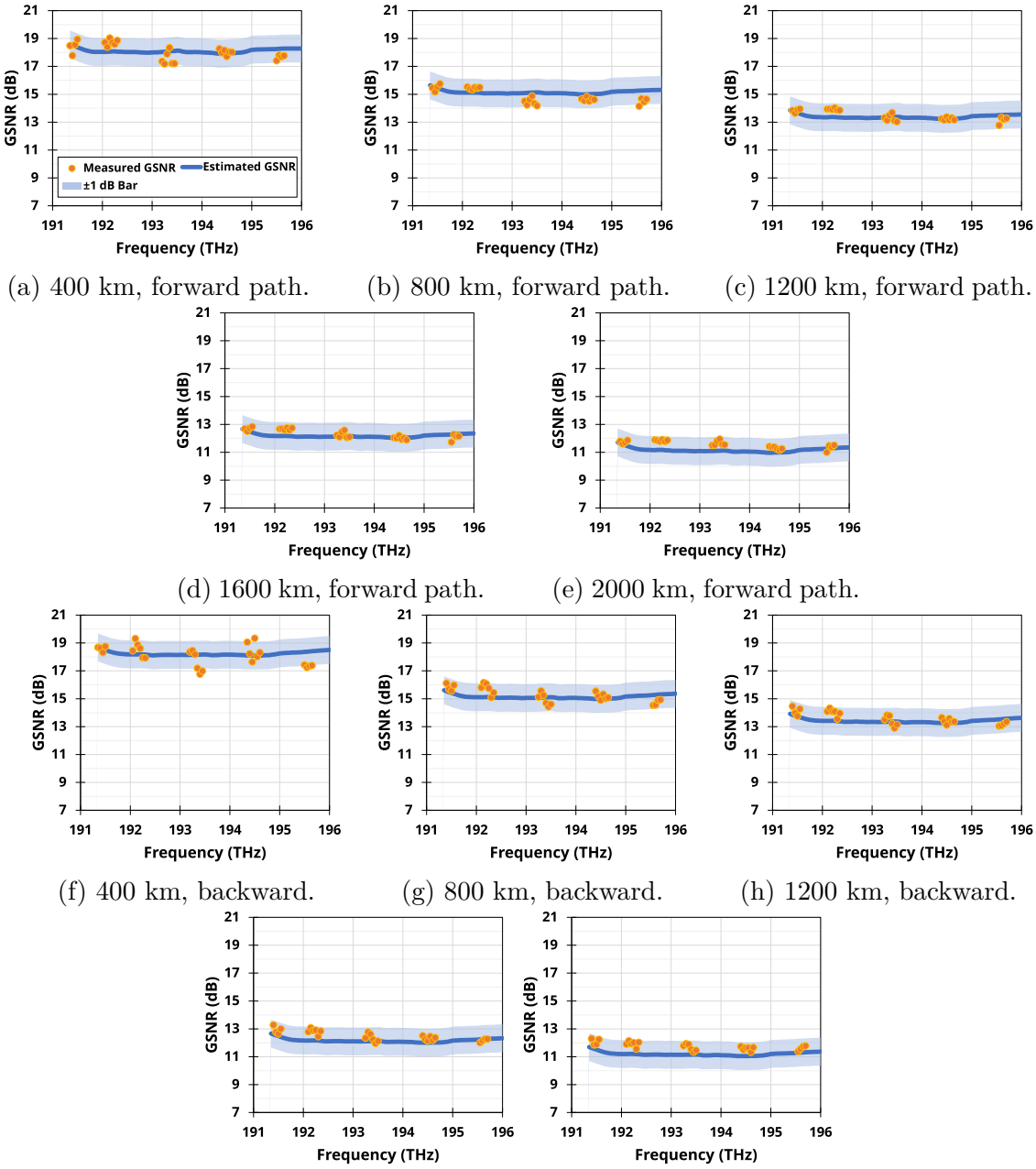

(a) 400 km, forward path. (b) 800 km, forward path. (c) 1200 km, forward path.

(d) 1600 km, forward path. (e) 2000 km, forward path.

(f) 400 km, backward. (g) 800 km, backward. (h) 1200 km, backward.

(i) 1600 km, backward. (j) 2000 km, backward.

Figure 3.13: Comparison of the estimation with the measurement for PM-8QAM.

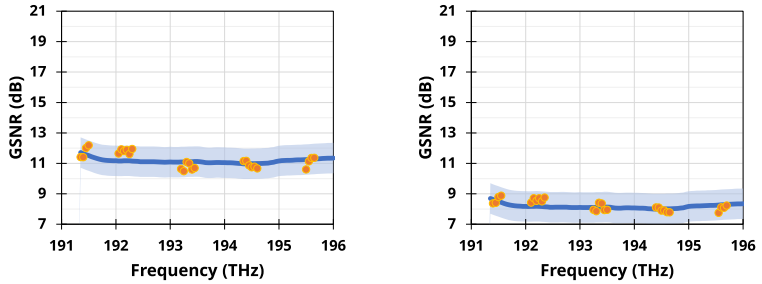

(a) 2000 km, forward path. (b) 4000 km, loop-back.

Figure 3.14: Comparison of the estimation with the measurement for PM-QPSK.

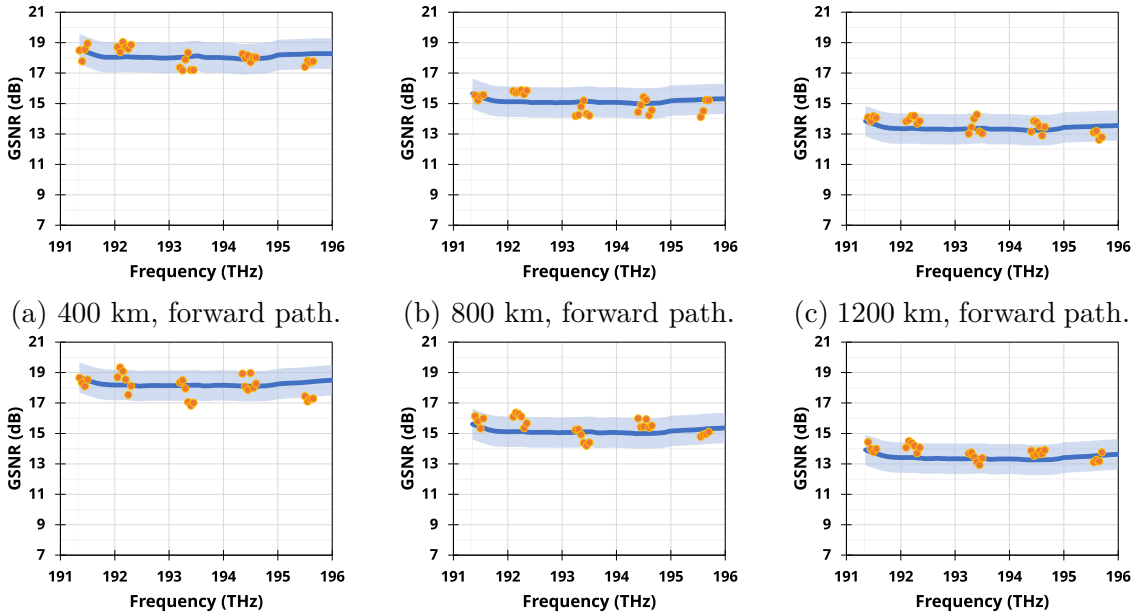

(a) 400 km, forward path. (b) 800 km, forward path. (c) 1200 km, forward path.

(d) 400 km, backward. (e) 800 km, backward. (f) 1200 km, backward.

Figure 3.15: Comparison of the estimation with the measurement for PM-16QAM.

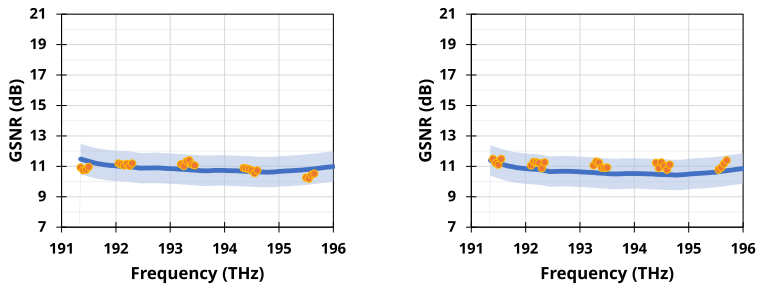

(a) 2000 km, forward path. (b) 2000 km, backward.

Figure 3.16: Comparison of the estimation with the measurement for PM-8QAM with Raman amplifiers turned off.

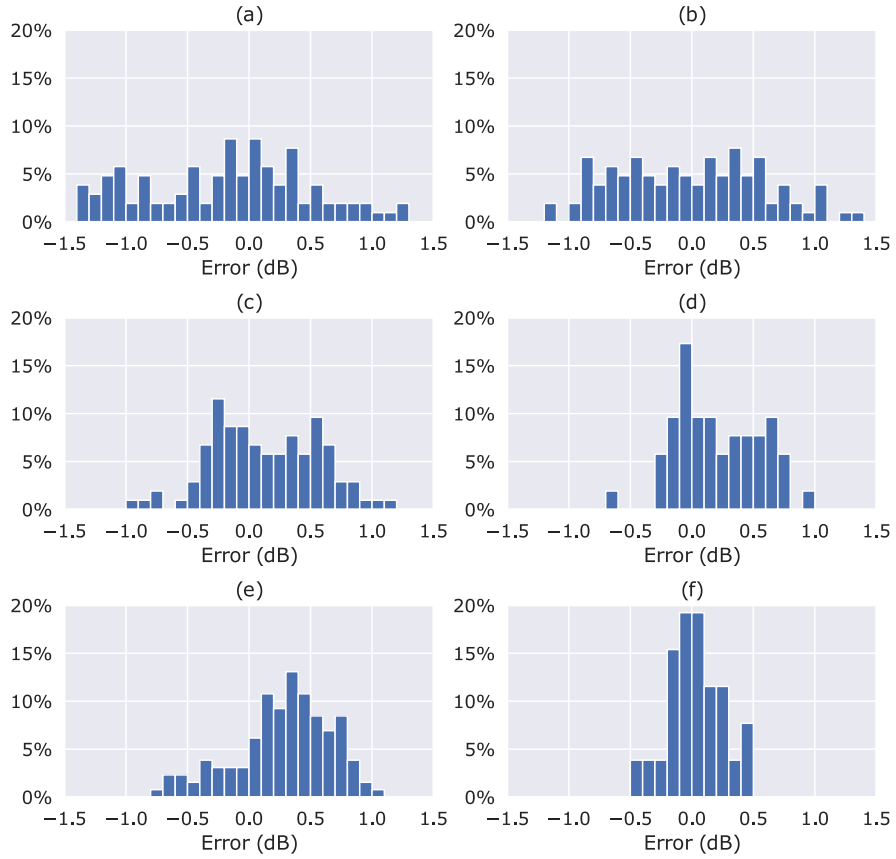

Figure 3.17: Error distribution grouped by distance: 400 km (a), 800 km (b), 1200 km (c), 1600 km (d), 2000 km (e) and 4000 km (f).

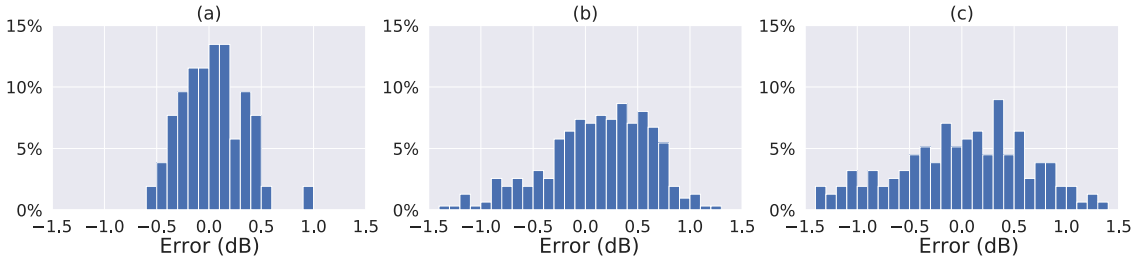

Figure 3.18: Error distribution grouped by modulation format: PM-QPSK (a), PM-8QAM (b) and PM-16QAM (c).

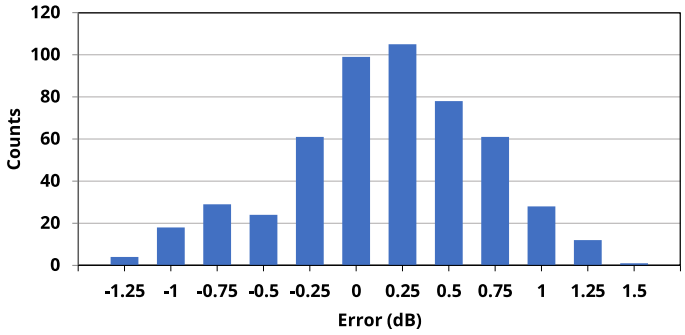

Figure 3.19: Error histogram over all measured points in the lab network.

mitigates the uncertainty on both ASE and NLI, because, for short distances it is more difficult to measure with high accuracy the GSNR since i) the BER is smaller, and then, less stable as, in the measurement time window, few errors are counted, ii) when the GSNR is higher, the estimated noise is smaller and thus, it is more sensitive to small inaccuracies. Moreover, as shown in Fig. 3.16, the GNPy estimations are accurate also without Raman cards demonstrating that GNPy is able to intercept the benefits of using different amplification techniques and thus it can be used as an engine of a what-if investigation in a total cost of ownership (TCO) analysis.

Finally, the errors have been computed as the difference between the measured GSNR and the estimated GSNR for all the signals and all the distances resulting in a set of 500 error samples. Figs. 3.17 report the error distribution grouped by distance. After 400 km ∼80% of the estimations are within ±1 dB. This percentage increases to ∼92% after 800 km and it arrives to the 100% for all the larger distances. The largest error is +1.4 dB and it is at 400 km. Finally, after 4000 km, all the errors are smaller than 0.5 dB. The average error is ∼+0.5 dB at 400 km and 800 km, then it goes to ∼+0.4 dB at 1200 km and, then ∼+0.3 dB after 1600 km and 2000 km. Finally, it shrinks down to ∼+0.2 dB at 4000 km.

Figs. 3.18 report the error distribution grouped by modulation format. The PM-QPSK modulation shows the smallest error statistic, whereas PM-16QAM shows the largest inaccuracy as the average error is ∼+0.2 dB for the PM-QPSK, ∼+0.4 dB for the PM-8QAM and ∼+0.5 dB for PM-16QAM. This because the PM-QPSK has been measured at the largest distances - were the accuracy is better - while PM-16QAM has been probed at the shortest reaches of 400 km, 800 km and 1200 km.

Fig. 3.19 groups all the errors together. The distribution is almost symmetric with a positive offset of ∼+0.25 dB and the average error is 0.1 dB. Moreover, 74% of the errors are positive and the largest error is 1.4 dB, meaning that most of the estimations are conservative.

In general, the error is determined by three main factors: (i) the conservative

assumptions of the GGN-model, (ii) the uncertainty in measuring the GSNR and (iii) the uncertainty of the parameters provided to GNPy to estimate the GSNR. In particular, factors (ii) and (iii) can lead to a non-conservative estimation of the overall performances even if the factor (i) would lead to conservative estimations. However, (i) justifies the conservative trend of the estimates.

In conclusion, GNPy shows conservative and accurate predictions of the GSNR being the average error equal to 0.1 dB and the error conservative in 74% of the cases.

3.3.3 Experimental Validation of the Microsoft production network

This section describes the GNPy validation over the Microsoft production network. It has to be remarked that, differently from the lab validation of the previous section, a validation over a production network is more challenging as in most of the cases the OSAs are not available, it is not possible to make use of the B2B of each transceiver unless it has been characterized before the deployment and thus it is necessary to use a more generic B2B that refers to the transceiver model. Moreover, the deployed networks suffer from non-ideal conditions such as aging of the components, sub-optimal connector cleanliness, and the presence of multiple splices along the fibers caused by continuous fiber cuts.

Network description

Table 3.4: Fiber parameters.

Fiber type	α (dB/km)	D (ps/nm/km)	γ (1/W/km)
NDSF	0.222	3.8	1.45
ELEAF	0.2	4	1.41
TWRS	0.24	6	1.84

The schematic representation of the network segment under analysis is depicted in Fig. 3.20. This portion of the network is a 3-node mixed-fiber mixed-amplifier network segment covering a distance exceeding 2000 km operated on the C-band and loaded with 40 channel on the 37.5 GHz WDM grid. The length of fiber spans ranges between 48 km and 115 km, and the involved fiber types are non-dispersion-shifted fiber (NDSF), enhanced large effective area fiber (ELEAF) and TrueWave RS (TWRS); whose parameters are reported in Tab. 3.4. Most of the amplification sites are hybrid Raman-EDFA, while a few of them are lumped-EDFA. In order to compensate for the amplifiers' ripple and the SRS, ROADM nodes are present every ∼600 km. Moreover, three add/drop locations – named node A, node B

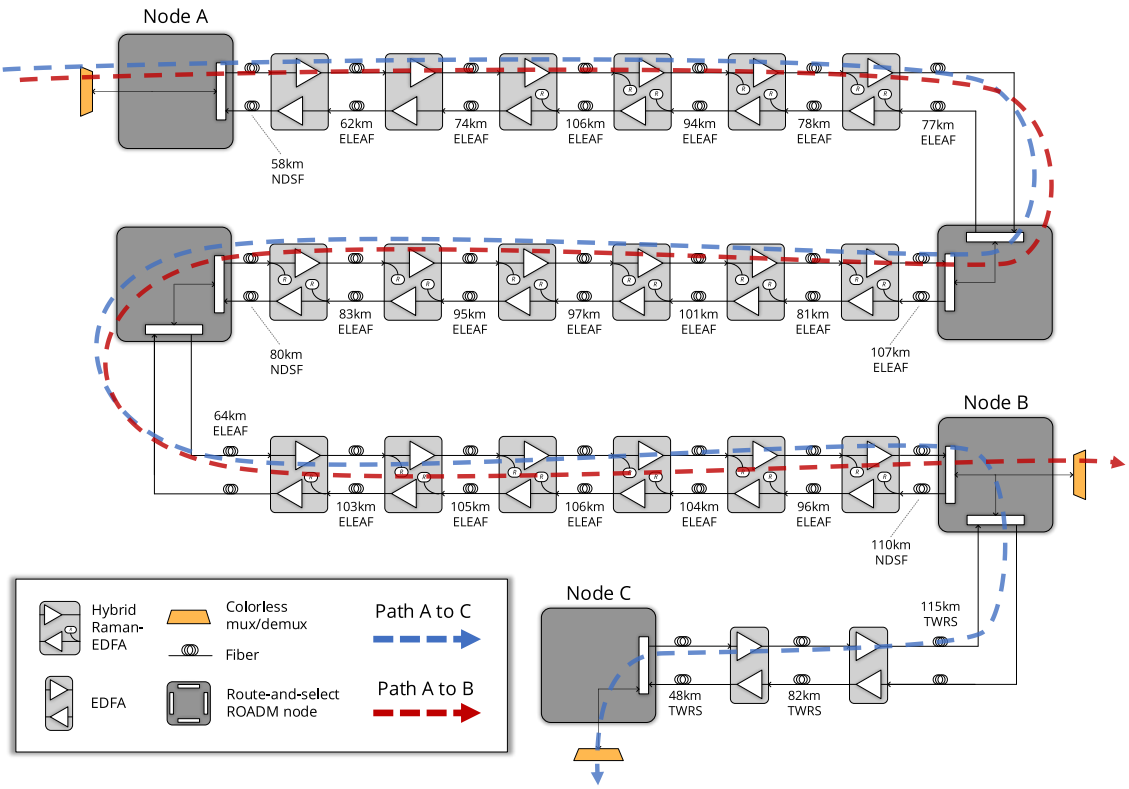

Figure 3.20: Layout of the analyzed network portion. Fiber types and lengths are described as well as amplifiers' type. Red and and blue dashed lines show the two analyzed paths.

and node C – are used to add/drop the channels. Elastic transceivers generate PM-8QAM modulated signals at the symbol-rate of 34.16 GBaud. The signals are RRC shaped having a roll-off factor of 0.2. The analysis will focus on two paths identified in Fig. 3.20 by dashed lines: from node A to node B (dashed red line) with a reach of ∼1900 km, and from A to C (dashed blue line) covering a distance of ∼2150 km. Ten LPs are provisioned in the spectral region between 191.35 THz and 191.6875 THz covering the path from node A to node B, and thirty LPs are provisioned in the spectral portion from 191.8125 THz to 193 THz, over the path A-to-C. The network equipment has been configured by a vendor proprietary line system controller to maximize the line system capacity.

Results

Fig. 3.21 reports the results and shows the exact spectral occupation of the channels. The figure compares the measured GSNR (triangular marks) with the GSNR estimated by GNPy (solid lines); the channels travelling along the path A-B are reported as green triangular markers and red solid line, while the channels

related to the path A-C are displayed with orange triangles and blue solid lines. Moreover, a ±1 dB band (light red and light blue) is also displayed. It can be observed that the estimations are always accurate and conservative in most of the cases. In detail, the estimation is always conservative on the path A-B, while, for the longest path A-C, some ripple can be observed in the curve of the GSNR because of the larger accumulation of the amplifiers' ripples. Few outliers can be observed at the edges of the spectrum.

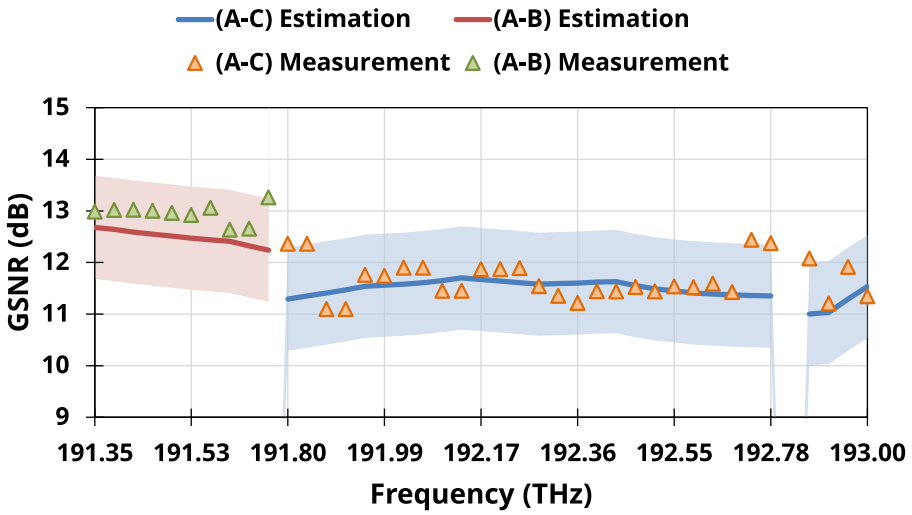

Figure 3.21: Measured (triangles) and estimated (solid lines) for the set of channels over the two analyzed paths. ± 1 dB confidence intervals are shown as colored background. The red line and the green triangles belong to the path A-B and the orange triangles and the blue line belong to the path A-C.

Fig. 3.22 depicts the histogram of the error computed as the difference between the estimated GSNR ($\mathrm{GSNR}_{\mathrm{est}}$) and the measured one ($\mathrm{GSNR}_{textmeas}$):

$$\mathrm{Error} = \mathrm{GSNR}_{\mathrm{est}} - \mathrm{GSNR}_{meas} \ . \tag{3.3}$$

All the errors are within the range between -0.3 dB and +1.2 dB, meaning that, the prediction can be fully trusted with a margin of only 0.3 dB. Moreover, only 23% of the cases are non-conservative. Furthermore, by observing Fig. 3.21, it can be noted that the non-conservative errors can be likely attributed to the ripple of the amplifiers that is not fully described in GNPy.

In conclusion, GNPy provided accurate while conservative estimations of GSNR over a major cloud provider's deployed network, where non-ideal conditions such as aging of the components, sub-optimal connector cleanliness, and the presence of multiple splices along the fiber path play a key role and have the potential to affect the predictions on the GSNR.

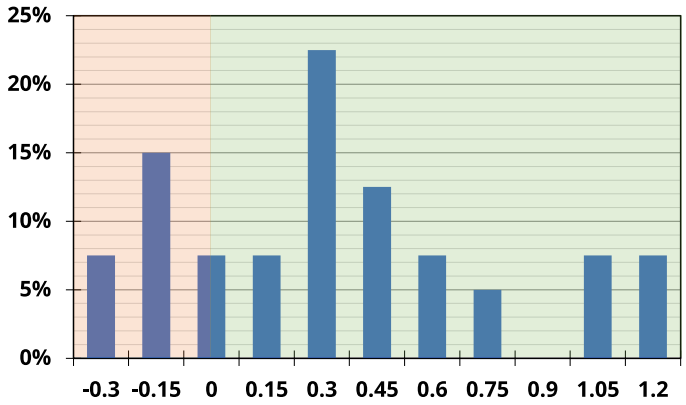

Figure 3.22: Error histogram over all measured points in the production network.

Chapter 4

Multi-band optimization and assessment

Ultra-wide band WDM systems have been proposed as a possible solution to increase the network capacity [115, 178] by extending the adopted optical bandwidth and, consequently, this technology has earned the attention of the industry [27, 68, 103]. Many experiments have been conducted by exploiting the C-, L- and S-bands [74, 148] or the L-, C-, S-, E- and O-bands [119]. Some effort has also been made to investigate what the most adequate amplification technology is, considering not only DFAs [8, 45, 106], but also Raman [8] amplification and SOAs [144, 145, 146]. Moreover, the power optimization is still an open issue [112].

This chapter is focused on point-to-point multi-band transmission systems. First, section 4.1 proposes an optimization strategy for multi-band transmission that generalizes the LOGO approach and finally, section 4.2 reports an assessment on the capacity of a point-to-point multi-band system for different applications and system configurations.

The material reported in this chapter was previously published in [58, 64].

4.1 C+L Power Optimization

This section proposes a generalization of the LOGO optimization paradigm [138] to optimize the transmitted power including the SRS effect. The section describes a C+L optimization strategy [64] that optimizes the average power per channel and the tilt of each optical band with the aim of maximizing the GSNR of the worst performing channel while equalizing the GSNR of all the other channels.

4.1.1 Methodology and Results

The system under analysis is depicted in Fig. 4.1. 161 32 GBaud PM-16QAM RRC channels are generated at the transmitter (TX) side; 83 C-band signals and

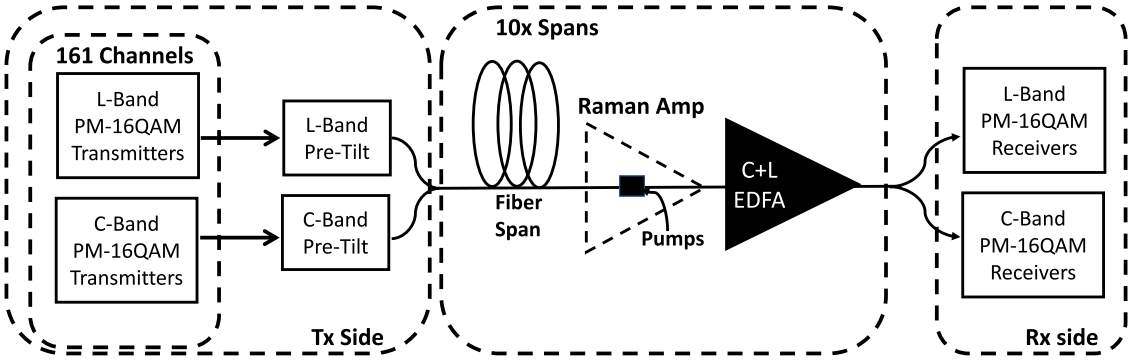

Figure 4.1: Layout of the system under analysis.

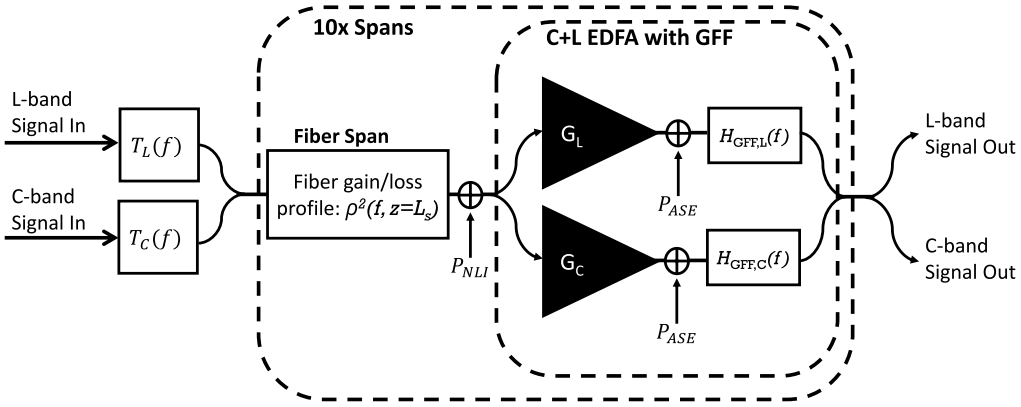

Figure 4.2: Equivalent block scheme of the optical system.

78 L-band signals operating on the 50 GHz DWDM grid, which are separated by a 250 GHz guard-band. The proper tilt is applied to the C- and L-bands then, the signals are multiplexed together and subsequently, the channels are transmitted over a 10-span link. Each span consist of an 80 km SSMF, followed by an HFA, which is composed of a Raman amplifier and a lumped C+L EDFA; the Raman amplifier injects into the fiber 5 counter-propagating Raman pumps with the parameters are reported in table 4.1 and the EDFA includes a gain-flattening filter (GFF), which restores the power profile at the input of the next fiber. At the end of the link, each optical channel is demodulated by a receiver that uses an LMS adaptive equalizer.

The equivalent scheme of the system is depicted in Fig. 4.2. The multiplexer applies the tilts $T_L(f)$ and $T_C(f)$ to the L-band and C-band channels, respectively. Then the resulting comb is amplified/attenuated by the fiber gain/loss profile $\rho^2(f, z = L_s)$, where $\rho^2(f, z = L_s)$ takes into account the frequency dependent fiber loss and the SRS. Then, the NLI disturbance has been computed according to the GGN-model and added to the signal. Then the two bands are de-multiplexed and amplified independently. The L- and C-band lumped amplifiers amplify the band by a quantity G_L and G_C, respectively. Moreover, the ASE noise is added to

Table 4.1: Parameters of the Raman amplifier's pumps.

	Pump 1	**Pump 2**	**Pump 3**	**Pump 4**	**Pump 5**
Power	150 mW	250 mW	150 mW	250 mW	200 mW
Frequency	200 THz	202 THz	207 THz	209 THz	210 THz

the signal assuming a noise figure of 1.6 dB and the transfer function of the GFF ($H_{GFF}(f)$) compensates for all the ripples, such that

$$\rho^2(f, z = L_s) \times G \times H_{GFF}(f) = 1 \tag{4.1}$$

over each band. In this way, the system is strictly periodical, the spectrum at the input of each fiber has always the same shape and each span results to be independent of the others.

The average transmitted power per channel has been computed according to the LOGO algorithm and then, the C- and L-band tilts $T_C(f)$ and $T_L(f)$ were applied. The optimization strategy proposed here is based on a brute force approach by compensating a percentage of the inter-channel SRS tilt between 0% and 100%. The resulting power per channel of all the explored combinations are reported in Fig. 4.3a. The GSNR of each tilt configuration has been evaluated (Fig. 4.3b) and the configuration maximizing the GSNR of the worst performing channel while flattening the spectrum has been selected. This approach aims to guarantee a mimimum level of performance for all the channels, however the strategy is totally compatible with any optimization approach, such as the maximization of the total link capacity.

In order to compare different launch strategies, other than this optimum configuration, also three other strategies are assessed: a no tilt strategy transmitting a flat power spectral density, a tilt aiming at pre-compensating 100% of the tilt and a tilt pre-compensating the 50% of the fiber tilt.

Because of the large computational time required by the SSFM, it was not possible to use it for the optimization process, therefore the GGN-model has been adopted. However, the SSFM simulations [30, 130] have been run on each of the four investigated configurations in order to validate the results obtained with the GGN-model.

10 channels under test are considered: 5 in the L-band at the frequencies 187.9 THz, 188.8 THz, 189.65 THz, 190.5 THz, 191.3 THz and 5 in the C-band at the frequencies 192.1 THz, 193.0 THz, 193.9 THz, 194.8 THz and 195.7 THz. Moreover, the signals are extracted after 5 and 10 fiber spans.

The brute force shows that the tilt configuration results to be optimum when the C-band does not compensate for the inter-channel SRS ($T_C(f) = 0$), while the L-band tilt compensates 50% of the inter-channel SRS. The optimum solution and the the reference no-tilt solution ($T_C(f) = 0$ and $T_L(f) = 0$) have also been

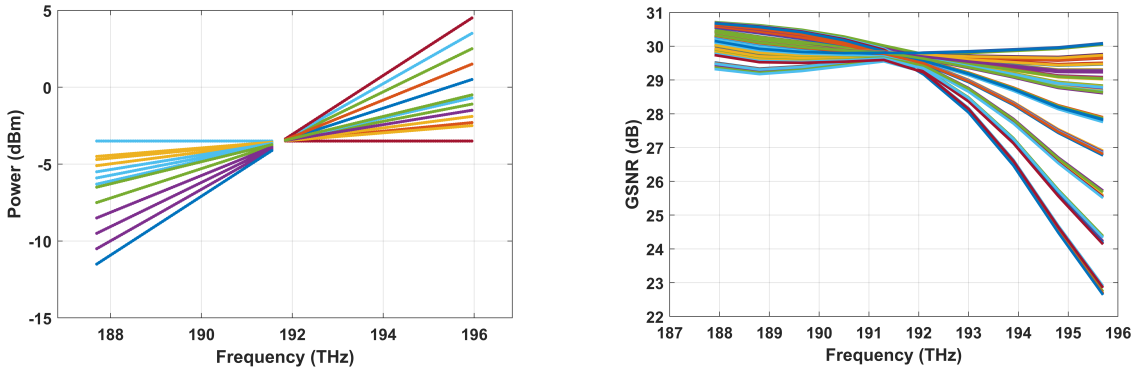

(a) (b)

Figure 4.3: Brute force tilt strategies of the transmitted power per channel (a) and the corresponding GSNR curves after one span (b).

simulated using the SSFM in order to validate the results obtained with the GGN-model. Also, the case in which 100% of the inter-channel SRS is pre-compensated and the case in which 50% of inter-channel SRS is pre-compensated have been SSFM simulated.

Figs. 4.4 report the results as GSNR vs. frequency after 5 (blue lines) and 10 (orange lines) spans. The dashed curves report the results of the SSFM simulations and the GGN-model estimations are reported as solid lines. The figures refer to different pre-emphasis strategies: a flat power per channel (Fig. 4.4a); a pre-compensation of 100% of the fiber tilt, such that the received power per channel is flat (Fig. 4.4b); a pre-compensation of 50% of the tilt introduced by the fiber propagation (Fig. 4.4c); and the optimum pre-emphasis provided by the brute force strategy (Fig. 4.4d). In general the GGN-model presents an excellent agreement with the split-step simulations demonstrating that the GGN-model is able to predict with good accuracy the values of the GSNR and the frequency dependent variation. Moreover, the gap between the split-step after 5 spans and after 10 spans is exactly 3 dB, confirming the incoherent accumulation of the NLI in which the GGN-model is based. Comparing the different pre-emphasis, transmission without tilt pre-emphasis (Fig. 4.4a) leads to largely sub-optimal performances, mainly in the L-band and, while the pre-emphasis compensate for all the fiber tilt (Fig. 4.4b) the L-band GSNR increases but the C-band GSNR decreases significantly leading to a GSNR unbalance of $\sim$2 dB. Moreover, a trade off between these two solutions has been investigated by compensating half of the fiber tilt (Fig. 4.4c) and, in this case, the performances are better than the previous cases but the C-band GSNR is still bad-performing. Finally, in case the pre-emphasis of the brute force solution is applied (Fig. 4.4d), the GSNR is maximized for most of the channels and it also presents a good balance between the C- and L-band as the GSNR curve is almost flat.

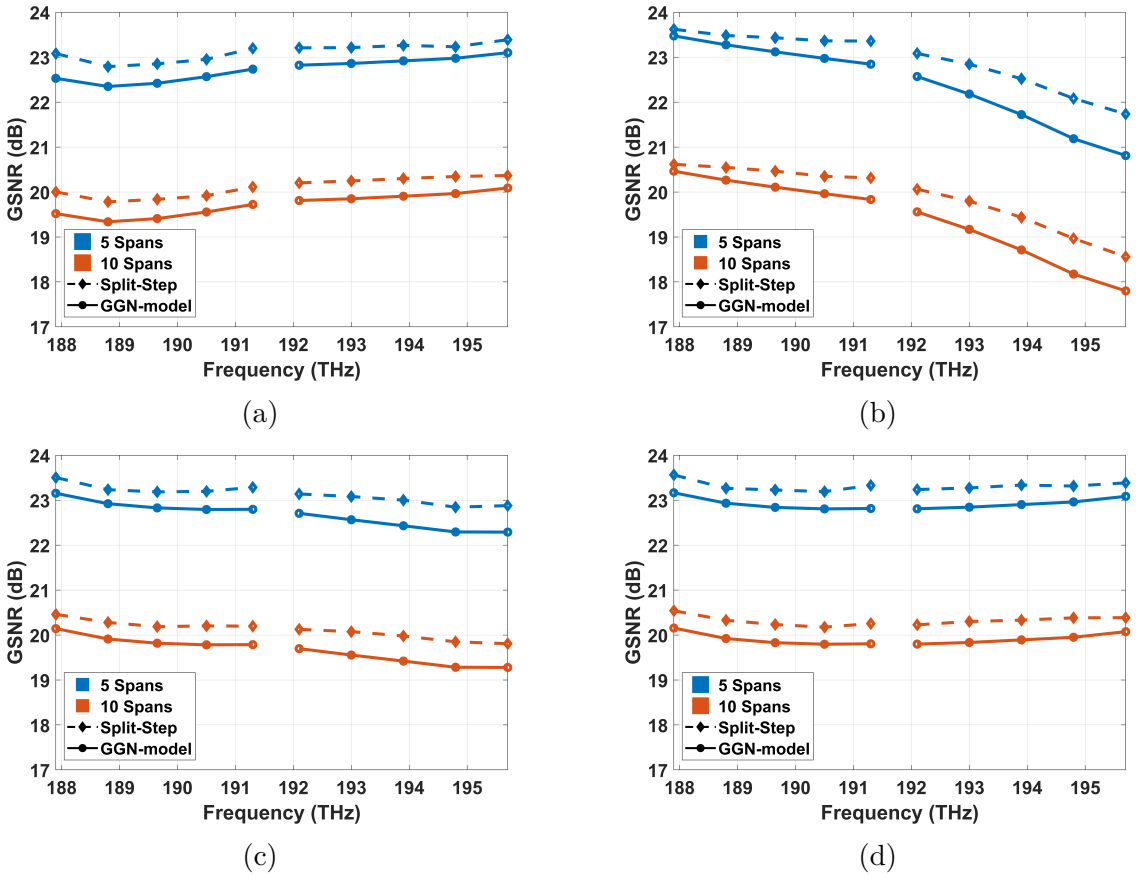

Figure 4.4: The GSNR after 5 and 10 spans computed both by means of the SSFM and the GGN-model without pre-compensating the fiber tilt (a), pre-compensating 100% of the tilt (b), pre-emphasis 50% of the tilt (c) and with the optimum tilt pre-compensation (d).

In conclusion, it has been shown that approaching a multi-band system with a unique power tilt leads to sub-optimal performances, while considering a per-band tilt is beneficial with practical no costs since the C+L lumped amplifier is made of a C-band EDFA combined with an L-band EDFA, and each of them can be configured with a different tilt. A separate management of the channel power on a per-band basis can give significant benefits. Therefore, the GGN-model can be exploited to maximize while equalizing the GSNR of a C+L optical system as the reliability of the results has been validated by means of SSFM simulations.

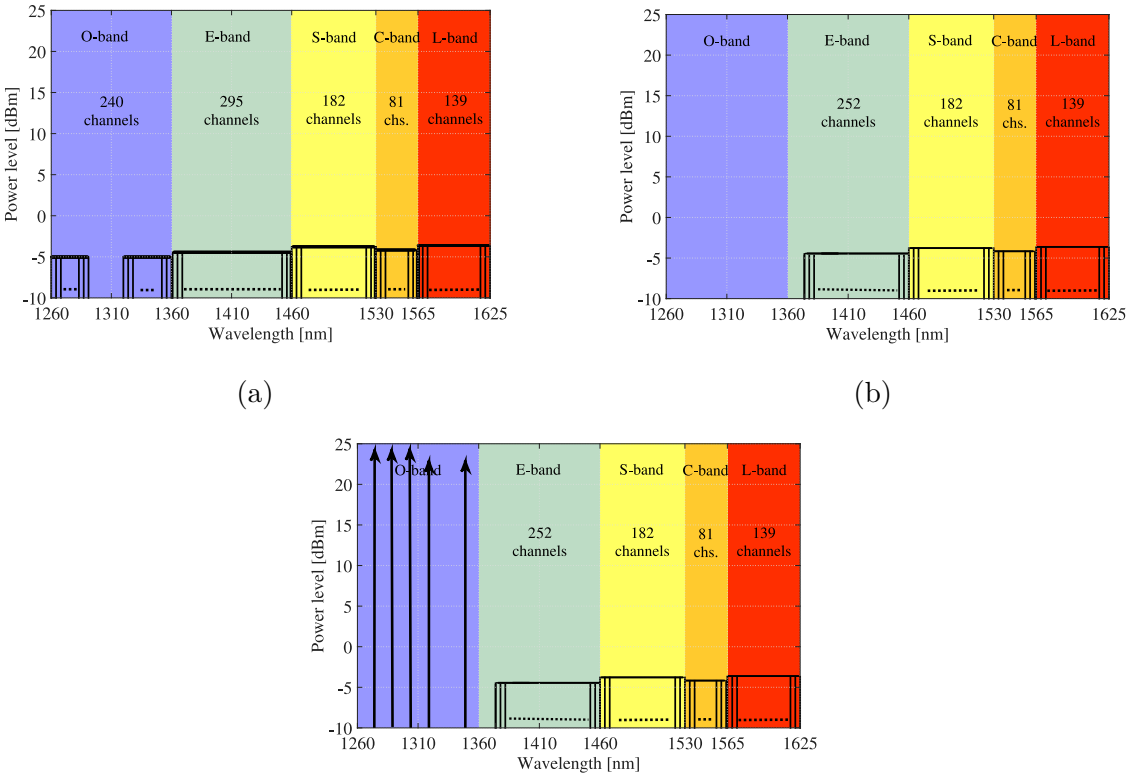

Figure 4.5: Considered system configurations: (a) Full multi-band transmission; (b) O-band off; (c) O-band off, Raman in O-band, E → L-band.

4.2 Multi-band point-to-point analysis

This section reports a performance assessment on a multi-band point-to-point system which makes use of the O-, E-, S-, C- and L-bands (Table B.3). Then, three different multi-band configurations are tested as reported in Figs. 4.5: an O → L-band configuration using all the bands to transmit WDM channels (Fig. 4.5a); an E → L-band configuration using all the bands except from the O-band (Fig. 4.5b); and an E → L-band configuration using the O-band for Raman amplification (Fig. 4.5c). Furthermore, this investigation explores different applications and therefore different reaches: data center interconnect (DCI) (single span link), metro (150 km), extended metro (300 km) and regional (600 km). Moreover, also different span lengths (L_s) are assessed: 50 km and 75 km.

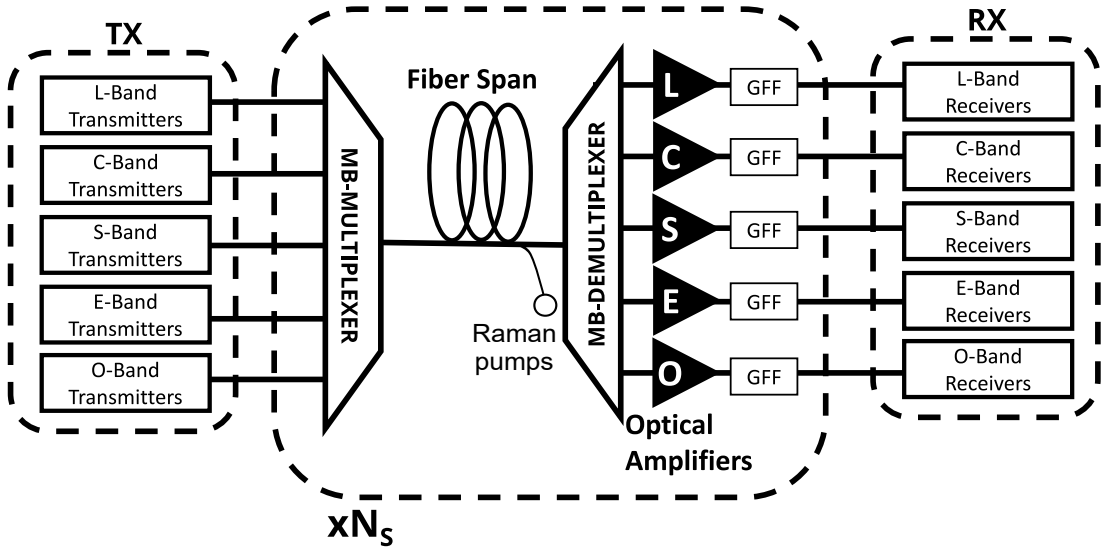

Figure 4.6: Layout of the multi-band system under analysis.

Methodology

The system under analysis is depicted in Fig. 4.6; the transmitters generate the signals that are then multiplexed together by a multi-band (MB) multiplexer. The combined signals are transmitted together through a periodic point-to-point multi-span optical link made of N_s spans having length L_s. The fiber attenuation, dispersion and the non-linear coefficient are summarized in Fig. B.5 and in Table B.3. For the scenarios including Raman amplification, at the end of each fiber span, counter-propagating Raman pumps are injected and the parameters of the Raman pumps are reported in Table 4.2. Then, in each amplification site, the signals are de-multiplexed and amplified by the corresponding optical DFA whose parameters are reported in Table B.3. After each amplifier, a GFF recovers the ripples of the channels introduced by the propagation. Finally, at the end of the link, the signals are de-multiplexed, amplified for the last time and received. The signals are RRC shaped with a roll-off of factor of 15% and a symbol-rate (R_s) of 32 GBaud. The channels occupy the 50 GHz fixed-grid. The detailed spectral occupation and the number of WDM slots per band are reported in Table B.3. A 2 nm guard-band among the adjacent bands has been assumed as well as a non-transmission bandwidth of 5 THz (30 nm) around the zero-dispersion frequency of the fiber, as shown in [71]. Therefore, the total bandwidth is 53 THz. The spectrum is assumed to be fully loaded and the controller configures the optical system to operate using the LOGO [138] on a per-band basis.

Each span of the link is abstracted as depicted in Fig. 4.7, where each band is multiplexed through a MB multiplexer to obtain the multi-band signal at the input

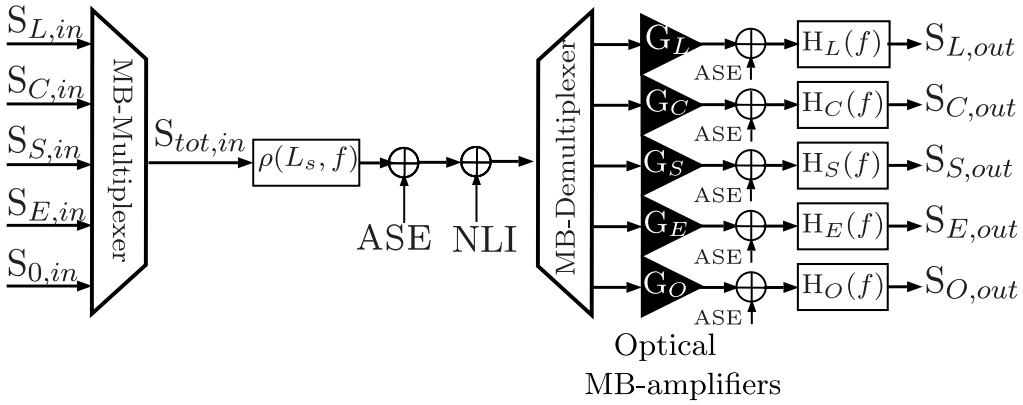

Figure 4.7: Equivalent block diagram of a span.

Table 4.2: O-band Raman pump configuration.

Frequency [THz]	222.22	227.27	229.89	232.56	235.29
Power [mW]	200	200	350	350	350

of the fiber ($S_{tot,in}$). The fiber is abstracted with an equivalent filter ($\rho(L_s, f)$) - evaluated as described in Appendix A - plus the ASE noise introduced by the Raman amplifier and the NLI generated by the fiber whose power is computed by means of the GGN-model as shown in Sec. 2.1.3. After the MB de-multiplexer, each amplifier is abstracted with a flat gain G, an additive Gaussian ASE noise and a filter ($H(f)$) modelling the GFF.

In the presence of Raman pumps, also the four-wave mixing (FWM) and the consequent GSNR penalty has been assessed according to [15], assuming a back-scattering coefficient (κ) equal to $10^{-7}\frac{1}{m}$. Therefore, a 2 THz extra guard-band has been adopted to keep the pump-pump FWM always negligible. For this reason, when the O-band is used by the Raman amplifier, the number of channels in the E-band is reduced from 295 to 252.

For each scenario under analysis, the GSNR has been computed. Subsequently, the capacity of each channel (R_b) is computed as:

$$R_b = R_s \, \mathrm{SE} \, , \tag{4.2}$$

SE is the spectral efficiency computed as:

$$\mathrm{SE} = \frac{2 \log_2(1 + \mathrm{GSNR})}{1 + \mathrm{OH}} \tag{4.3}$$

where OH is the FEC overhead assumed equal to 12%.

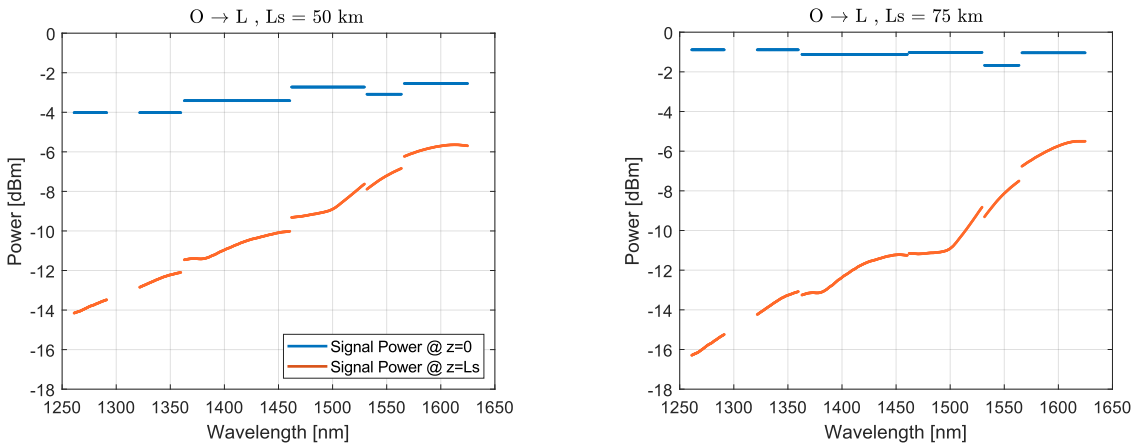

(a) (b)

Figure 4.8: Signal power at the beginning of the fiber ($z = 0$) in blue and at the end ($z = L_S$) in red, for L_S =50 km (a) and L_S =75 km (b).

Results and Comments

Figs. 4.8 report the power of the signals at the beginning (blue) and at the end (red) of a fiber span having length 50 km (Fig. 4.8a) and 75 km (Fig. 4.8b) in case all the bands are used for channel transmission. As expected, the low-wavelength signals present a larger power loss due to the higher fiber attenuation and the SRS that transfers power from the low-wavelength channels to the high-wavelength ones. On the contrary, high-wavelength signals experience a very small loss because of SRS and because the attenuation is lower. Therefore, the channels present a tilt over the entire bandwidth of 8 dB after 50 km and of 10 dB after 75 km.

Fig. 4.9 reports the GSNR (solid blue line), the $\mathrm{SNR_{ASE}}$ (dashed green line) and the $\mathrm{SNR_{NL}}$ (dash-dotted red line) after the propagation along one span of 75 km in case the channels are transmitted in all the bands. Most of the channels present a large imbalance between $\mathrm{SNR_{ASE}}$ and the $\mathrm{SNR_{NL}}$. This is due to the power tilt observed in Fig. 4.8b. Hence, the power of the low-wavelength channels will be very small at the end of the fiber and then, the performances will be mainly affected by the ASE noise introduced by the amplifiers. On the other side, the high-wavelength channels receive a power gain which causes an enhancement of the NLI generation and, therefore, these channels experience a lower $\mathrm{SNR_{NL}}$. For this reason, the use of a power pre-emphasis and Raman amplification can be investigated to mitigate the effect of SRS, as shown in [77, 114]. Moreover, the L-band presents a slight upturn owing to the absence of channels at higher wavelength that reduces the overall amount of NLI generated in that portion of the spectrum. The discontinuities among the transmission bands are due to the discontinuity both in the transmitted power and in the amplifiers' NF.

Table 4.3: Spectral efficiency of each scenario [bps/Hz].

		O → L					No Raman, E → L				Raman in O, E → L			
		O	E	S	C	L	E	S	C	L	E	S	C	L
$L_s = 50$ km	DCI	8.7	10.0	10.0	9.9	9.4	10.0	10.3	9.9	9.6	11.2	11.1	10.8	10.6
	Metro	6.9	8.2	8.3	8.1	7.7	8.2	8.5	8.1	7.8	9.4	9.3	9.0	8.8
	Extended Metro	5.8	7.1	7.1	7.0	6.6	7.1	7.4	7.0	6.7	8.3	8.2	7.9	7.7
	Regional Network	4.7	6.0	6.0	5.9	5.5	6.0	6.3	5.9	5.6	7.2	7.1	6.8	6.6
$L_s = 75$ km	DCI	6.8	8.5	8.7	8.5	7.8	8.5	9.0	8.5	7.9	9.3	9.3	8.9	8.7
	Metro	5.7	7.4	7.6	7.4	6.7	7.4	7.9	7.4	6.8	8.2	8.1	7.8	7.6
	Extended Metro	4.6	6.3	6.5	6.3	5.6	6.3	6.7	6.3	5.7	7.1	7.0	6.7	6.5
	Regional Network	3.6	5.2	5.4	5.2	4.5	5.2	5.6	5.2	4.6	6.0	5.9	5.6	5.4

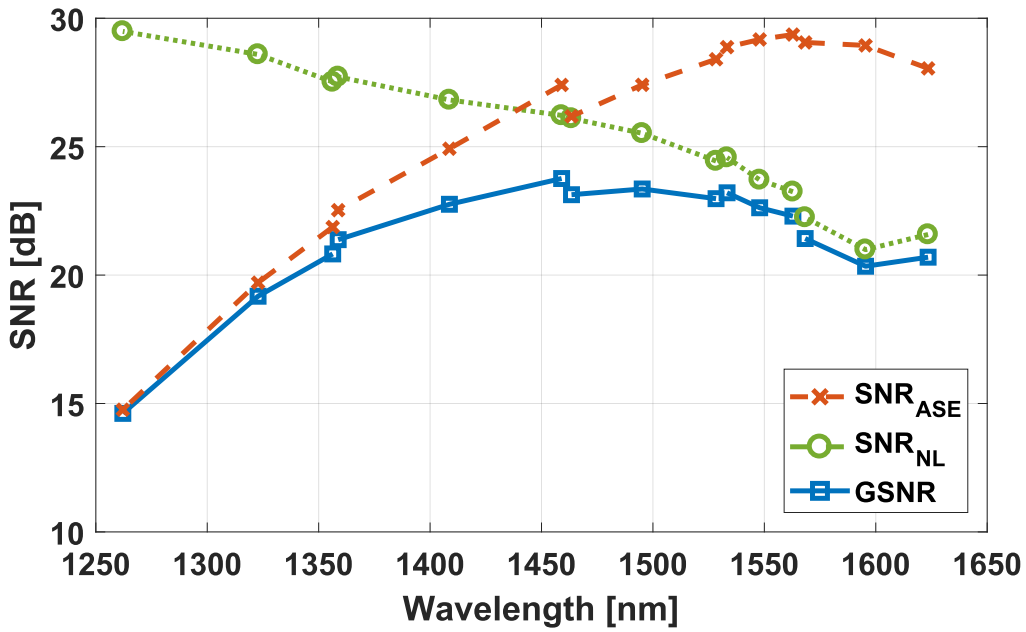

Figure 4.9: Single span GSNR, $\mathrm{SNR_{ASE}}$ and $\mathrm{SNR_{NL}}$ in case all bands are used for channel transmission with $L_s = 75$ km.

Table 4.3 reports the average spectral efficiency of each band and Fig. 4.10 reports the bit-rate for each scenario, including different span lengths (50 km and 75 km), spectral configurations (O→L and E→L with and without Raman pumps) and distances (single span, 150 km, 300 km and 600 km). Results demonstrate that the best performing bands are the ones in the middle of the spectrum since the inter-channel SRS depletion almost compensates the inter-channel SRS pump and since the fiber attenuation is the smaller. As expected, the scenarios where the span length is 75 km are less performing because of the larger fiber attenuation. The O-band has poor performances because the fiber attenuation is high, as well as the SRS power depletion and the O-band NF is larger compared the one of the others. Furthermore, even if the fiber dispersion is very low in the O-band, this does not significantly impact the propagation performance, as the O-band is limited by the ASE noise, as shown in Fig. 4.9. Moreover, comparing the E→L with and without Raman amplification, it can be observed that the use of O-band Raman amplification leads to limited improvements as the bit-rate increases by only 10%. This is due to the large fiber attenuation limiting the effectiveness of the Raman amplification.

Figs. 4.11 and Table 4.4 report respectively the capacity per band and the the total capacity for all the considered scenarios. By comparing the capacity in the O-band to the one in the S-band, it can be noted that, despite the large difference in terms of channels used -240 versus 182-, they carry a similar quantity of traffic and this is due to the poorer GSNR of the O-band channels. Moreover, in the DCI

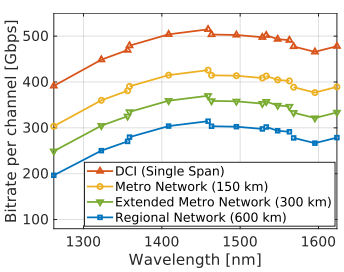

(a) Full O → L, L_s = 50 km.

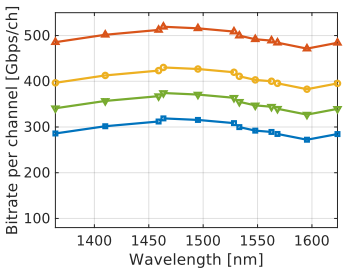

(b) No Raman, E → L, L_s = 50 km.

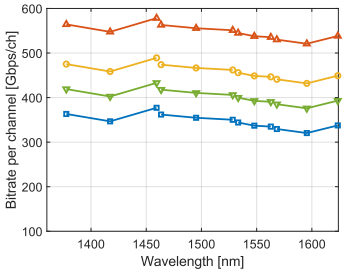

(c) Raman in O, E → L, L_s = 50 km.

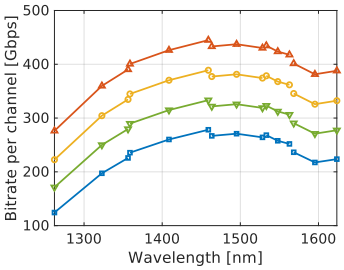

(d) Full O → L, L_s = 75 km.

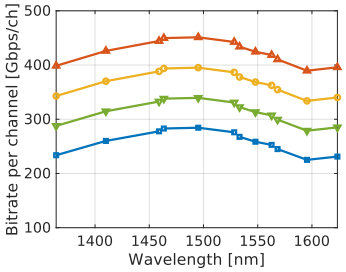

(e) No Raman, E → L, L_s = 75 km.

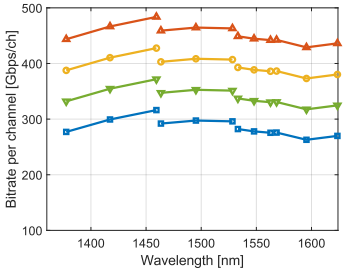

(f) Raman in O, E → L, L_s = 75 km.

Figure 4.10: Net bit-rate per wavelength for each scenario when considering two different span lengths. Each row reports different span lengths – $L_s = 50$ km the first and $L_s = 75$ km the second one. Each column refers to different bandwidth uses: full O→L the first, E→L without Raman amplification the second and E→L with Raman amplification the last one.

Table 4.4: Maximum capacity [Tb/s].

		O → L	No Raman E → L	Raman in O E → L
$L_s = 50$ km	DCI	450	348	359
	Metro	367	268	302
	Extended Metro	314	229	265
	Regional	263	208	229
$L_s = 75$ km	DCI	375	296	298
	Metro	323	258	261
	Extended Metro	272	219	225
	Regional	222	181	189

scenario the total capacity increases by ∼15% (from 450 Tbps to 375 Tbps) when the span length reduces from 75 km to 50 km. Then, in the other scenarios, this gap reduces enlarging the total distance. Moreover, the use of the O-band in a DCI scenario, increases the total capacity by 20% and 30% when the distance is 50 km

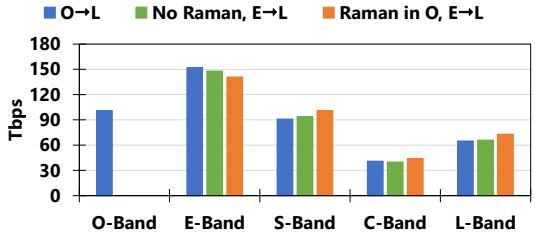

(a) DCI (Single Span), $L_s = 50$ km.

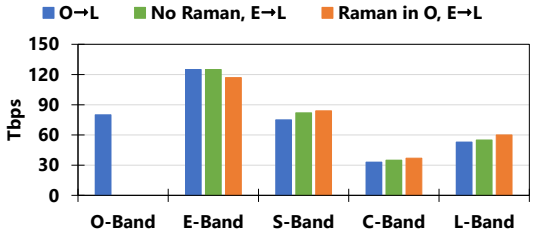

(b) DCI (Single Span), $L_s = 75$ km.

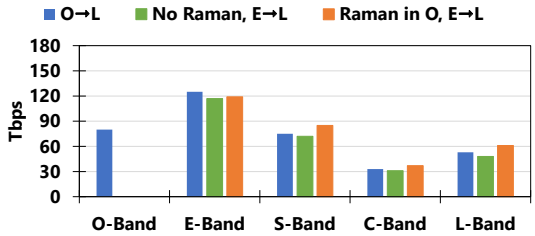

(c) Metro (150 km), $L_s = 50$ km.

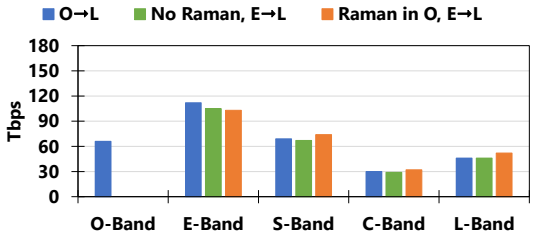

(d) Metro (150 km), $L_s = 75$ km.

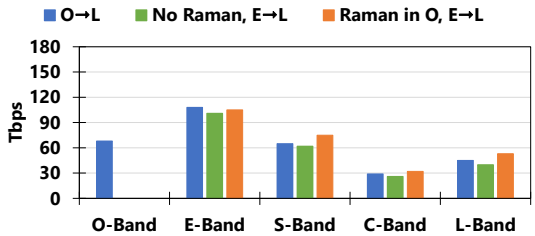

(e) Extended Metro (300 km), $L_s = 50$ km.

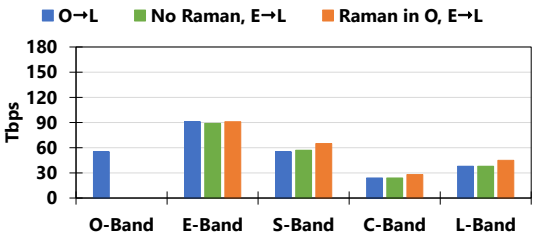

(f) Extended Metro (300 km), $L_s = 75$ km.

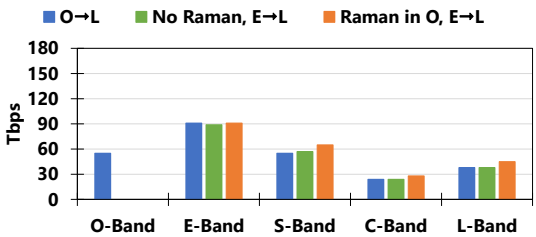

(g) Regional (600 km), $L_s = 50$ km.

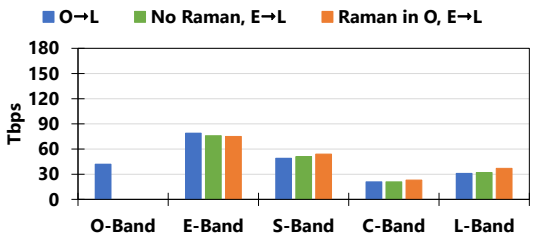

(h) Regional (600 km), $L_s = 75$ km.

Figure 4.11: Maximum capacity per transmission band. Each row refers to a different reach: DCI (75 km) the first, metro (150 km) the second, extended metro (300 km) the third and regional (600 km) the last one. Left-hand side: 50 km spans; and right-hand side: 75 km spans.

and 75 km at the cost of deploying a larger number of transceivers.

Finally, Table 4.5 reports the capacity increase of the analyzed scenarios with

Table 4.5: Gain factor with respect to full C-band and full C+L.

		Gain from C-band			Gain from C+L-band		
		O → L	No Raman E → L	Raman in O E → L	O → L	No Raman E → L	Raman in O E → L
$L_s = 50$ km	DCI	10×	8×	8×	4×	3×	3×
	Metro	10×	7×	8×	4×	3×	7×
	Extended Metro	9.5×	7×	8×	4×	3×	3×
	Regional	9×	7×	8×	4×	3×	3×
$L_s = 75$ km	DCI	9×	7×	7×	4×	3×	3×
	Metro	9×	7×	7×	3×	2.7×	3×
	Extended Metro	9×	7×	7×	3×	3×	3×
	Regional	8×	7×	7×	3×	3×	3×

respect to a full C-band system and a full C+L system with the same system parameters. As expected, the capacity gain is smaller that the bandwidth enlargement. This is due to the decrease in the GSNR while increasing the number of transmitted channels. Moreover, the capacity gain always decreases with the increase of the fiber length and the increase of the total distance, however, the use of all the bands leads to a capacity that is between 8 and 10 times larger than a full C-band system and between 2.3 and 3 times larger than a C+L system.

In conclusion, the already exploited C-band is a small portion of the entire available band as the vast majority of the modern fibers deployed do not present the OH water-peak and, therefore, the attenuation is always smaller than 0.4 dB/km. Consequently, in absence of available dark fibers, once the technology becomes available, multi-band transmission might represent an alternative option to the deployment of other fibers to enhance the capacity of an optical network. The fiber capacity can be, indeed, extended up to 9-10 times width respect to a C-band system. However, how much of the portion of the available spectrum is convenient to exploit as well as the maximum acceptable span length and the convenience in using Raman amplification are issues that has to be investigated in a TCO analysis by trading off costs and performances.

Chapter 5

Physical layer aware optical networking assessments

Many research activities have been focused on optical network design and planning targeting capacity, cost and energy optimizations [87, 124, 125, 173, 180, 182], as well as taking into account the regenerator placement problem [72, 183]. However, the analyses carried out are usually specific for a given problem. This allows high performance to be achieved for the given problem however, on the other hand, the results lack generality and, in this way, they do not permit a general comparison of the networking benefits of different physical layer technologies. On the contrary, the network analysis tools introduced and adopted in this chapter assess average performances by observing both offline and average metrics.

This chapter introduces two network analysis and design tools: the OPLA tool [65] and the SNAP tool [22, 37]. OPLA is an offline tool based on the observation of the routing space statistics of a given network, while SNAP is a Monte Carlo based tool simulating the progressive load of an optical network. The tools are then used to analyze and compare the network benefit of many physical layer technologies, such as Raman amplification [18], advanced DSP techniques [40, 46], SDM [50, 179] and ultra-wideband transmission [115].

This chapter is structured as follows: section 5.1 describes OPLA showing a possible application on the selection of amplifier upgrades (section 5.1.1) and on the removal of OEO regenerators to reduce the network costs (section 5.1.2); section 5.2 reviews the SNAP structure firstly introduced in [22, 37] and then, it reports some technological comparisons by first, comparing different SDM technologies (section 5.2.2) and then, SDM with multi-band transmission (section 5.2.3).

The material reported in this chapter was previously published in [53, 55, 62, 63, 65].

5.1 Offline Physical Layer Assessment

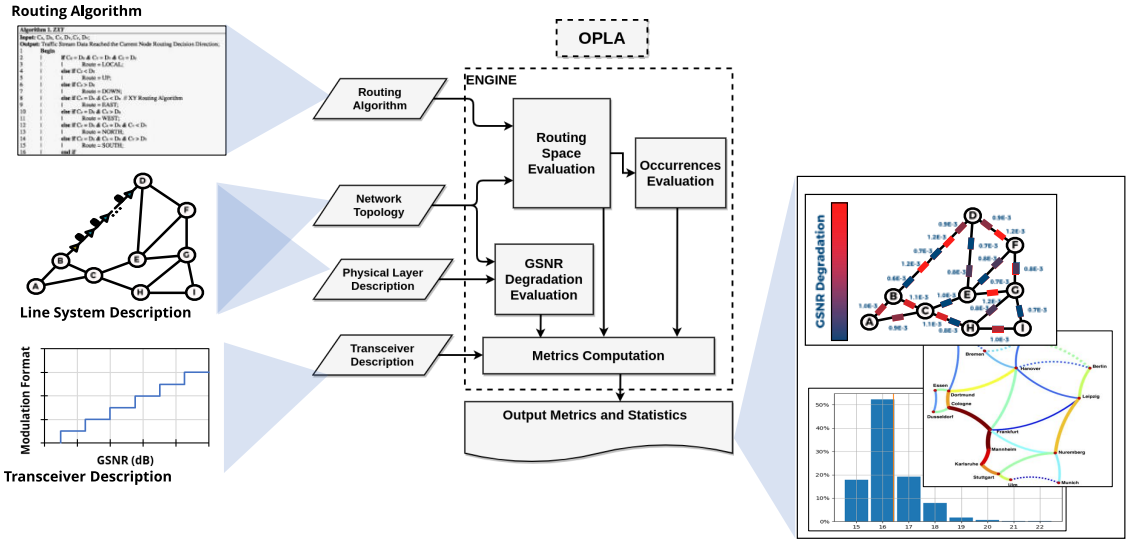

Figure 5.1: The structure of OPLA.

OPLA is a network tool for analyzing and optimizing the physical layer of the optical networks whose code structure is reported in Fig. 5.1. Since OPLA is an offline tool, it does not simulate the actual allocation of the LPs making faster each network assessment.

As input, OPLA requires the selection on the routing algorithm to be used, the description of the network physical layer and the transceiver characteristic including the GSNR threshold of each operating mode and the relative parameters.

First, given the selected routing algorithm and the network topology, OPLA evaluates the routing space of the network under analysis, i.e., the set of paths that are explored to accommodate a LP. Subsequently, two main weighted graphs are created: a noise-to-signal ratio (NSR) graph and an occurrences graph.

The NSR graph abstracts each NE composing the network with its NSR defined as

$$\mathrm{NSR}_{\mathrm{NE}} = \frac{P_{\mathrm{noise}}}{P_{\mathrm{s}}} \tag{5.1}$$

where P_{noise} is the noise introduced by the NE, including ASE noise and NLI under the conservative assumption of full-spectral load. Then, P_s is the signal power. It can be noted that this graph can be used to identify the most critical NE in terms of signal degradation that they introduce as they present the largest NSR.

Similarly, the occurrence graph evaluates a metric for each NE that is the number of occurrences of each NE (O_{NE}) in the routing space, i.e., the number of paths traversing the network element. This graph gives information on how often a NE

appears in the routing space and, consequently, which NE will probably be used by more LPs.

Based on that, OPLA computes aggregated metrics on the entire routing space or a subset of the paths that satisfy some condition such as having a specific source and/or destination node or traversing some specific NE, link and/or node. Moreover, OPLA makes use of the NSR graph to compute the GSNR of each path ($\mathrm{GSNR}_{\mathrm{path}}$) as

$$\mathrm{GSNR}_{\mathrm{path}} = \frac{1}{\sum_{i \in \mathrm{path}} \mathrm{NSR}_{\mathrm{NE},i}} \,, \tag{5.2}$$

hence, $\mathrm{GSNR}_{\mathrm{path}}$ is evaluated by accumulating the NSR contribution of all the NEs belonging to the path. Then, given the transceiver description, OPLA evaluates the feasibility of each operating mode and, consequently, the one maximizing the capacity of the path. Besides, OPLA utilizes the occurrences graph to evaluate metrics such as the maximum occurrences ($\mathrm{O}_{\mathrm{max,p}}$) and the average occurrences ($\mathrm{O}_{\mathrm{avg,p}}$) of each path as

$$\mathrm{O}_{\mathrm{max,p}} = \max_{\{i \in \mathrm{path}\}} \{\mathrm{O}_{\mathrm{NE},i}\} \tag{5.3}$$

and

$$\mathrm{O}_{\mathrm{avg,p}} = \frac{1}{\mathrm{N}_{\mathrm{NE}}} \sum_{i \in \mathrm{path}} \mathrm{O}_{\mathrm{NE},i} \tag{5.4}$$

where $\mathrm{O}_{\mathrm{NE},i}$ is the occurrence of the i-th NE and N_{NE} is the number of NEs belonging to the path. Such metrics give an indication of how likely the path will be congested.

In general, OPLA enables an offline analysis and optimization of the network, of the routing algorithms and of the transceivers. Moreover, it is noteworthy that this approach has an added value in decoupling the network performances with respect to the transponder characteristics and this is in perfect synergy with an open and disaggregated paradigm, where the network and the transponders are disaggregated [91].

The remainder of this section reports an example of the application of OPLA to address the amplifier upgrades (subsection 5.1.1) and to reduce the number of OEO regenerators in a translucent network by deploying Raman amplifiers and upgrading the transceivers (subsection 5.1.2).

5.1.1 Selection of Amplifier Upgrades Addressed by OPLA

In this section, OPLA is used to drive the selection of amplifier upgrades in the German backbone network with the aim of maximizing the average GSNR of the routing space [65].

Methodology

The optimization targets the maximization of the average GSNR of the paths in the whole routing space by upgrading a given number of optical amplifiers (N_{up}) among the total number of amplifiers (N_{amp}) in the German backbone network B.1. Three selection strategies are investigated: a brute force strategy, a smart brute force and a "minimum degradation" approach. In the brute force strategy every combination is explored with OPLA and the optimum solution is selected. Such a strategy guarantees the optimum solution but the algorithm complexity is binomial and therefore, the computational complexity is very large.The smart brute force approaches the problem by progressively upgrading the N_{up} amplifiers one after the other. This approach does not guarantee the optimum solution but the algorithm complexity is $O(N_{\text{up}} \cdot N_{\text{amp}})$: lower than the brute force. Finally, the "minimum degradation" approach relies on the NSR graph and the occurrences graph to compute a new metric ($m_{\text{NE},i}$) for each amplification site

$$m_{\text{NE},i} = \text{O}_{\text{NE},i} \cdot \text{NSR}_{\text{NE},i} \ . \tag{5.5}$$

Then, the metric $m_{\text{NE},i}$ identifies the critical NEs of a network since it is larger when the NE is frequently used and contemporary it highly impairs the signal quality. Then, by sorting all the NEs by its $m_{\text{NE},i}$, the "minimum degradation" approach provides the order of upgrades of the amplifiers. This approach is fast and can be used when the number of amplifiers is very large and the selection of the amplification upgrades involves many amplification site. The complexity of this strategy is $O(N_{\text{amp}})$, i.e. linear with the number of the amplifier and constant with N_{up}, as the order of the metric automatically provides the upgrading order.

The three strategies are applied to the German network whose topology is depicted in Fig. B.1 and whose parameters are summarized in table B.2. Before any amplifier upgrade, every link is amplified using lumped EDFAs having NF=5 dB, and a total of 65 amplifiers are present. The fibers are SSMF whose parameters are reported in table B.1. The amplification upgrade concerns the improvement of a lumped EDFA with an HFA resulting in a reduction on the effective NF to 0 dB. The network is assumed to be loaded with 95 coherent channels in the 50 GHz WDM grid having a symbol rate of 32 GHz. The routing space has been computed according to a k-shortest path with $k = 5$.

Results

Fig. 5.2 reports the average GSNR vs. number of upgrades for all the approaches: the brute force (yellow curve), the smart brute force (green curve) and the "minimum degradation" (orange curve). Moreover, as the brute force requires the exploration of the entire choice set, the range of values (light blue area) and the average performance among all the cases (blue line) are reported. The results

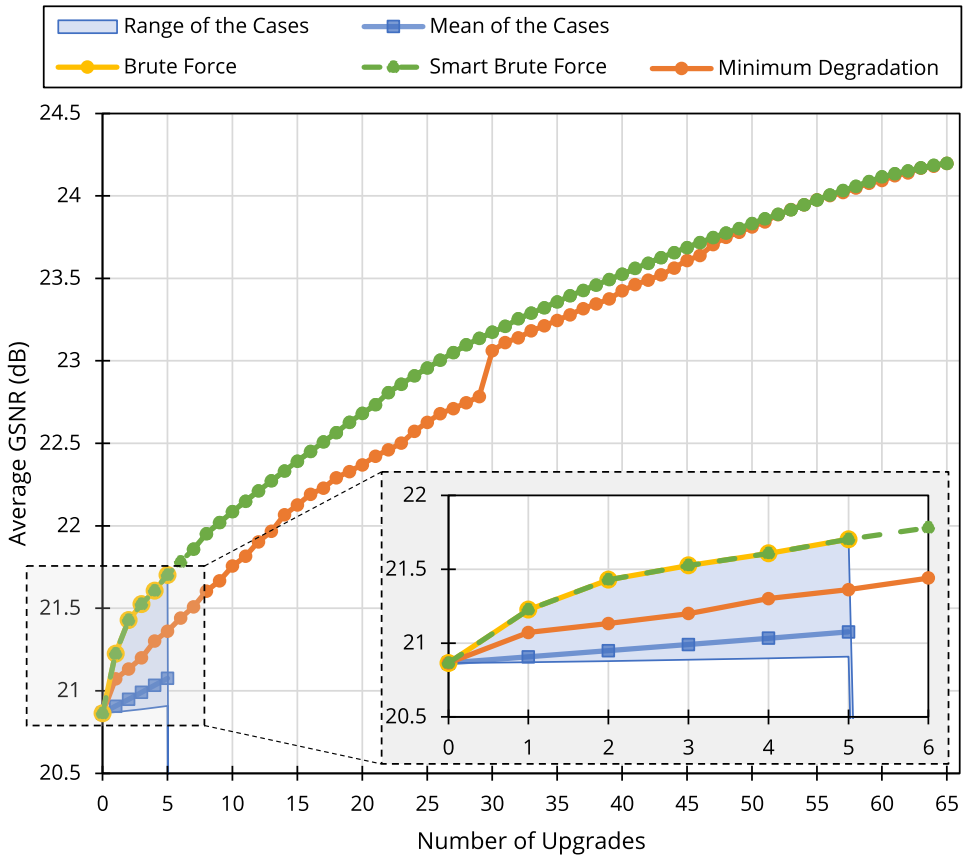

Figure 5.2: Average GSNR for the brute force, the smart brute force and the minimum degradation approach.

of the brute force are computed only up to 5 upgrades because of its computational complexity; for this reason, Fig. 5.2 reports also an enlargement of the figure in the relative area. When no amplifiers are upgraded (N_{up}=0), the average GSNR is equal to 20.9 dB and, when all the amplifiers are upgraded, it goes up to 34.2 dB as expected from the theory (Table II of [39]) saying that the GSNR improvement ΔGSNR is equal to $\frac{2}{3}\Delta$NF. In this case, a ΔNF=5 dB leads to a ΔGSNR of 3.3 dB. After 5 upgrades, the range of values is between 20.9 dB and 21.7 dB, meaning that, the upgrade of only 5 amplifiers gives an improvement of almost 1 dB. Moreover, the mean of the average GSNR among all the candidate solutions reaches only 21 dB, meaning that most of the options lead to an inefficient upgrade. Furthermore, for all the cases in which the brute force has been computed, the smart brute force is always able to provide the same solution. Then, up to 30 upgrades, the "minimum degradation" presents a gap of 0.3 dB with respect to the smart brute force. Such a gap is reduced to 0.1 dB after the 30$^{\text{th}}$ upgrade because the "minimum degradation" approach misses one amplification site which should have been upgraded earlier. Looking more closely at the amplifier in question, this

has a large number of occurrences but a small NSR meaning that the "minimum degradation" approach overweights the occurrences with respect to the NSR. To overcome this issue, a next step could be the generalization of the metric $m_{\mathrm{NE},i}$ such that the weight between $\mathrm{O}_{\mathrm{NE},i}$ and $\mathrm{NSR}_{\mathrm{NE},i}$ can be tuned. For this reason an α parameter is proposed so that the new metric is

$$m'_{\mathrm{NE},i} = \mathrm{O}_{\mathrm{NE},i}^{(1-\alpha)} \cdot \mathrm{NSR}_{\mathrm{NE},i}^{\alpha} \tag{5.6}$$

with $0 \leq \alpha \leq 1$. In this way, the case α=0.5 leads to the same results of $m_{\mathrm{NE},i}$. Observing the smart brute force, in most of the cases, the increment on the average GSNR is smaller with the increase in the number of upgrades; this means that the upgrade of some amplification sites is not very effective and, by integrating OPLA in a TCO analysis it would also be possible to determine the maximum number of upgrades that is convenient to perform on the network.

In conclusion, this section proposes three different approaches in which OPLA can be used to drive the network analysis and upgrades. The choice of using one method of the three methods depends on the size of the network (e.g., metro, regional or long haul networks), the number of upgrades to be investigated, number of different options (e.g., different amplifier models, fiber types and ROADM architectures), the available amount of time and the available computing power. Moreover, a possible solution to close the gap between the smart brute force and the "minimum degradation" has been proposed for a future evolution of the tool.

5.1.2 Technological solutions for OEO regenerator removal

OEO regenerators are devices deployed in the intermediate nodes of a path with the aim of restoring the GSNR of the signal when otherwise the communication would be infeasible. Such devices receive the optical signal, by converting it into the electrical domain and then, they re-transmit the regenerated signal toward the destination node. Despite the fact that OEO regenerators may be used to increase the network capacity by increasing the QoT of the LPs, the use of OEO is limited by their power consumption and their cost. For this reason, the use of advanced DSP techniques [54, 62, 63] and amplification upgrades [25, 62, 63] are investigated to minimize the number of OEO regenerators in a network.

Methodology

The OEO removal strategy has been applied to the Pan-European network (Fig. B.2) and to the USNET (Fig. B.3), whose parameters are summarized in table B.2. The links are composed of uncompensated SSMF and amplified by means of lumped EDFAs having a NF of 5 dB before any upgrade. The 50 GHz WDM grid with 80 channel slots has been assumed. The networks make use of 200 Gbps transceivers generating PM-16QAM modulated signals with a symbol

rate of 32 GBaud. Such transceivers require a pre-FEC BER smaller than $4 \cdot 10^{-3}$ to be in-service. OPLA is used to compute the k-shortest paths with k = 8 and the GSNR of each network; moreover, the wavelengths are assigned according to the first-fit principle. First, the reference scenario has been built by allocating an any-to-any traffic matrix, i.e., one 200 Gbps connection from every node toward every other node has been established. Then, every LP having a GSNR smaller than the target has been labelled as under-performing lightpath (ULP). Along each ULP, the OEO generators are distributed according to the "minimum stops" algorithm [17].

First, a DSP upgrade has been applied to improve the LP GSNR. The upgrade is modelled with a GSNR gain (ΔGSNR). Then, two specific DSP technologies are explored: the DBP and the PS assuming a conservative gain of 0.6 dB [23, 40] and 0.7 dB [46], respectively. Subsequently, also the amplification upgrades have been investigated for the same purpose, by replacing the EDFAs with HFAs and thus, by changing the NF, from 5 dB, down to 0 dB.

Results

In the Pan-European network, the baseline scenario before any upgrade presents 572 ULPs over 756 LPs (75.6% of the LPs are under-performing) and the ULPs require a total of 1108 OEOs to keep the network working, for an average of 1.94 OEOs per ULP. A total of 1864 transceiver pairs are used. The baseline of the USNET network has 29 ULPs on 552 LPs (5.2% of the LPs are under-performing) and they require 29 OEOs. Hence, each ULP requires only 1 OEO. Moreover, 581 transceiver pairs are used. The Pan-European network has a higher number of ULPs and it requires more OEOs. This is due to the lower average node degree of the Pan-European network and to the higher average link length.

Figs. 5.3 report the impact of using advanced DSP techniques in the Pan-European network. In detail, Fig. 5.3a reports the percentage of ULP that are enabled by only OEOs (red), by both the DSP upgrade and OEOs (gray) and by the DSP upgrade only (blue) by changing ΔGSNR. It can be observed that, the number of ULPs enabled by DSP and by DSP+OEO increases almost linearly with ΔGSNR. Moreover, the growth rate of ULPs enabled by DSP is 17% per dB while the one of ULPs enabled by DSP+OEO is 30% per dB. Fig. 5.3b reports the percentage of removed OEOs by changing ΔGSNR. The amount of OEOs decreases by 27.8% per dB. Finally, Fig. 5.3c reports the number of upgraded transceivers. Such a quantity increases by 240 units per dB from 0 dB up to 1 dB of ΔGSNR. Then, it reaches a total of 478 upgrades when ΔGSNR is 1.5 dB. It can be noted that, also a small gain of 0.1 dB can give some benefits as 14 LPs are enabled and 10% of the OEOs are removed.

Figs. 5.4 report the benefits of DSP on the USNET network. Fig. 5.4a reports the percentage of ULPs enabled by OEOs (red) and by DSP (blue). No hybrid

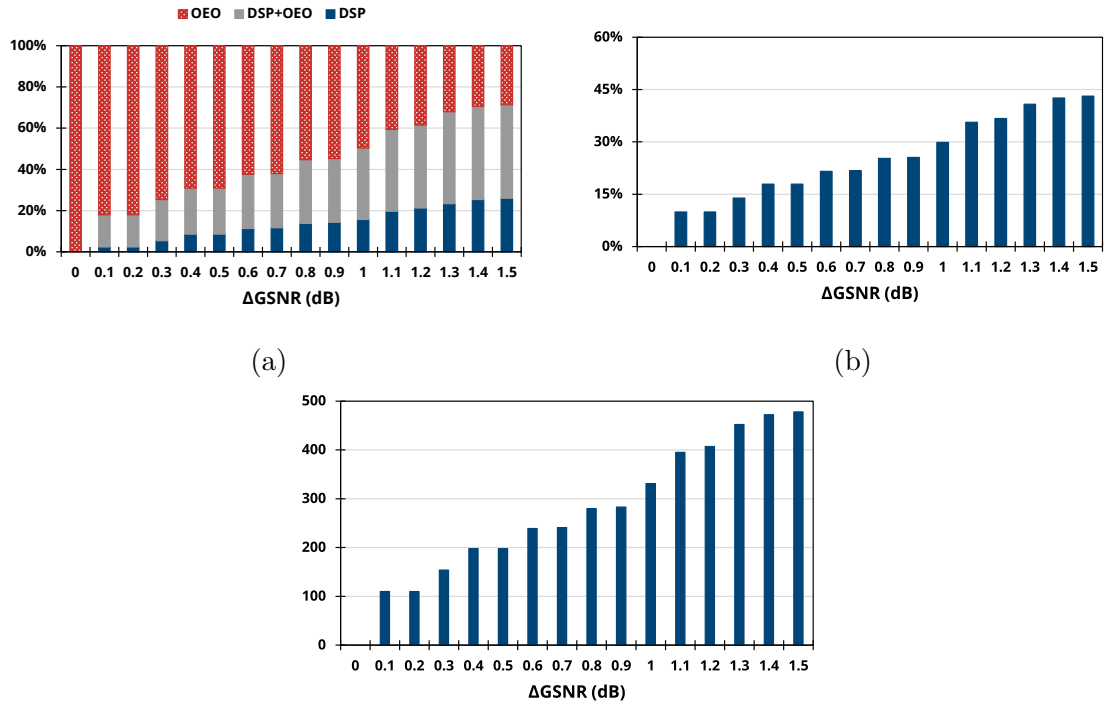

Figure 5.3: The percentage of ULP enabled by OEO, hybrid OEO+DSP and DSP (a); the percentage of removed OEO regenerators (b); and the number of upgraded DSPs in the Pan-European network.

DSP+OEO solutions are reported as the baseline scenario presents only one regenerator per ULP. The percentage of DSP-enabled ULPs goes to 100% after just 0.9 dB of ΔGSNR and a DSP gain of 0.1 dB is enough to enable 20% of the ULPs to be fully transparent. Moreover, Fig. 5.4b reports the percentage of removed OEOs vs. ΔGSNR showing that, with 0.9 dB, all the OEOs are removed. Furthermore, Fig. 5.4c reports the number of upgraded transceiver pairs showing that the promotion to the full transparency of the network needs the upgrade of only 29 transceiver pairs. In the USNET network, an improvement of 0.1 dB makes transparent 20% of the ULP and permits the removal of 20% of the regenerators by upgrading 5 transceiver pairs. In general, values of ΔGSNR larger than 0.9 dB result superfluous since, for ΔGSNR equal to 0.9 dB the network reaches the full transparency. Finally, Table 5.1 summarizes the impact of two specific advanced DSP techniques for which the GSNR advantage is known: the DBP (ΔGSNR=0.6 dB [23, 40]) and the PS (ΔGSNR=0.7 dB [46]). On the Pan-European network, both the techniques make transparent 11% of the ULPs and they allow the removal of 26% of the ULPs

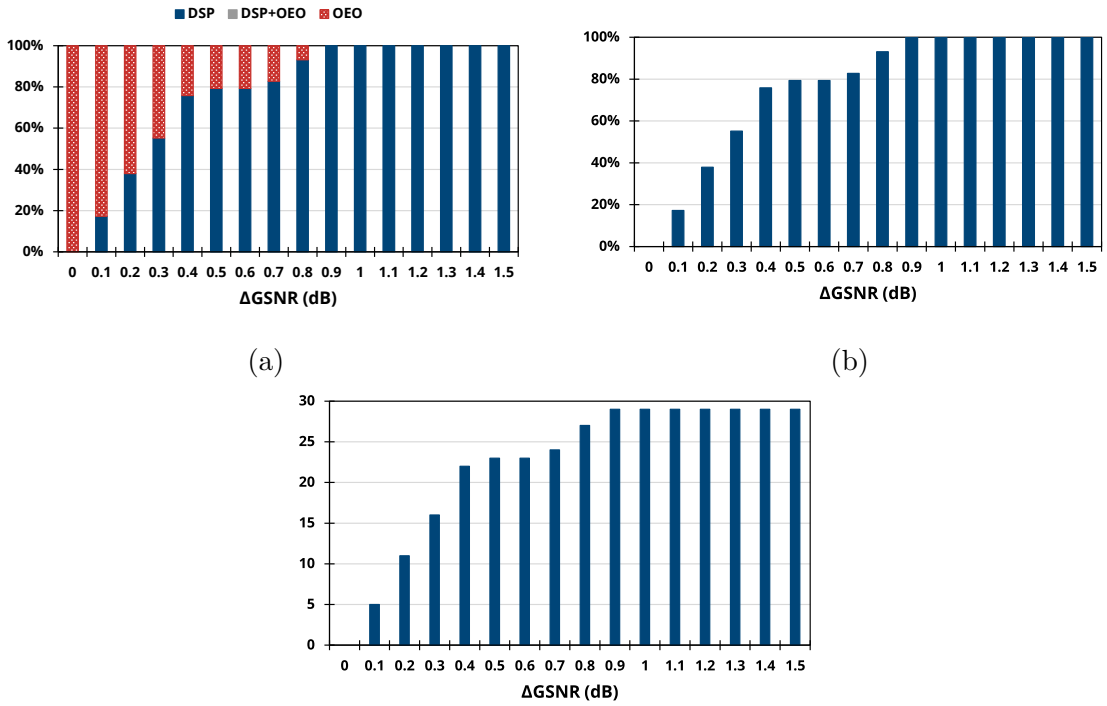

Figure 5.4: The percentage of ULP enabled by OEO, hybrid OEO+DSP and DSP (a); the percentage of removed OEO regenerators (b); and the number of upgraded DSPs in the USNET network.

	DBP		PS	
	Pan-European	USNET	Pan-European	USNET
DSP enabled ULPs	65 (11%)	23 (79%)	67 (12%)	24 (83%)
DSP+OEO enabled ULPs	150 (26%)	0 (0%)	150 (26%)	0 (0%)
Removed OEOs	238 (21%)	23 (79%)	240 (22%)	24 (83%)
Upgraded transceivers	239	23	241	24

Table 5.1: Benefits of DBP and PS.

if 240 transceiver pairs are upgraded. On the USNET network, the upgrades enable 83% of the LPs and the removal of 83% of the OEO regenerators by upgrading 23-24 transceivers.

Figs. 5.5 report the results obtained for the Pan-European network by promoting the amplification sites from lumped EDFA to HFA and therefore, by improving the equivalent NF of the amplifiers from 5 dB (no HFA upgrades) down to 0 dB. In

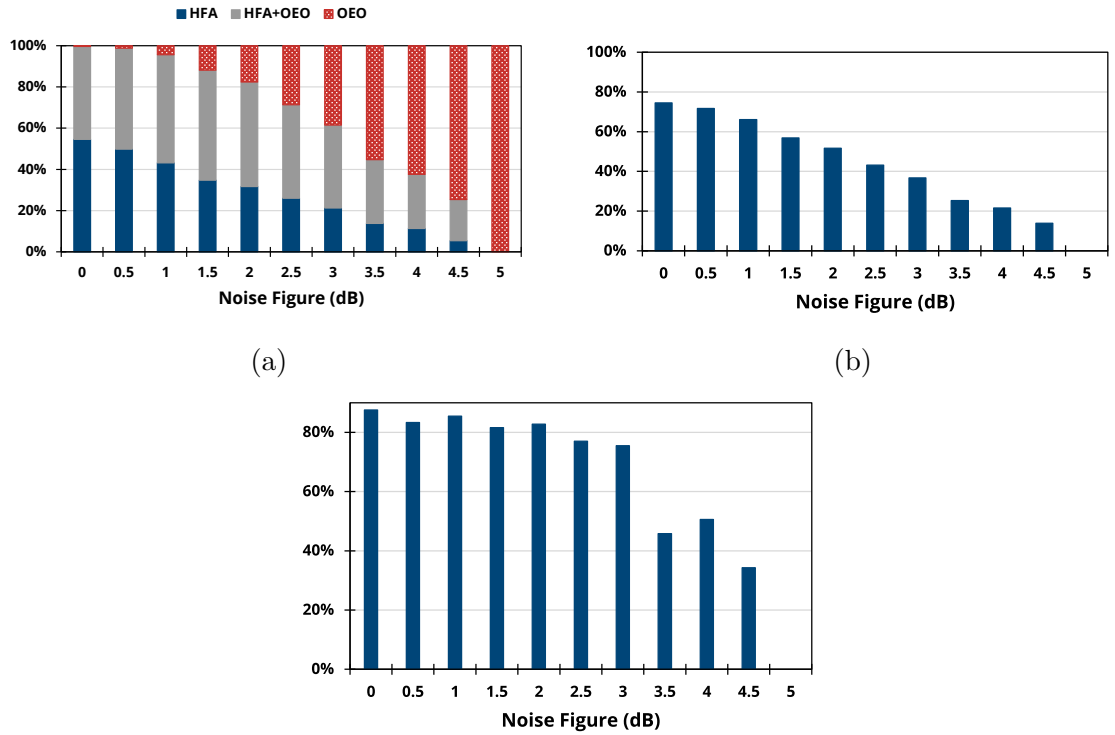

Figure 5.5: The percentage of ULP enabled by OEO, hybrid OEO+HFA and HFA (a); the percentage of removed OEO regenerators (b); and the number of upgraded amplifiers in the Pan-European network.

detail, Fig. 5.5a reports the percentage of ULPs enabled by solely OEO regenerators (red), HFA+OEO (gray) and only HFA (blue). Even a small improvement of 0.5 dB which reduces the NF to 4.5 dB, reduces to 75% the percentage of ULPs enabled by OEO regenerators, and, 5% of them are fully transparent. Furthermore, by reducing the NF to 0 dB, almost all the ULPs are enabled by HFA or HFA+OEO as only 0.4% of the ULPs are enabled by solely OEO regenerators. The percentage of HFA enabled ULPs increases with a rate of 11% per dB when reducing the NF and the percentage of HFA+OEO enabled ULPs has growth rate of 9% per dB. Fig. 5.5b reports the percentage of OEO removed by improving the NF. This trend is almost linear as 15% of OEOs can be removed for each dB of improvement in the amplifier NF. Moreover, when the NF goes down to 0 dB, 75% of the OEOs are removed. Fig. 5.5c reports the percentage of upgraded amplifiers. Such a quantity is not monotonic with NF since, on one side, a smaller NF increases the number of removed OEO regenerators and therefore the number of amplifiers to be upgraded, while, on the other side, a smaller NF makes more effective the

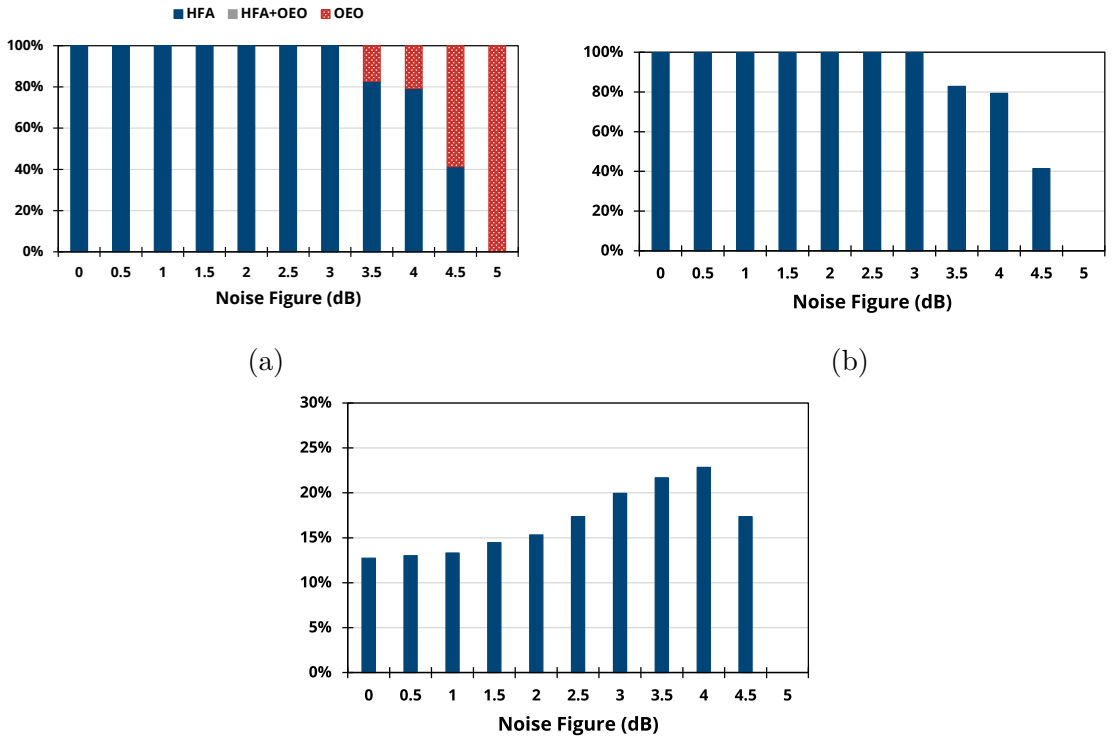

Figure 5.6: The percentage of ULP enabled by OEO, hybrid OEO+HFA and HFA (a); the percentage of removed OEO regenerators (b); and the number of upgraded amplifiers in the USNET network.

benefit of each HFA and, therefore, the number of amplifiers needed to remove an OEO is reduced. Moreover, when the NF reduces between 4.5 dB and 3.5 dB, the number of upgraded amplifier oscillates between 30% and 50%, and then, by further decreasing the NF, such quantity increases to 90%.

Figs. 5.6 report the same results for the USNET network. As shown in Fig. 5.6a, a reduction in the NF of 2 dB is enough to make the network fully transparent. Moreover, no hybrid solutions using both OEOs and HFA are present since all the ULPs present only one regenerator. Then, a NF of 3 dB or smaller removes all the OEO regenerators. Even if a further reduction in the NF below 3 dB does not help in removing any regenerator, as shown in Fig. 5.6c, it is possible to reduce the percentage of upgraded amplifier from 20% (NF=3 dB) to 13%.

In general, comparing the two networks, both the DSP upgrades and the amplifier upgrades are more effective in the USNET than in the Pan-European network since, the ULPs require, in general, a smaller GSNR improvement to reach the threshold GSNR. This is due to the larger average node degree and the smaller

average link length of the USNET network, which lead, on average, to a larger GSNR of the LPs. Moreover, due to the similar GSNR gain, the DBP and the PS lead to similar network benefits. The highlighted benefits, properly combined with a techno-economic analysis, can be exploited to trade-off costs and benefits of the network upgrades.

5.2 Statistical Network Assessment Process

SNAP [22, 37] is a network analysis tool that performs dynamic simulations by progressively loading the network within a Monte Carlo framework. Therefore, as opposite to OPLA, SNAP may show a temporal evolution of the network by evaluating load dependent metrics such as the blocking probability and the actual allocated traffic. However, due to the computational complexity, SNAP can not be used to analyze a wide range of network configurations. For this reason, OPLA and SNAP are complementary tools for assessing the performances of the optical networks.

5.2.1 The structure of SNAP

Fig. 5.7 depicts the flowchart of SNAP. The input parameters required by the tool are: the description of the network's physical layer, the traffic model and the RWA algorithm. The network description is provided in the form of a weighted graph having N_{nodes} nodes representing the ROADM nodes and N_{links} weighted edges representing the links of the network. The weight $w_{i,j}$ of each edge connecting the node i to the node j is the NSR of the corresponding link and it includes both the ASE noise and the NLI. Such a graph can be computed using the GNPy's QoT-E. The traffic model is provided in the form of a probability matrix having size $N_{\text{nodes}} \times N_{\text{nodes}}$, in which, each element $p_{i,j}$ represents the probability that a connection request between the node i and the node j occurs. Consequently, SNAP performs a Monte Carlo simulation where the sequence of connection requests are randomly generated according to the probability matrix. Therefore, the connection probability can, in general, either be different for each node pair or uniform, and it does not depend on the prior history. In detail, SNAP performs N_{MC} Monte Carlo iterations in which, each run starts from an empty network having no allocated LPs. Then, SNAP randomly extracts a connection request according to the traffic model and it attempts the allocation of the resources according to the RWA algorithm. If the resources allow the provisioning of the LP, the connection request is accepted, the network resources are reserved to the LP for the rest of the network's life, the capacity of the LP is computed according to the LP's GSNR and the information is stored. Otherwise, if according to the RWA algorithm, the network is not able to accommodate the connection request, it is rejected and a

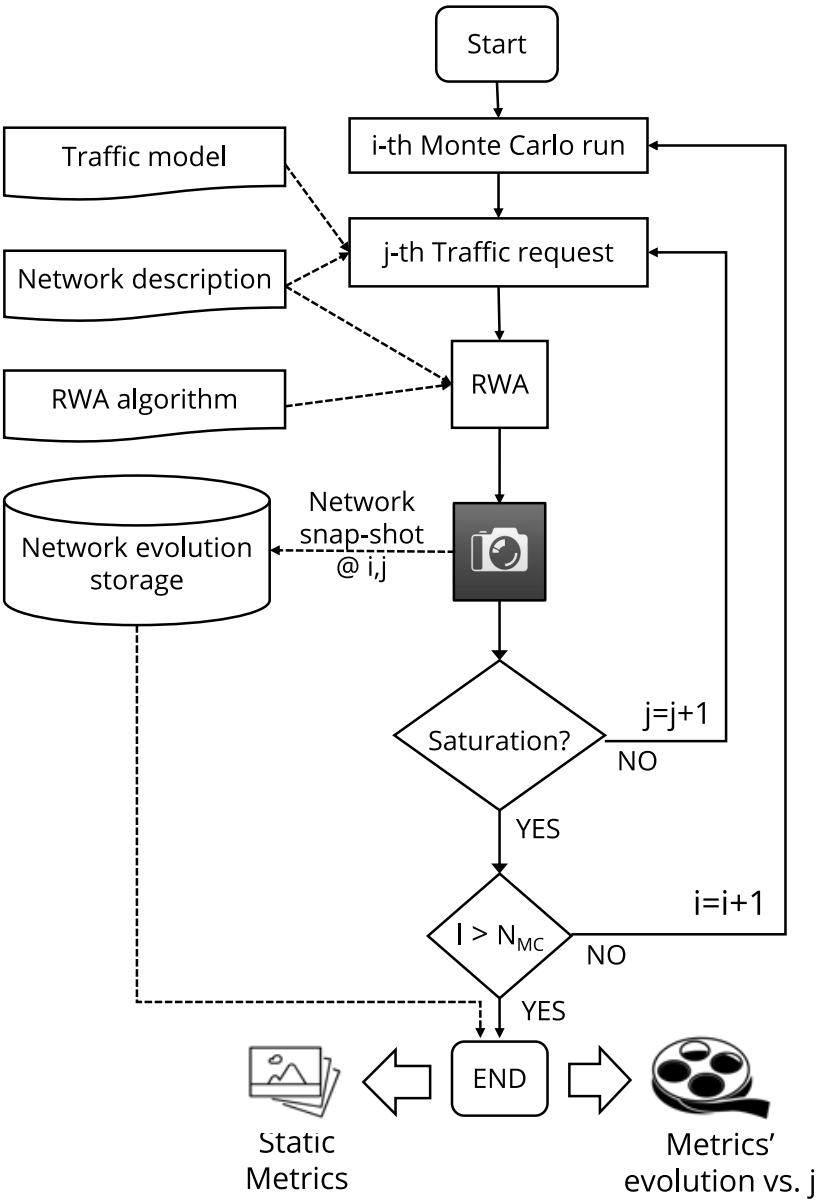

Figure 5.7: The flowchart of SNAP.

blocking event is registered. Then, other connection requests are extracted until the network reaches the saturation state, i.e., until the blocking probability and the number of requests reach a given threshold. This entire procedure is repeated N_{MC} times and every metric is averaged among the different Monte Carlo iterations.

The remainder of the section makes use of SNAP to compare the networking benefit of several SDM techniques [52, 53] (section 5.2.2) and multi-band technology [55, 56] (section 5.2.3).

5.2.2 Networking Merit of SDM Technologies

This section compares the network performance of two SDM technologies [50, 179]: uncoupled fiber ribbon (UFR) and strongly-coupled multi-core fiber (SCMCF). The UFR consist in a set of independent parallel single mode fibers and, therefore, it allows a complete network flexibility. Whereas, the SCMCF are multi-core fibers presenting a strong core coupling, which helps in mitigating the NLI [7, 150], but it requires the joint switching (JoS) [128] of all the cores for a wavelength because of the strong coupling. Consequently, this technologies improves the QoT at the cost of reducing the network flexibility. Moreover, in order to investigate also different ROADM architectures [105, 107, 149], the UFR has been explored considering both the independent switching (InS) [128] and the core-continuity constrain (CCC) [149].

Methodology

This investigation has been performed on the German network (Fig. B.1), whose network parameters are summarized in Table B.2. The analysis compares SCMCF with JoS and UFR with both InS, CCC and JoS. Since the case of UFR with JoS does not present non-linear mitigation and it is the less flexible solution, it is used as a reference to evaluate both the benefit due to non-linear mitigation and to the ROADM flexibility. For both the technologies we considered the typical SSMF fiber propagation parameters as reported in table B.1. Moreover, the spatial cardinality of 3, 5 and 7 is explored, i.e., the number of parallel cores. The lumped EDFA have a NF of 5 dB and each ROADM introduces a loss of 18 dB recovered by a BST amplifier. The transceivers operate in the C-band in the 50 GHz greed, for a total of 96 channels. The signals are RRC shaped with a roll-off of 0.15 and a symbol rate of 32 GBaud. The transceivers are able to flexibly adapt the LP capacity to the GSNR. The GSNR has been computed by means of GNPy and, the GSNR enhancement due to the non-linear mitigation has been computed according to [7]. The working point of the amplifiers is computed according to the LOGO algorithm [127].

The traffic requests are generated according to an uniform any-to-any distribution. The routes are computed according to a KSP algorithm having $k = 25$. The wavelength and the spatial assignment follows a first fit approach. SNAP has been applied to each scenario by performing 25,000 Monte Carlo runs for every case.

Therefore, the blocking probability vs. total allocated traffic has been computed and, in order to compare solutions having different spatial cardinality, the total allocated traffic has been normalized with respect to the spatial cardinality.

Results and Comments

Fig. 5.8 reports the blocking probability vs. allocated traffic normalized to the spatial cardinality for the reference UFR with JoS (dotted lines) and for the UFR with CCC (dash-dotted lines) and with InS (dashed lines) using 3 (orange), 5 (blue) and 7 (green) parallel fibers per link. The outcomes of SCMCF (solid lines) using 3 (orange), 5 (blue) and 7 (green) cores are also reported. The UFR with JoS shows, as expected, the same performances by changing the number of fibers meaning that the capacity growth is proportional to the number of fibers. This is due to the fact that this solution does not present GSNR improvements nor any increase in the network flexibility. However, the ROADM complexity is very low. Moreover, when the blocking probability is medium and low - below 0.1 -, the gain due to the non-linear mitigation of SCMCF never overcomes the gain in network flexibility of CCC and InS. However, this gain decreases with the increase in the number of parallel fibers and cores. The SCMCF reaches the performance of UFR with CCC, only when the blocking probability is very large: 0.2, 0.15 and 0.14 when the number of fibers/cores is 3, 5 and 7, respectively. Moreover, the SCMCF crosses the UFR with InS only when the blocking probability is 0.23 when 3 parallel fiber/cores are used and it is 0.19 otherwise. Moreover, the gain of InS, with respect to CCC is very small being always smaller than 4.3, 5.7 and 5.8 Tbps when using 3, 5 and 7 parallel fibers, respectively. This corresponds to a relative gain of 1.35%, 1.7% and 1.7%. Therefore, the use of CCC instead of InS allows a strong reduction in the ROADM complexity - from quadratic to linear - at the cost of a small reduction in the allocated traffic.

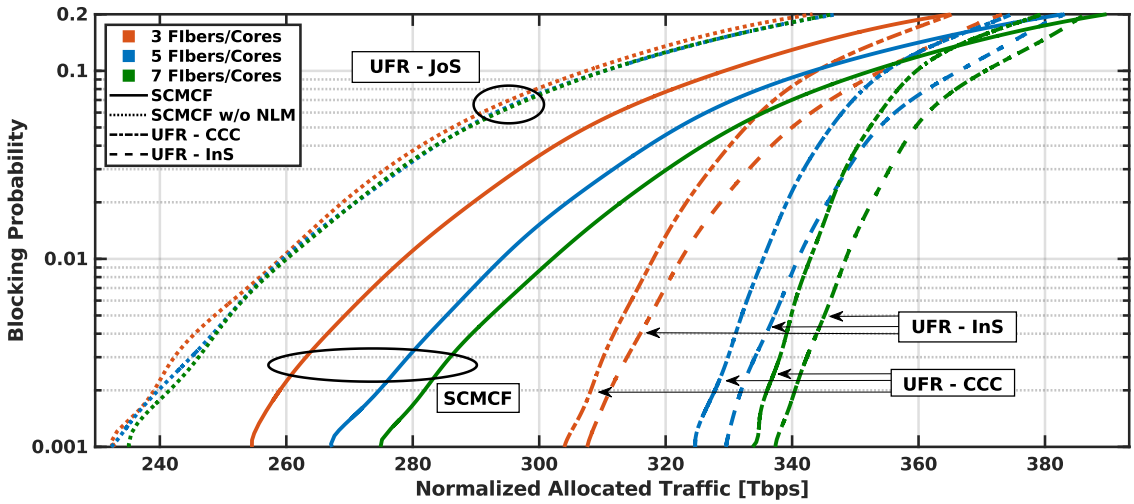

Figure 5.8: Blocking probability vs. allocated traffic normalized to the number of fibers/cores for a different number of cores and SDM solution.

Fig. 5.9 depicts the relative gain of each technology with the reference UFR

with JoS at blocking probability equal to 0.01 for 3, 5 and 7 parallel fibers or cores. The non-linear mitigation enables the allocation of an extra 20, 36 and 43 Tbps per core. While, CCC allows the accommodation of 59, 72 and 84 Tbps per fiber using 3, 5 and 7 fibers. Finally, InS allocates an extra traffic of 64, 82 and 90 Tbps per fiber.

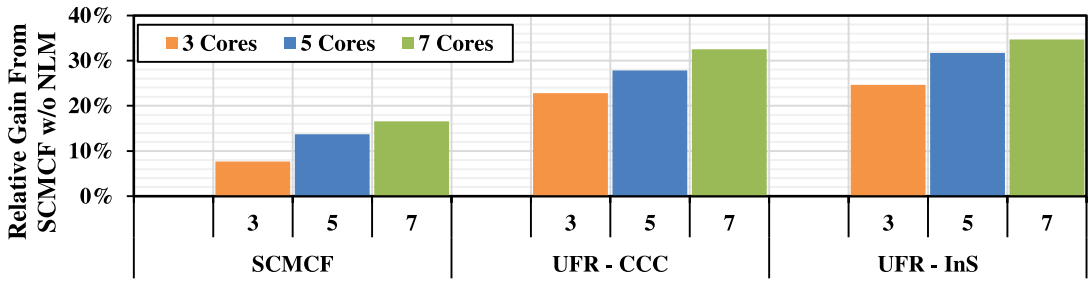

Figure 5.9: Relative gain respect to the reference UFR with JoS at blocking probability equal to 0.01.

In conclusion, the UFR with CCC shows a great trade-off in terms of ROADM complexity and capacity growth for reasonable values of blocking probability, making a good solution for the German network.

5.2.3 A Networking comparison of SDM and multi-band transmission

This section analyzes and compares the capacity upgrade of an optical network in absence of available dark fibers exploring two different possibilities: the adoption of SDM [50, 179] using UFRs or band-division multiplexing (BDM) [58, 67, 71]. In this context, if an SDM solution involving UFR is adopted, it requires the deployment of new fiber pairs without any GSNR penalty, while, the use of multi-band transmission can avoid the deployment of new cables by extending the channels to all the low-loss U-, L-, C-, S-, E- and O-bands for a total of 50 THz between 1360 nm and 1675 nm the GSNR of the channels will be poorer because of the SRS and the Kerr effect.

Methodology

This investigation compares network upgrade targeting the increase of the number of fiber pairs - from here on indicated as SDM technology - with the one targeting the increase of the occupied bandwidth (from here on indicated as BDM technology). In order to quantify each upgrade, it has introduced the following quantities: the SDM cardinality (N_{SDM}) indicating the number of parallel fiber pairs and the BDM cardinality (N_{BDM}) indicating the multiplicative factor in terms of

bandwidth occupation with respect to the use of 80 channels in the C-band. Moreover, to fairly compare the two technologies the multiplexing cardinality (N_{M}) is also defined as the product between N_{SDM} and N_{BDM} of each scenario. Therefore, both pure and mixed solutions are investigated by exploring different values of N_{M} in the set {1, 2, 3, 4, 6, 12}. Hence, all the combinations of N_{SDM} and N_{BDM} explored in the different scenarios are listed in the Table 5.3. The case of $N_{\mathrm{M}} = 1$ represents the reference case in which only one fiber pair is used ($N_{\mathrm{SDM}} = 1$) and only 80 channels in the C-band are used (N_{SDM} =1). Hence, the scenarios are divided into four categories:

1. Reference ($N_{\mathrm{SDM}} = 1$ and $N_{\mathrm{BDM}} = 1$);
2. Pure BDM ($N_{\mathrm{SDM}} = 1$ and $N_{\mathrm{BDM}} = N_{\mathrm{M}}$);
3. Pure SDM ($N_{\mathrm{SDM}} = N_{\mathrm{M}}$ and $N_{\mathrm{BDM}} = 1$);
4. Mixed BDM/SDM scenarios ($N_{\mathrm{SDM}} \neq 1$ and $N_{\mathrm{BDM}} \neq 1$).

Moreover, increasing N_{BDM}, a larger number of spectral slots (N_{λ}) are used and therefore, other bands than the C-band are occupied. Hence, Table 5.2 shows the total number of spectral slots, the total occupied bandwidth and the occupation of such slots in the U, L, C, S, E, O-bands when the N_{BDM} increases.

The analysis was carried out over the German network (Fig. B.1) and the USNET (Fig. B.3) whose parameters are summarized in Table B.2. The German network includes 17 nodes and 26 links having an average length of 207 km. The covered area has a diameter of ∼600 km. The USNET network has 24 nodes and 44 links with an average distance of 308 km and the covered area has a diameter of ∼4000 km. Therefore, they have similar node degrees but different covered areas. Coherent elastic transceiver operates in the 50 GHz grid at a symbol rate of 32 GBaud, enabling the use of up to 80 channels for each 4 THz spectral slot. The fiber type is assumed to be SSMF and the parameters used for this analysis are reported in Fig. B.5 and in Table B.3. Multi-band amplifiers are used to recover the fiber attenuation every 75 km. The noise figure of each amplifier is reported in table B.3 and, after each amplifier, a GFF is used to compensate the spectral ripples and tilts introduced by the propagation. The multi-band GSNR has been computed following the strategy depicted in section 4.2.

The traffic is generated according to a uniform any-to-any distribution. The paths are computed according to a KSP algorithm with k = 15 and the wavelengths are assigned according to a first fit principle. By using SNAP the networks are progressively loaded up to the saturation of the network then, the blocking probability and the allocated traffic are evaluated. Then, the allocated traffic is normalized with respect to N_{M} to make the comparison among the different scenarios fair.

Table 5.2: BDM bandwidth occupation.

N_{BDM}	N_λ	Number of channels per band						Total Bandwidth
		U	L	C	S	E	O	
1	80	-	-	80	-	-	-	4 THz
2	160	-	80	80	-	-	-	8 THz
3	240	-	137	80	23	-	-	12 THz
4	320	-	137	80	103	-	-	16 THz
6	480	80	137	80	183	-	-	24 THz
12	160	108	137	80	183	296	156	48 THz

Table 5.3: N_{M}, N_{BDM} and N_{SDM} of each investigated upgrades.

	Pure BDM		Mixed Upgrades						Pure SDM	
N_{M}	N_{BDM}	N_{SDM}	N_{BDM}	N_{SDM}	N_{BDM}	N_{SDM}	N_{BDM}	N_{SDM}	N_{BDM}	N_{SDM}
1	1	1	-	-	-	-	-	-	1	1
2	2	1	-	-	-	-	-	-	1	2
3	3	1	-	-	-	-	-	-	1	3
4	4	1	2	2	-	-	-	-	1	4
6	6	1	3	2	2	3	-	-	1	6
12	12	1	6	2	4	3	3	4	2	6	1	12

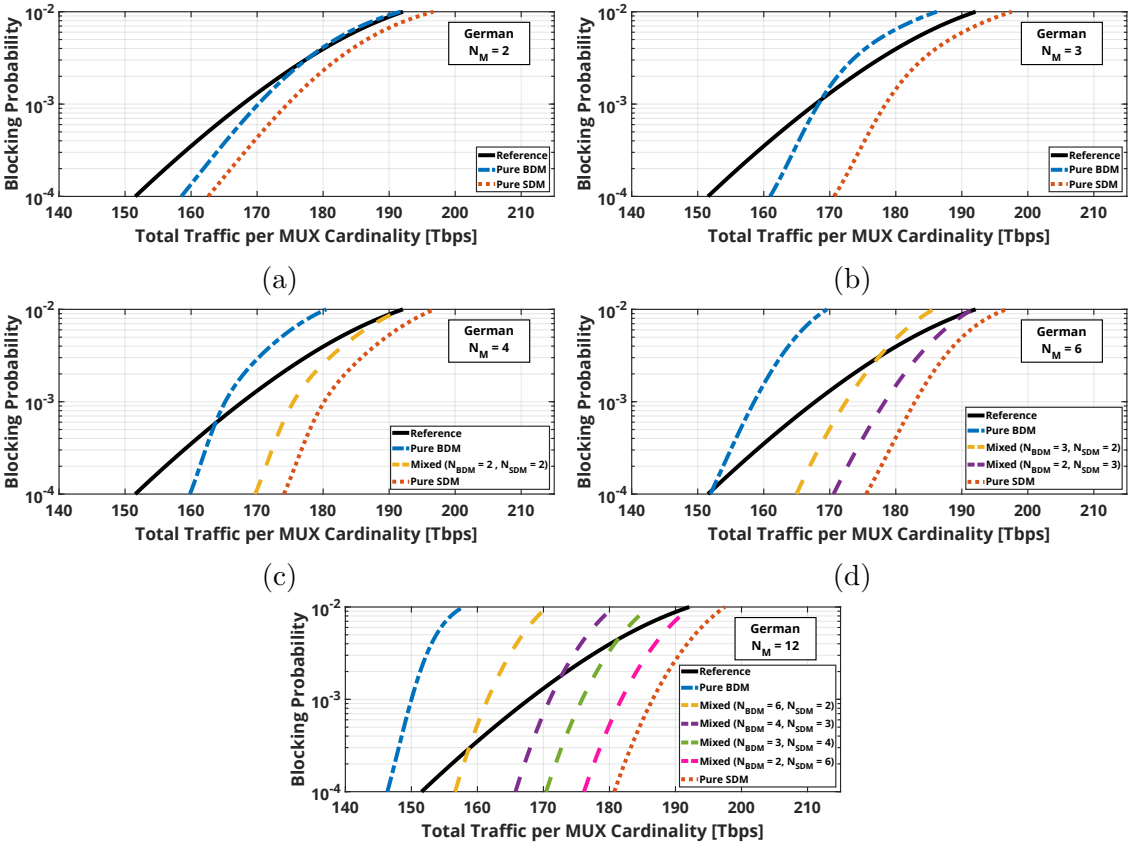

Figure 5.10: Network performances in the German topology by varying the multiplexing cardinality N_M: 2 (a), 3 (b), 4 (c), 6 (d) and 12 (e).

Results and Comments

Figs. 5.10 and Figs. 5.11 report the blocking probability vs. normalized allocated traffic in the German network and in the USNET network, respectively. The traffic is normalized with respect to the multiplexing cardinality. Each sub-figure refers to a different multiplexing cardinality: $N_{\mathrm{M}} \in \{2, 3, 4, 6, 12\}$. Every figure reports the single fiber pair C-band reference scenario ($N_{\mathrm{M}} = 1$), the pure SDM scenarios (blue dash-dotted lines), the pure BDM scenarios (red dotted lines) and the mixed scenarios (dashed lines). For $N_{\mathrm{M}} = 2$ (Fig. 5.10a and Fig. 5.11a), both the pure SDM and pure BDM present similar performances compared to the reference even if both present some gain owning to the higher network flexibility introduced by the larger number of available frequency slots for the BDM and by the larger number of fibers per link for the SDM as they reduce the number of blocking events. The gap between the BDM and the SDM is caused by the poorer propagation performances of the LPs in case of BDM. By comparing the two networks, the result are similar,

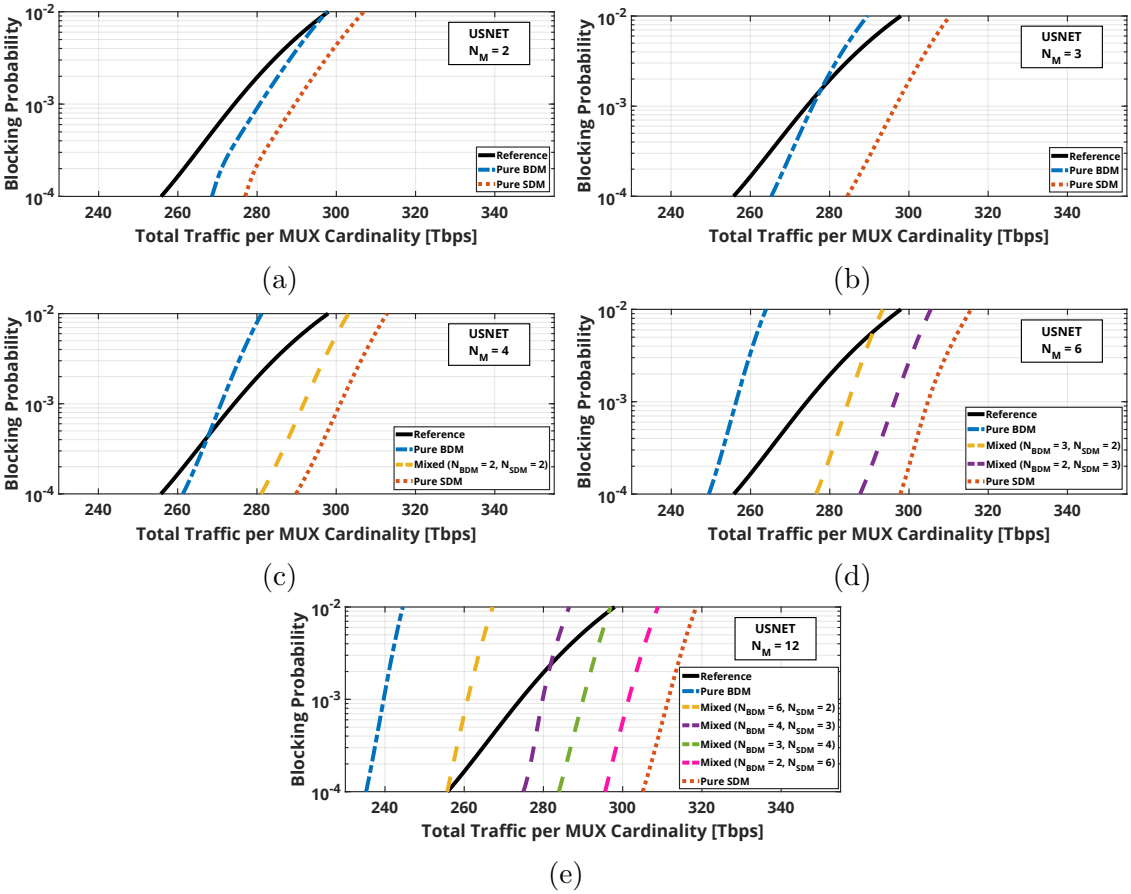

Figure 5.11: Network performances in the USNET topology by varying the multiplexing cardinality N_M: 2 (a), 3 (b), 4 (c), 6 (d) and 12 (e).

mainly because the node degree is similar, the main difference is in the total amount of allocated traffic which is larger in the USNET network because of the different network size. Moreover, as expected, pure SDM upgrades are always the best performing scenarios as they do not experience any extra propagation impairment with the increase of N_{M}. Then, enlarging N_{M} to 3 (Fig. 5.10b and Fig. 5.11b) and to 4 (Fig. 5.10c and Fig. 5.11c), the outcomes evolves according to the observations of $N_{\mathrm{M}} = 2$. As expected, the pure BDM is parallel to the pure SDM with a rigid horizontal shift caused by the poorer propagation performances and, consequently, the gap increases with N_{M}. Therefore, the mixed cases are in between with similar trends and gaps. The outcomes at N_{M} of 6 (Fig. 5.10d and Fig. 5.11d) and 12 (Fig. 5.10e and Fig. 5.11e) show a further enhancement on the phenomena seen in the previous cases. Therefore, as expected, the pure SDM is the best performing solution giving an increase in the allocated traffic with respect to the reference of 17% and 16% when N_{M} is equal to 6 in the German network and in the USNET network, respectively. Moreover, for $N_{\mathrm{M}} = 12$ the gain increases to 20% for both the

topologies. On the opposite side, pure BDM scenarios represent the lower bound because of the larger propagation impairments and the loss with respect to the reference is 12% and a 10% in case N_{M} is equal to 6 for the German network and in the USNET network, respectively, and, in case N_{M} is 12, the loss grows up to 18% for both the networks. As expected, the mixed upgrades show intermediate behaviours, and, in particular, when $N_{\mathrm{BDM}} \leq 4$, the penalty is always limited to 2% with respect to the reference. Comparing the two networks, the behaviour is similar even if the dimensions are different in fact, they present similar gaps and slopes. They differ mainly in the absolute value of the total allocated traffic that is lower in the German network due to the lower available resources. Therefore, the obtained results can reasonably be generalized to any medium and large scale core network having a similar average node degree.

The results are then synthesized as normalized traffic at the blocking probability 10^{-3} for the German network (Fig. 5.12a) and the USNET network (Fig. 5.12b). For both the networks, the pure SDM provides a capacity growth with respect to the reference of 5%, 7%, 8%, and 10% for N_{M} equal to 2, 3, 4 and 6, respectively. This gain is introduced by the increase in the network flexibility with N_{M}, while the GSNR of the LPs does not decrease. For the pure SDM solutions, the performances of the two networks diverges only for $N_{\mathrm{M}} = 12$, where the gain from the reference is 12% for the German network and 17% for the USNET network. This is due to the higher average node degree of the USNET network which enables higher flexibility when N_{M} grows. Moreover, in both the networks, pure BDM solutions show a small gain of 2% with respect to the reference when $N_{\mathrm{M}} = 2$. Such a gain is almost 0% for N_{M} equal to 3 and 4 having a balanced compensation between the gain due to flexibility and the loss due to the poor QoT. Then, when N_{M} grows up to 6, the BDM solutions present a small capacity penalty of 6% in both the networks, which enlarges to 9% and 12% when $N_{\mathrm{M}} = 12$ for the German network and the USNET network, respectively. This happens since the network flexibility is no more able to fully compensate the GSNR penalty, caused by the bandwidth extension.

In conclusion, BDM is a good solution to enhance the network capacity up to an 8 THz C+L+S system ($N_{\mathrm{M}} = 4$, 320 WDM channels) as it presents some gain or negligible penalties with the advantage of exploiting the already deployed fibers. After that, it is necessary to move toward a mixed SDM/BDM solution if significant capacity losses are not accepted.

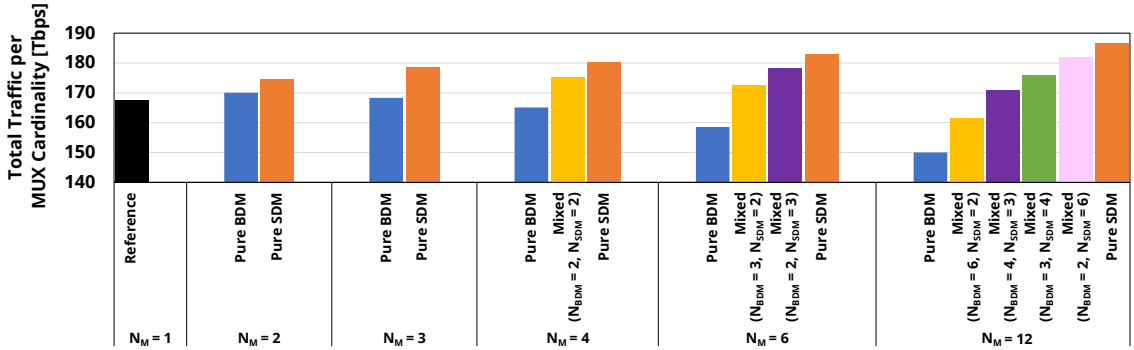

(a)

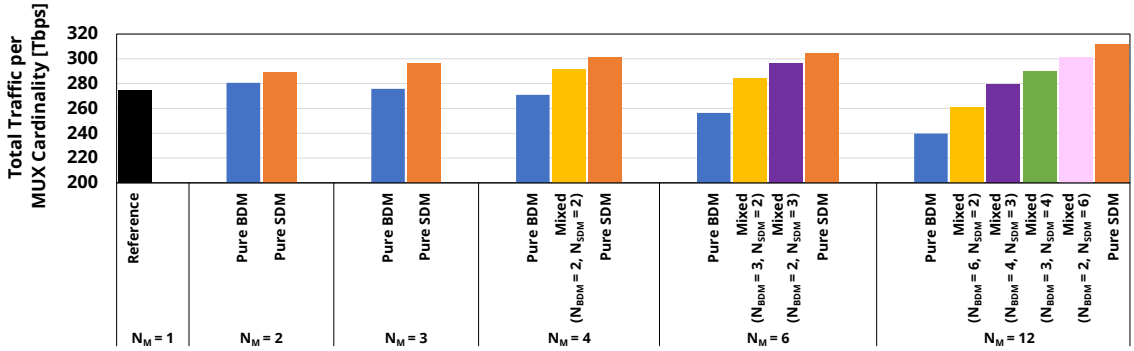

(b)

Figure 5.12: Total traffic per MUX cardinality @blocking probability 10^{-3} in German (a) and US-NET (b) topologies.

Chapter 6

Network orchestration and automation

SDN targets the centralization of the network management [120]. This is achieved through the disaggregation of the control plane from the data plane, the development of a centralized controller, the adoption of open interfaces between the data plane and the control plane, and the possibility to configure the network devices through these interfaces [158].

In this context, open source projects such as OpenDaylight (ODL) [109] and open network operating system (ONOS) [76] began with the aim of automating the optical networks.

SDN solutions have been applied to the optical layer, as demonstrated recently in [36, 102, 184]. In detail, in [102] the QoT is inferred by monitoring the OSNR in real time, while in [184] some machine learning technique has been leveraged to achieve the physical layer awareness.

This chapter describes the integration of a QoT-E implementing the GN-model in the PROnet SDN orchestrator [111] to enable a physical layer aware network automation over a commercial network [83] hosted in the Open Networking Advanced Research (OpNeAR) laboratory [170] in the University of Texas at Dallas (UTDallas) campus and in the ViaWest data center in Dallas. This enables the orchestrator to evaluate the feasibility of a path and to perform a decision on the modulation format that can be applied before the actual provisioning a LP. This chapter first reviews the architecture of the PROnet orchestrator in section 6.1, then, in section 6.2, a detailed description of the network used for the experiment and, finally, in section 6.3, the QoT-E integration and validation is detailed.

The material reported in this chapter was previously published in [57].

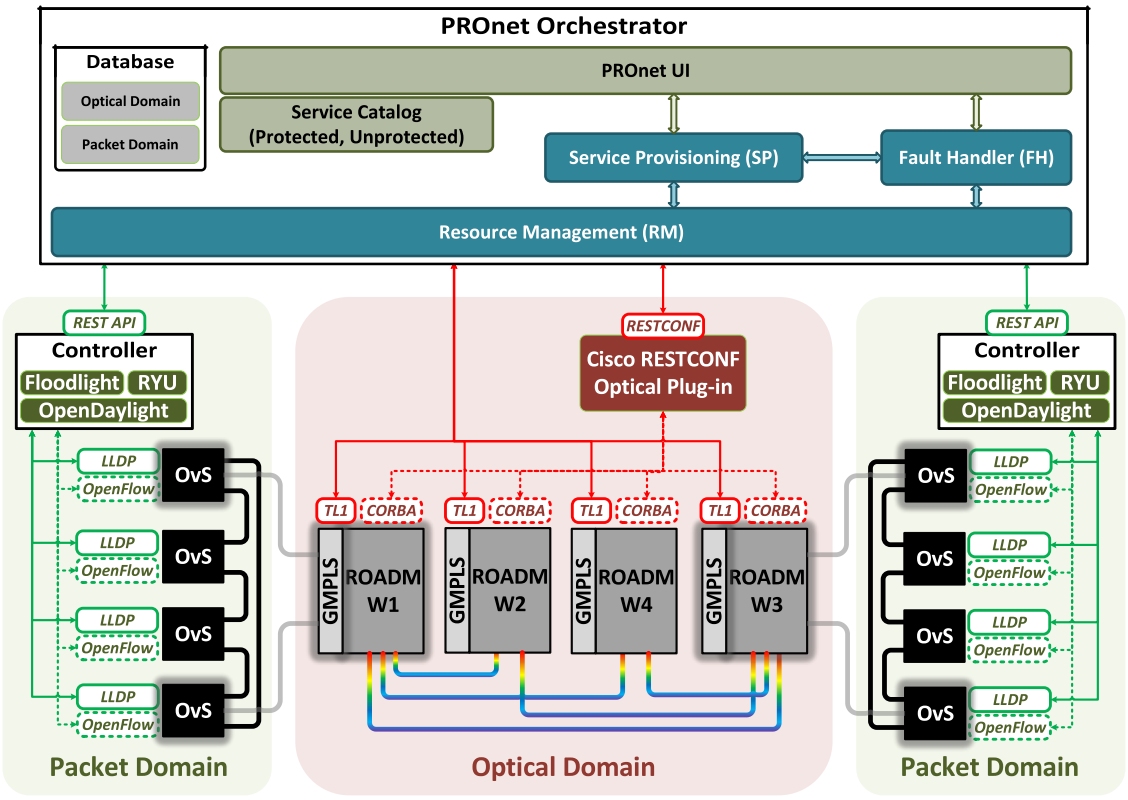

Figure 6.1: The software and hardware architecture.

6.1 The PROnet SDN orchestrator architecture

Fig. 6.1 depicts the optical domain and the packet domain, together with the orchestrator and the interfaces among the orchestrator and the optical and the packet domains. The optical domain includes four ROADM nodes called W1, W2, W3 and W4 connected together by five amplified optical links. The optical domain can be interfaced by means of a RESTCONF based vendor-proprietary optical plug-in or by means of the transaction language 1 (TL1) protocol in case a direct interaction with the optical equipment is needed. The packet domain consist of two Open vSwitch (OvS) Ethernet switches connected to the ROADMs W1 and W3. The Ethernet switches support the ODL [109], the Floodlight (FL) [97, 139, 176] and the Ryu [118] controllers, and it manages the switches by means of OpenFlow as a southbound interface. Moreover, the Ethernet controllers allow the use of link layer discovery protocol (LLDP) [85] to discover the layer-2 network resources and the network topology.

The architecture of the PROnet orchestrator consist of a database where all the useful information is stored and four main modules: the resource management (RM), the service provisioning (SP), the service catalog (SC) and the Fault

Handler (FH). The database organizes the information in two main categories: the optical domain related information and the packet domain related information. The RM module collects information about the network topology and the network configuration by using a REST API to interface with the Ethernet controller and the RESTCONF optical plugin. This information is stored in a database and it is organized into two different categories: optical domain related data and packet domain related data.

The SP and the SC modules are in charge of setting up the traffic flows in the network. To do that, they first, discover the network resources by means of LLDP [85], then, the KSP algorithm is executed to compute the k shortest paths, and finally, a multi-path service is used to enable the transfer of data between two hosts by selecting two disjointed paths and then by connecting the Ethernet switches. The multi-path service is used also to implement a load-balancing mechanism to fairly distribute the traffic between the two disjointed paths. This load-balancing has been implemented by using a Linux kernel function called bonding. The aim of this function is to bond the Ethernet interfaces of the two paths so that they are seen as a single interface. Owing to the bonding functionality, when an outage causes the out of service of a path, all the traffic is rerouted along the other bonded path. The FH module is in charge of establishing another redundant path that substitutes the path out of service.

Finally, the PROnet orchestrator provides to the end user an graphical user interface (UI) to perform the network operations by sending high level commands that are internally managed by the orchestrator itself.

In this context the QoT-E can be exploited each time a path is computed to determine in advance the best feasible modulation format and therefore, to allocate the exact resources needed every time a traffic request comes, avoiding multiple attempts.

6.2 The network structure

The detailed scheme of the optical domain is depicted in Fig. 6.2 and the photos of the network equipment are shown in Figs. 6.3. PROnet is a four node network having a rectangular topology with one diagonal. TheROADM nodes Akard (W1), P Building (W3) and TBD (W4) are located in the UTDallas campus, while ViaWest (W2) is located in a ViaWest data center. The Nodes W1 and W3 are three degree ROADM nodes, while W2 and W4 are two degree nodes. Every node degree is equipped with a BST amplifier to set the optimum output power and a pre-amplifier amplifying the incoming channels. Every link is bidirectional and the fiber is SSMF. In order to restore the channel power, every 75 km, the signal is amplified with an ILA. The link between W1 and W2 is 225 km long and amplified every 75 km. Instead, the link between W2 and W3 is amplified every 50 km. The

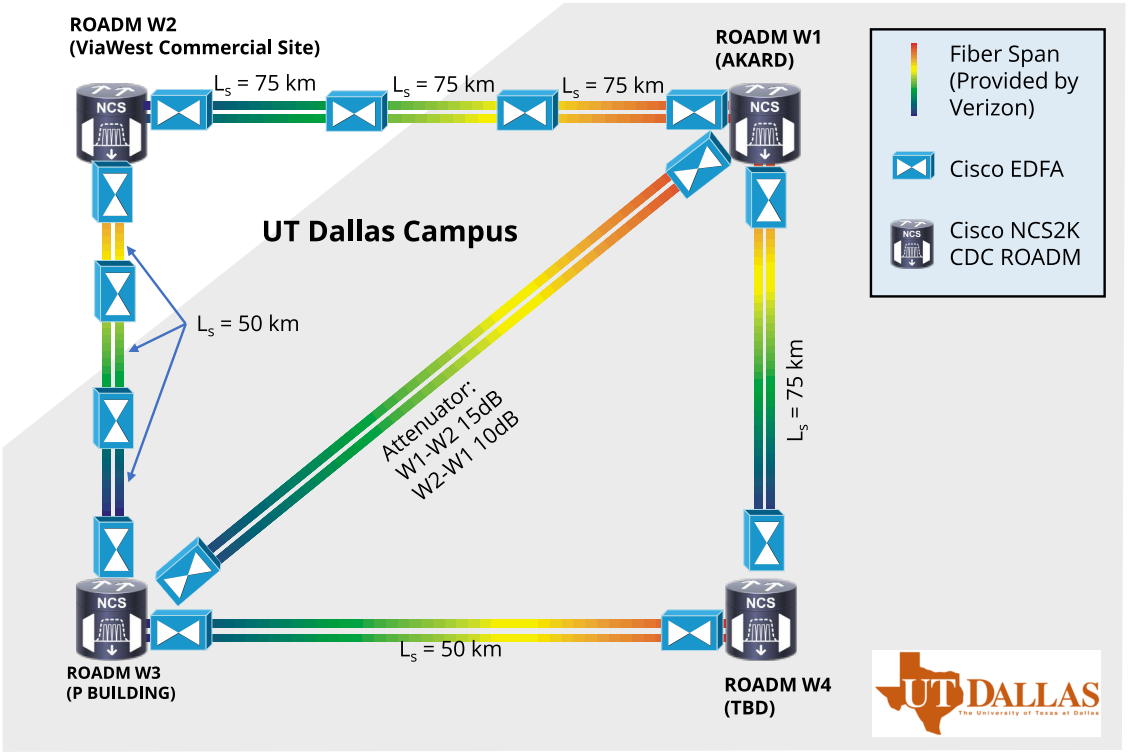

Figure 6.2: Detailed scheme of the PROnet optical domain.

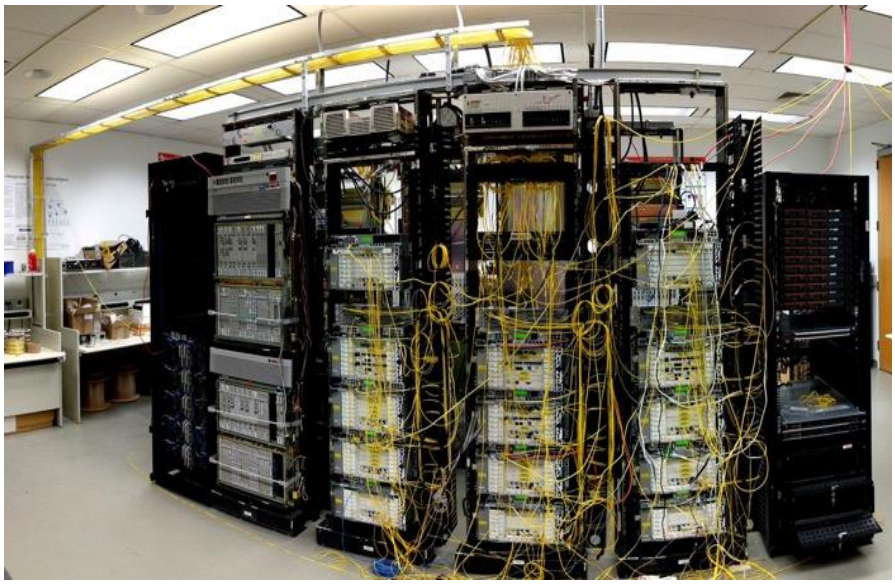

(a)

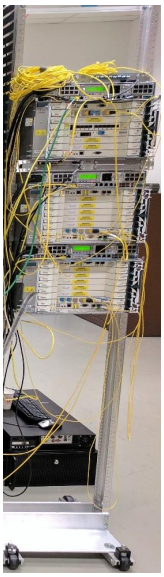

(b)

Figure 6.3: A photo of the commercial equipment hosted in the OpNeAR in the UTDallas campus (a) and in ViaWest (b).

links between W3 and W4 and between W4 and W1 are, instead, single span links whose length is 50 km and 75 km, respectively. Finally, W3 and W1 are connected using a patch cord and an optical attenuator which emulates a fiber span. All the optical amplifiers involved are EDFAs, and thus, no Raman amplifiers have been used.

Every ROADM node has been equipped with multi-rate DWDM line card with transponder capabilities able to select different modulation formats: PM-QPSK (100 Gbps), and PM-8QAM (150 Gbps) PM-16QAM (200 Gbps). The signals are RRC with a roll-off factor of 15%.

6.3 The QoT-E integration and validation

The integrated QoT-E makes use of all the information collected by the RM and stored in the database to retrieve a complete description of the physical layer. Then, each time that the SP module computes a path in the network, it calls the QoT-E module which computes the GSNR under the assumption of full spectral load - as it is a worst case assumption - and then, it writes this information in the database in a dedicated table. In this way, the orchestrator can retrieve the estimated GSNR of the path every time that it is needed. Then, when the path is allocated, the best modulation format is chosen by comparing the GSNR threshold of each modulation format with the estimated GSNR.

Experiments have been carried out to validate the accuracy of the QoT-E [57]. The validation has been performed by comparing the actual GSNR of the LP under test with the QoT-E. The LP under test is transmitted at 1547.32 nm from the node W4, then it transparently passes through the node W1 and W2 and it is received at the node W3. The resulting path is 450 km long. The channel under test is root-raised cosine shaped and PM-16QAM modulated with a symbol rate of 32 GBaud. Moreover, a total of 48 "alien wavelengths" have been inserted into the line system to make relevant also the NLI effect. The concept of "alien wavelength" consists in transporting "alien" signals across the WDM [110, 163, 172] network. These channels have been emulated by properly shaping with an optical interleaver the ASE noise generated by an EDFA. The alien wavelengths have been generated in the 50 GHz WDM fixed grid with a -3 dB bandwidth of 37.5 GHz. The LP under test has been positioned in the middle of the comb. Furthermore, the gain of the amplifiers has been configured by the line system controller. The measured GSNR has been obtained by following the procedure described in section 3.3.1.

Two different launched PSD strategies have been tested (Figs. 6.4): a flat power per channel strategy (Fig. 6.4a) and a flat power spectral density strategy (Fig. 6.4b). In detail, the flat power spectral density consists of equalizing the power-to-bandwidth ratio ($\frac{P_i}{B_i}$) of each channel. For each of the two strategies a power sweep has been performed by varying the transmitted power by a power

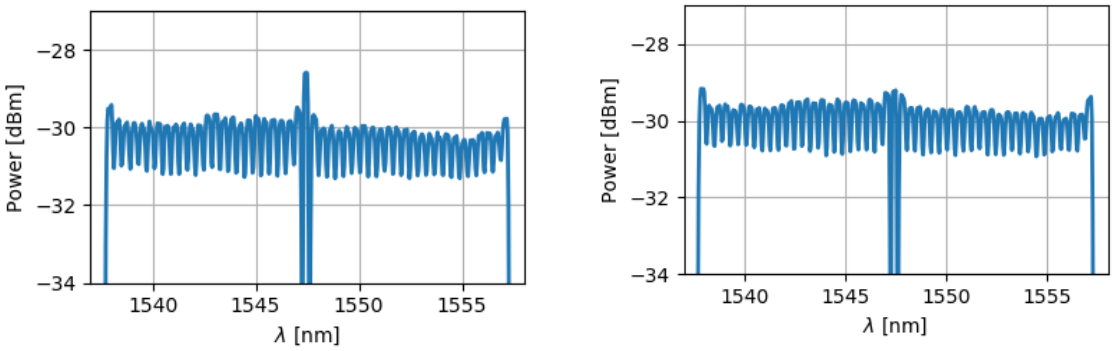

(a) (b)

Figure 6.4: The PSD with equal power per channel (a) and equal peak power spectral density (b).

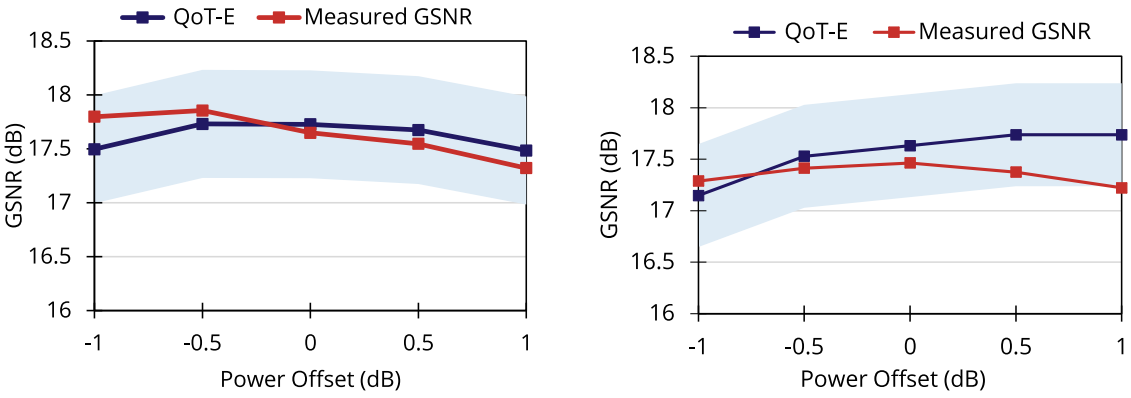

(a) (b)

Figure 6.5: The GSNR varying the transmitted power with equal power per channel (a) and equal power spectral density (b).

offset in a range of ±1 dB.

Figs. 6.5 report the measured GSNR (red line) and the estimated GSNR (blue curve) with a ±0.5 dB error bar (light blue) in case of equal power per channel (Fig. 6.5a) and equal power spectral density (Fig. 6.5b). The estimations are in good agreement with the measurement being the error always within 0.5 dB. Moreover, the estimation is not always conservative as it would be expected by the GN-model. This is due to the uncertainty on the system parameters eroding such a conservative margin. Moreover, the accuracy in predicting the optimum power, i.e., the power maximizing the GSNR of the channel in the middle of the comb [127, 138], is always within 1 dB.

In conclusion, the QoT-E module has been embedded in the PROnet orchestrator, which can now exploit such a module to rapidly and efficiently provision LPs

in optical networks in support of host-to-host big data transfer.

Chapter 7

Conclusions and Future Works

In this thesis, the physical layer has been discussed and analyzed following a disaggregated vendor-agnostic paradigm. An open source tool for analyzing the network performances has been described and experimentally validated. Moreover, a novel network design tool has been proposed and innovative technological solutions have been investigated and compared. Finally, a physical layer aware orchestrator has been proposed and experimentally validated.

7.1 Summary

This thesis starts introducing the topic by reviewing the history of the modern optical communication by retracing the fundamental milestones that have revolutionized this technology.

Then, the fundamentals of optical transmission and networking are described in depth. The general structure of optical networks is introduced and then each network element is dissected by describing the operation of the transmitter, the fiber, the amplifier, the ROADM node and the receiver. Then, the weighted graph is presented as an effective abstraction of the physical layer in which each link is characterized by the GSNR degradation that it introduces. Finally, the basics of RWA are reviewed.

Nowadays, the operators are pushing the market toward the openness and the disaggregation of the network devices. In such a context, GNPy is proposed as a vendor-agnostic tool to estimate the QoT in an optical network in full compatibility with a multi-vendor and multi-generation playground. Indeed, given a description of the physical layer, the engine of GNPy is able to provide an accurate estimation of the GSNR. The reliability of such a QoT-E has been proven through a validation campaign both in the laboratory and on the field. In particular, the most extensive validations have been carried out in the Microsoft laboratory and over the Microsoft core network.

As the operators target the maximization of the return on the investment on the installed equipment, the multi-band technology goes in this direction, since it increases the network capacity without requiring the deployment of new fibers. For this reason, indeed, multi-band C+L line systems are already commercially available and are being installed. In this thesis, a simple but effective optimization strategy for multi-band line system controlling has been proposed. Then, the capacity of fully loaded multi-band point-to-point communication has been assessed exploring several applications (DCI, metro and regional networks) and several configurations including Raman amplification. The outcomes show that multi-band transmission can potentially accommodate 7 to 10 times more traffic than a simple C-band system.

Then, two network design tools have been introduced - OPLA and SNAP - and used. In detail, the offline tool OPLA has been adopted to address some Raman placement strategies to effectively increase the network capacity. OPLA has been employed also to assess the effectiveness of using Raman amplification and advanced DSP techniques to save regenerators. Then, SNAP has been used to compare the network benefit of several SDM solutions and multi-band transmission.

Lastly, an integration of the QoT-E in the PROnet network orchestrator to enable a physical layer aware automation and orchestration has been shown and experimentally validated.

7.2 Next Steps

The topic of physical layer awareness for open optical networking is a promising area that offers many opportunities for investigations.

A YANG model describing the input parameters of GNPy is in the process of definition. Moreover, the GNPy's QoT-E is being extended to include mixed-rate flex-grid networks and the filter and cross-talk penalties introduced by the ROADM nodes. Moreover, there is an ongoing activity in collaboration with Links Foundation [169] and Lumentum to build a vendor-agnostic open and disaggregated network automation infrastructure over a multi-vendor open line system. Such a framework will be based on the ONOS SDN controller [76] interfaced with an open line system controller (OLSC) to control a multi-vendor commercial network hosted in the Links laboratories. The OLSC makes use of GNPy as a driving force to optimize the network.

Moreover, the multi-band transmission is a promising technology for effectively increasing the network capacity. The optimization paradigm proposed in this thesis is an initial step that has to be refined by using more advanced optimization techniques and cost functions. Furthermore, also the optimization on the dynamic gain equalizer (DGE) deployment and on the use of Raman amplification has to be investigated in-depth. Furthermore, it is worth to investigate the adoption of a

guard-band between groups of bands to *isolate* them by minimizing the inter-band SRS for the purpose of simplifying the management of multi-band upgrades.

SNAP and OPLA are powerful instruments to analyze the performance of the network and therefore, they should integrate cost metrics in order to trade off costs and benefits in TCO analysis.

Finally, the computation of the propagation delay and the transceiver latency should be implemented either in GNPy and in OPLA and SNAP to include the impact of the physical layer on the quality of service (QoS) that a network can provide.

Appendix A

The Raman scattering

This appendix details the mathematical description of the Raman scattering [142]. The Raman scattering involves the SRS and the spontaneous Raman scattering. In general, the Rayleigh back-scattering plays a role while assessing the SRS, however, it has been shown that, in silica core fiber (SCF), its impact on the SRS is negligible when the power of the Raman pumps is smaller than 800 mW [81]. For this reason, in this thesis, the effect of the Rayleigh back-scattering in the Raman scattering is neglected.

The SRS is a power transfer from the higher frequencies toward the lower ones and it is described by the set of N ordinary differential equations (ODE) [18]: one for each WDM channel and for each Raman pump. Each equation describes the power evolution $\partial_z P(z, f_i)$ of the i-th channel along the spatial variable z. The set of equations is:

$$\begin{cases} \pm\partial_z P(z,f_1) = & -\alpha_{\mathrm{p}}(f_1)P(z,f_1) + \\ & \sum_{j=2}^{N} C_{\mathrm{R}}(f_1,f_j)P(z,f_j)P(z,f_1) \\ & \vdots \\ \pm\partial_z P(z,f_i) = & -\alpha_{\mathrm{p}}(f_i)P(z,f_i) + \\ & \sum_{j=i+1}^{N} C_{\mathrm{R}}(f_i,f_j)P(z,f_j)P(z,f_i) - \\ & \sum_{j=1}^{i-1} \frac{f_j}{f_i} C_{\mathrm{R}}(f_i,f_n)P(z,f_j)P(z,f_i) \\ & \vdots \\ \pm\partial_z P(z,f_N) = & -\alpha_{\mathrm{p}}(f_i)P(z,f_N) - \\ & \sum_{j=1}^{N-1} \frac{f_N}{f_j} C_{\mathrm{R}}(f_N,f_j)P(z,f_j)P(z,f_N)\ . \end{cases} \tag{A.1}$$

The equations are sorted from the lower to the higher frequency. The $\pm$ sign indicates the propagation direction: the "+" is for co-propagation and the "−" is for counter-propagation. $\alpha_{\mathrm{p}}(f)$ is the power attenuation coefficient of the fiber and the term $\alpha_{\mathrm{p}}(f_i)P(z,f_i)$ of each equation describes the linear attenuation of the signal at the i-th frequency. Each element $+C_{\mathrm{R}}(f_i,f_j)P(z,f_j)P(z,f_i)$ of the

summation is a Raman gain term of the equation - to be noted that $f_i < f_j$ -; $P(z, f_j)$ is the power at the frequency f_j and $C_{\mathrm{R}}(\Delta f_{i,j})$ is the Raman coefficient evaluated in $\Delta f_{i,j} = |f_i - f_j|$. The Raman coefficient of the various fiber types can be retrieved from [132]. Furthermore, the term $-\frac{f_j}{f_i} C_{\mathrm{R}}(f_i, f_n) P(z, f_j) P(z, f_i)$ is the power depletion toward the lower frequency channels. It can be observed that it is very similar to the gain term except for the "$-$" sign which indicates a power loss and for the the vibrations loss term ($\frac{f_j}{f_i}$). The boundary conditions of the ODEs $P(z_0, f_i)$ are given by the transmitted power at each frequency $P_{\mathrm{TX}}(f_i)$; the co-propagating signals will have the boundary condition in $P(0, f_i) = P_{\mathrm{TX}}(f_i)$, while, counter-propagating pumps will have the boundary condition at the end of the fiber span: $P(L_{\mathrm{s}}, f_i) = P_{\mathrm{TX}}(f_i)$.

Since the equations are all coupled together, in general, this set of ODEs has not an analytical solution. For this reason a numerical solver is used to evaluate the solution. Once the system has been solved, the solution will be a function $P(z, f_i)$. Starting from the solution it is possible to define the overall gain/loss profile of the fiber ($\rho(z, f)$) as:

$$\rho(z, f_i) \triangleq \sqrt{\frac{P(z, f_i)}{P(z_0, f_i)}} \,. \tag{A.2}$$

Consequently, the power gain/loss of each fiber can be described by the function $\rho(z, f)$ which also includes the linear attenuation. For this reason, the overall effect of the attenuation and the SRS of a fiber span can be described together by an equivalent filter having transfer function $H_F(f) = \rho(L_{\mathrm{s}}, f)^2$.

The spontaneous Raman scattering is described by another set of ODEs [18] which solution is the evolution of the ASE noise ($P_{\mathrm{ASE}}(z, f_i)$) generated by the spontaneous Raman scattering along the fiber over the signal bandwidth. The equations are in the form

$$\begin{aligned} \pm \partial_z P_{\mathrm{ASE}}(z, f_i) = & -\alpha_{\mathrm{p}}(f_i) P_{\mathrm{ASE}}(z, f_i) + \\ & \sum_{j=i+1}^{N} C_{\mathrm{R}}(f_i, f_j) P(z, f_j) P_{\mathrm{ASE}}(z, f_i) - \\ & \sum_{j=1}^{i-1} \frac{f_j}{f_i} C_{\mathrm{R}}(f_i, f_n) P(z, f_j) P_{\mathrm{ASE}}(z, f_i) + \\ & \sum_{j=i+1}^{N} C_{\mathrm{R}}(f_i, f_j) \left[1 + \eta(T)\right] h f_i R_{\mathrm{s}} P(z, f_j) \,. \end{aligned} \tag{A.3}$$

The spontaneous Raman equations are very similar to the SRS equations, but they are no more coupled among each other thus, they can be solved independently. The spontaneous Raman equations differ in the presence of the non-homogeneous terms $C_{\mathrm{R}}(f_i, f_j) \left[1 + \eta(T)\right] h f_i R_{\mathrm{s}} P(z, f_j)$, where h is the Plank's constant, R_{s} is the

symbol rate of the i-th channel and $\eta(T)$ is the phonon occupancy factor

$$\eta(T) = \frac{1}{exp\left(\frac{h|f_j - f_i|}{k_B T}\right) - 1} \tag{A.4}$$

where T is the temperature, k_B is the Boltzmann's constant. Moreover, as the ASE noise generated by a signal is completely negligible, only the non-homogeneous terms in which $P(z, f_j)$ refers to the power of a Raman pump are considered [18]. Moreover, in this case, the boundary conditions are given by the ASE noise at the input of the fiber which is zero. And thus, $P_{\text{ASE}}(0, f) = 0$.

Then, all you need to model the spontaneous Raman scattering is the ASE noise at the end of the fiber: $P_{\text{ASE}}(L_s, f_i)$.

Finally, for every WDM signal $s_i(t)$, the GSNR due to the Raman scattering can be simply computed as:

$$\text{GSNR}_{\text{SRS}} \triangleq \frac{P(L_s, f_i)}{P_{\text{ASE}}(L_s, f_i)} = \frac{P_{\text{ch,in}}(f_i)\,\rho(L_s, f_i)^2}{P_{\text{ASE}}(L_s, f_i)} \tag{A.5}$$

Appendix B

Fiber Parameters, Reference Topologies and Multi-Band parameters

This appendix reports the typical fiber parameters and the network topologies used in this thesis. Also, the parameters used for multi-band transmission are reported.

B.1 Fiber Parameters

This section reports, in the table B.1, the typical fiber parameters such as the attenuation coefficient (α), the chromatic dispersion (D) and the nonlinear coefficient (γ). Table B.1 lists these parameters for the SSMF, NZDSF, NDSF, ELEAF and TWRS.

B.2 Network Topologies

The backbone network topologies analyzed in this thesis are: the German network B.1, the Pan-European network B.2 and the north American USNET network B.3. The distribution of the link length of each network is depicted in Fig. B.4. The summary parameters and the references of these networks are reported in table B.2.

Table B.1: Fiber parameters.

Fiber type	Attenuation (α)	Chromatic Dispersion (D)	Nonlinear Coefficient (γ)
SSMF	0.2 dB/km	16.7 ps/nm/km	1.27 1/W/km
LEAF	0.222 dB/km	3.8 ps/nm/km	1.45 1/W/km
NDSF	0.222 dB/km	3.8 ps/nm/km	1.45 1/W/km
ELEAF	0.2 dB/km	4 ps/nm/km	1.41 1/W/km
TWRS	0.24 dB/km	6 ps/nm/km	1.84 1/W/km

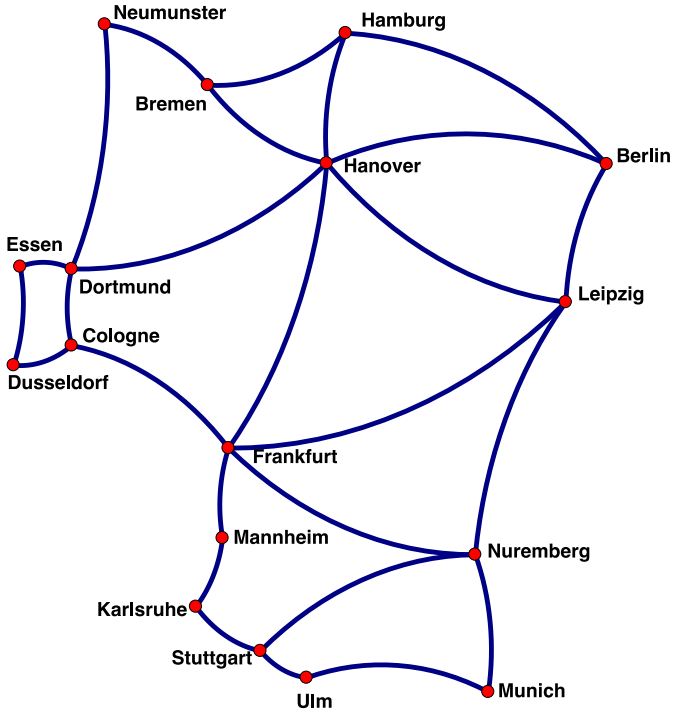

Figure B.1: The German network topology.

B.3 Parameters used for Multi-Band transmission

This section reports the propagation parameters of the SSMF used in the multi-band analysis of this thesis. In detail, Fig. B.5 reports the fiber attenuation and dispersion, Fig. B.6 reports the Raman efficiency and Table B.3 reports, for each band, the wavelength and frequency range, the central frequency, the number of spectral slots in the 50 GHz grid, the attenuation coefficient, the dispersion and the non-linear coefficient and the noise figure of each DFA.

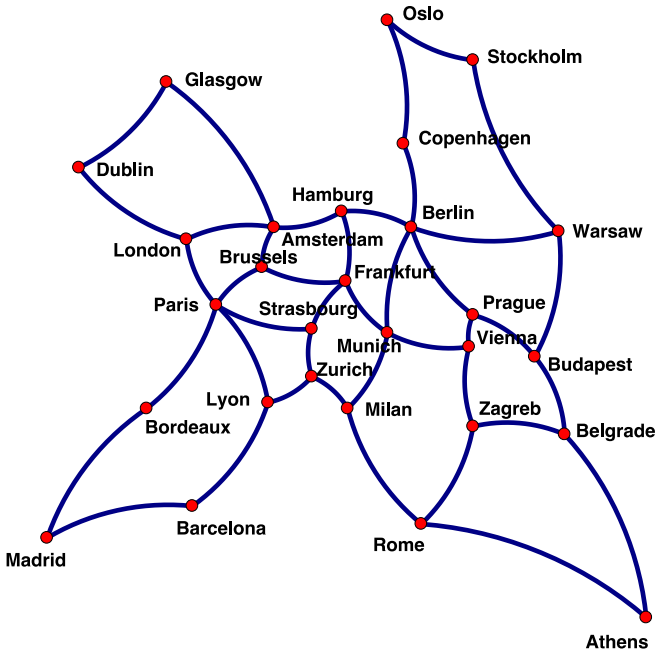

Figure B.2: The Pan-European network topology.

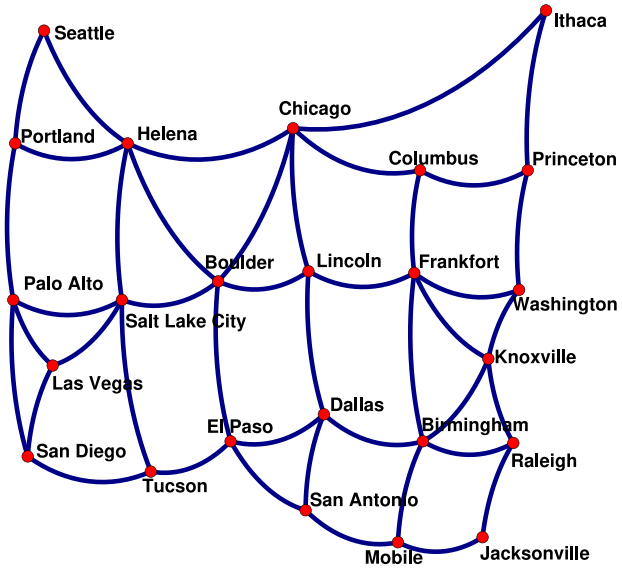

Figure B.3: The USNET network topology.

	German	Pan-European	USNET
Number of nodes	17	28	24
Number of links	26	41	43
Average node degree	3.06	3.93	3.58
Average link length	207 km	637 km	637 km
Reference figure	Fig. B.1	Fig. B.2	Fig. B.3
Source	[11]	[11]	[159]

Table B.2: Summary parameters of the network topologies.

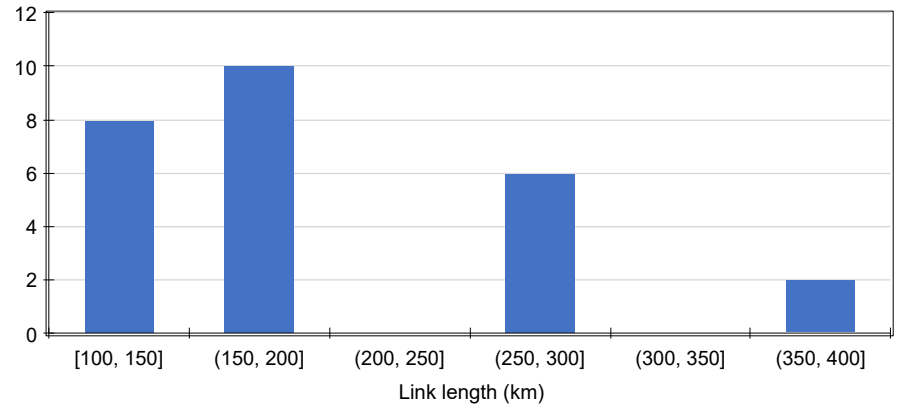

(a)

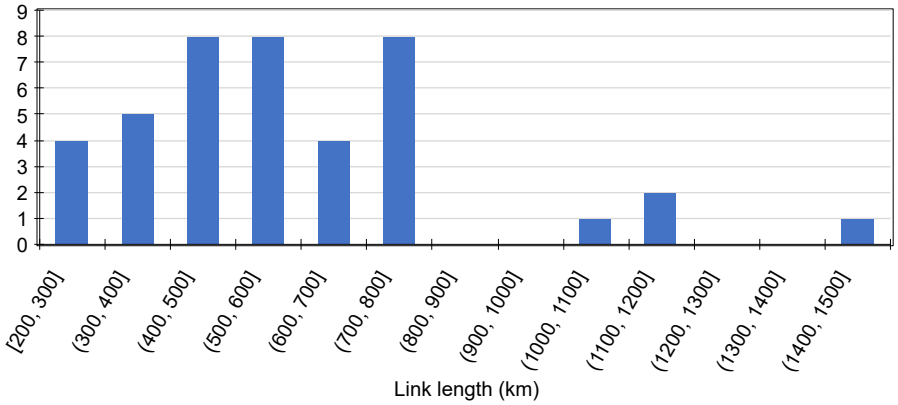

(b)

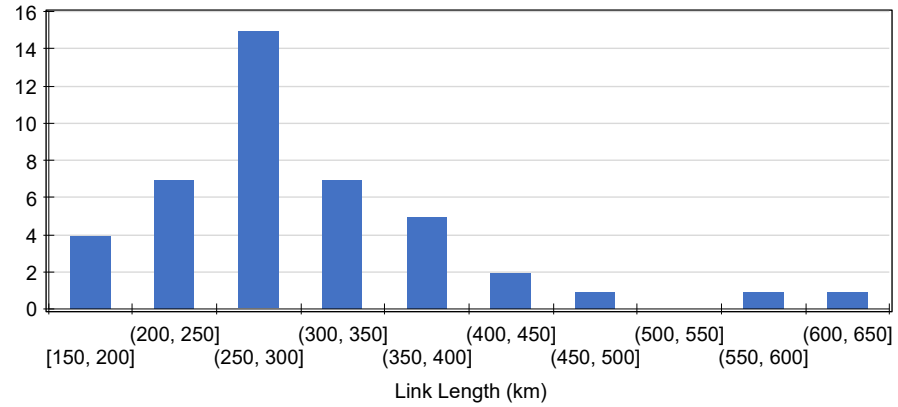

(c)

Figure B.4: The histogram of the link length for the German (a), the Pan-European (b) and the USNET (c) networks.

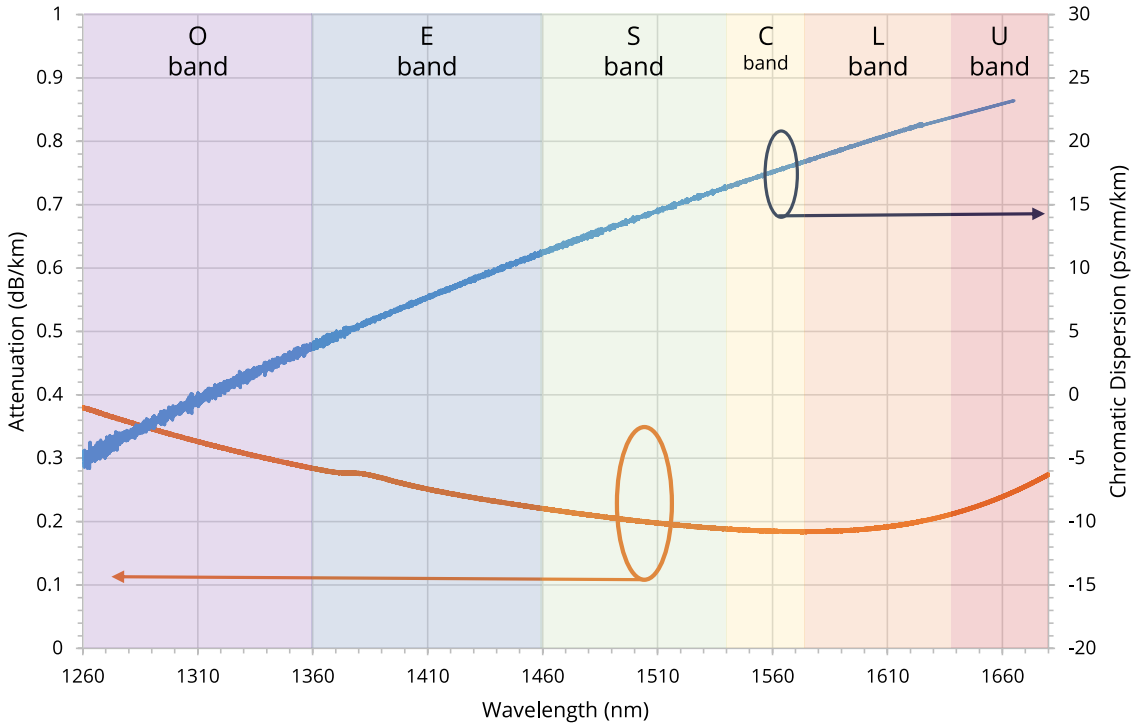

Figure B.5: Fiber attenuation and dispersion of a SSMF from 1260 nm up to 1620 nm.

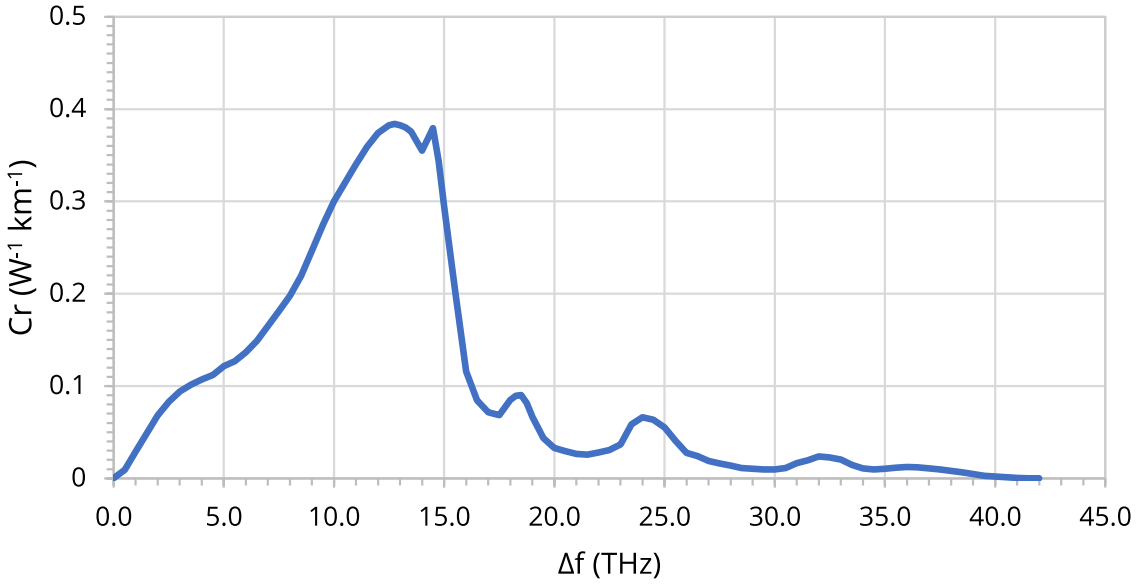

Figure B.6: Raman efficiency of SSMF.

Table B.3: Per band parameters.

	U	L	C	S	E	O
Wavelength range [nm]	1625 - 1675	1565 - 1625	1530 - 1565	1460 - 1530	1360 - 1460	1260 - 1360
Frequency range [THz]	179.10 - 184.62	184.62 - 191.69	191.69 - 196.08	196.08 - 205.48	205.48 - 220.59	220.59 - 238.10
Central Frequency [THz]	181.86	188.16	193.89	200.78	213.04	229.35
Number of available channels	108	137	80	183	296	156
Attenuation α [dB/km]	0.264	0.200	0.191	0.220	0.283	0.34
Dispersion coefficient β_2 [ps^2/km]	-30.8	-24.3	-20.2	-13.4	-4.2	-0.5
Nonlinear coefficient γ [1/W/km]	1.22	1.6	1.5	1.4	1.3	1.28
DFA noise figure [dB]	6	6	5.5	7	6	7

Bibliography

[1] Telecom Infra Project (TIP). *A new approach to building and deploying telecom network infrastructure*. https://telecominfraproject.com/.

[2] Telecom Infra Project (TIP). *The GitHub repository of GNPy*. https://github.com/Telecominfraproject/oopt-gnpy. DOI: 10.5281/zenodo.3458320.

[3] G. P. Agrawal. *Fiber-optic communication systems*. Vol. 222. John Wiley & Sons, 2012.

[4] G. P. Agrawal. "Optical communication: its history and recent progress". In: *Optics in Our Time*. Springer, Cham, 2016, pp. 177–199.

[5] Z. Alferov. "Double heterostructure lasers: early days and future perspectives". In: *IEEE Journal of Selected Topics in Quantum Electronics* 6.6 (2000), pp. 832–840. DOI: 10.1109/2944.902131.

[6] V. Alwayn. *Optical network design and implementation*. Cisco Press, 2004.

[7] C. Antonelli, M. Shtaif, and A. Mecozzi. "Modeling of nonlinear propagation in space-division multiplexed fiber-optic transmission". In: *Journal of Lightwave Technology* 34.1 (2015), pp. 36–54. DOI: 10.1109/JLT.2015.2510511.

[8] S. Aozasa et al. "Tm-doped fiber amplifiers for 1470-nm-band WDM signals". In: *IEEE Photonics Technology Letters* 12.10 (2000), pp. 1331–1333. DOI: 10.1109/68.883820.

[9] J. L. Auge, V. Curri, and E. Le Rouzic. "Open design for multi-vendor optical networks". In: *Optical Fiber Communication Conference (OFC) 2019*. Optical Society of America, 2019, Th1I.2. DOI: 10.1364/OFC.2019.Th1I.2.

[10] S. Benedetto and E. Biglieri. *Principles of digital transmission: With wireless applications*. Springer Science & Business Media, 1999.

[11] A. Betker et al. "Reference transport network scenarios". In: *MultiTeraNet Report* (2003).

[12] M. Birk et al. "The OpenROADM initiative". In: *Journal of Optical Communications and Networking* 12.6 (2020), pp. C58–C67. DOI: 10.1364/JOCN.380723.

[13] A. Bononi, O. Beucher, and P. Serena. "Single-and cross-channel nonlinear interference in the Gaussian Noise model with rectangular spectra". In: *Optics Express* 21.26 (Dec. 2013), pp. 32254–32268. DOI: 10.1364/OE.21.032254.

[14] A. Bononi et al. "Modeling nonlinearity in coherent transmissions with dominant intrachannel-four-wave-mixing". In: *Optics Express* 20.7 (Mar. 2012), pp. 7777–7791. DOI: 10.1364/OE.20.007777.

[15] J. C. Bouteiller, L. Leng, and C. Headley. "Pump-pump four-wave mixing in distributed Raman amplified systems". In: *Journal of Lightwave Technology* 22.3 (2004), pp. 723–732. DOI: 10.1109/JLT.2004.824459.

[16] *BOW: First real-world demonstration of a Bayesian optimization system for wavelength reconfiguration*. http://bow.csail.mit.edu.

[17] G. Brassard and P. Bratley. *Fundamentals of algorithmics*. Vol. 524. Prentice Hall Englewood Cliffs, 1996.

[18] J. Bromage. "Raman amplification for fiber communications systems". In: *Journal of Lightwave Technology* 22.1 (Jan. 2004), p. 79. DOI: 10.1109/OFC.2003.1247563.

[19] I. Busi and Sergio B. *YANG model for requesting path computation*. Internet-Draft `draft-ietf-teas-yang-path-computation-06`. Work in Progress. Internet Engineering Task Force, July 2019. 73 pp.

[20] A. Campanella et al. "ODTN: Open disaggregated transport network. Discovery and control of a disaggregated optical network through open source software and open APIs". In: *Optical Fiber Communications Conference and Exhibition (OFC)*. 2019, pp. 1–3. DOI: 10.1364/OFC.2019.M3Z.4.

[21] M. Cantono, J. L. Auge, and V. Curri. "Modelling the impact of SRS on NLI generation in commercial equipment: an experimental investigation". In: *Optical Fiber Communication Conference*. Optical Society of America, 2018, p. M1D.2. DOI: 10.1364/OFC.2018.M1D.2.

[22] M. Cantono, R. Gaudino, and V. Curri. "Potentialities and criticalities of flexible-rate transponders in DWDM networks: A statistical approach". In: *Journal of Optical Communications and Networking* 8.7 (2016), A76–A85. DOI: 10.1364/JOCN.8.000A76.

[23] M. Cantono et al. "Comparing networking benefits of digital back-propagation vs. lightpath regeneration". In: *European Conference on Optical Communication (ECOC)*. 2016, pp. 1–3.

[24] M. Cantono et al. "Introducing the generalized GN-model for nonlinear interference generation including space/frequency variations of loss/gain". In: *arXiv preprint arXiv:1710.02225* (2017).

[25] M. Cantono et al. "Networking benefit of hybrid fiber amplification for light-path regenerators saving". In: *Optical Fiber Communications Conference and Exhibition (OFC)*. 2017, pp. 1–3. DOI: 10.1364/OFC.2017.W4F.7.

[26] M. Cantono et al. "On the Interplay of Nonlinear Interference Generation With Stimulated Raman Scattering for QoT Estimation". In: *Journal of Lightwave Technology* 36.15 (Aug. 2018), pp. 3131–3141. DOI: 10.1109/JLT.2018.2814840.

[27] M. Cantono et al. "Opportunities and challenges of C+ L transmission systems". In: *Journal of Lightwave Technology* 38.5 (2020), pp. 1050–1060. DOI: 10.1109/JLT.2019.2959272.

[28] M. Cantono et al. "Physical layer performance of multi-band optical line systems using Raman amplification". In: *Journal of Optical Communications and Networking* 11.1 (2019), A103–A110. DOI: 10.1364/JOCN.11.00A103.

[29] R. Cardillo, V. Curri, and M. Mellia. "Considering transmission impairments in configuring wavelength routed optical networks". In: *Optical Fiber Communication Conference and the National Fiber Optic Engineers Conference*. 2006, 3 pp. DOI: 10.1109/OFC.2006.215976.

[30] A. Carena et al. "A time-domain optical transmission system simulation package accounting for nonlinear and polarization-related effects in fiber". In: *IEEE Journal on Selected Areas in Communications* 15.4 (1997), pp. 751–765. DOI: 10.1109/49.585785.

[31] A. Carena et al. "Modeling of the impact of nonlinear propagation effects in uncompensated optical coherent transmission links". In: *Journal of Lightwave Technology* 30.10 (2012), pp. 1524–1539. DOI: 10.1109/JLT.2012.2189198.

[32] *Characteristics of a non-zero dispersion-shifted single-mode optical fibre and cable*. http://handle.itu.int/11.1002/1000/10390.

[33] *Characteristics of a single-mode optical fibre and cable*. http://handle.itu.int/11.1002/1000/10389.

[34] K. Christodoulopoulos, K. Manousakis, and E. Varvarigos. "Comparison of routing and wavelength assignment algorithms in WDM networks". In: *IEEE GLOBECOM 2008 - 2008 IEEE Global Telecommunications Conference*. 2008, pp. 1–6. DOI: 10.1109/GLOCOM.2008.ECP.510.

[35] M. J. Connelly. *Semiconductor optical amplifiers*. Springer Science & Business Media, 2007.

[36] F. Cugini et al. "Toward plug-and-play software-defined elastic optical networks". In: *Journal of Lightwave Technology* 34.6 (2015), pp. 1494–1500. DOI: 10.1109/JLT.2015.2511802.

[37] V. Curri, M. Cantono, and R. Gaudino. "Elastic all-optical networks: a new paradigm enabled by the physical layer. How to optimize network performances?" In: *Journal of Lightwave Technology* 35.6 (2017), pp. 1211–1221. DOI: 10.1109/JLT.2017.2657231.

[38] V. Curri and A. Carena. "Merit of Raman pumping in uniform and uncompensated links supporting NYWDM transmission". In: *Journal of Lightwave Technology* 34.2 (2016), pp. 554–565. DOI: 10.1109/JLT.2015.2477599.

[39] V. Curri et al. "Design strategies and merit of system parameters for uniform uncompensated links supporting Nyquist-WDM transmission". In: *Journal of Lightwave Technology* 33.18 (2015), pp. 3921–3932. DOI: 10.1109/JLT.2015.2447151.

[40] R. Dar and P. J. Winzer. "On the limits of digital back-propagation in fully loaded WDM systems". In: *IEEE Photonics Technology Letters* 28.11 (2016), pp. 1253–1256. DOI: 10.1109/LPT.2016.2522969.

[41] R. Dar et al. "Accumulation of nonlinear interference noise in fiber-optic systems". In: *Optics Express* 22.12 (June 2014), pp. 14199–14211. DOI: 10.1364/OE.22.014199.

[42] *Definitions and test methods for statistical and non-linear related attributes of single-mode fibre and cable*. https://www.itu.int/rec/T-REC-G.650.2-201508-I/en.

[43] D. Derickson, C. Hentschel, and J. Vobis. *Fiber optic test and measurement*. Vol. 8. Prentice Hall PTR New Jersey, 1998.

[44] E. Desurvire and M. N. Zervas. "Erbium-doped fiber amplifiers: principles and applications". In: *Physics Today* 48.2 (1995), p. 56.

[45] E. M. Dianov. "Bismuth-doped optical fibers: a challenging active medium for near-IR lasers and optical amplifiers". In: *Light: Science & Applications* 1.5 (2012), e12–e12. DOI: https://10.1038/lsa.2012.12.

[46] C. A.S. Diniz et al. "Network cost savings enabled by probabilistic shaping in DP-16QAM 200-Gb/s systems". In: *Optical Fiber Communication Conference*. Optical Society of America. 2016, Tu3F–7. DOI: 10.1364/OFC.2016.Tu3F.7.

[47] A.F. Elrefaie et al. "Chromatic dispersion limitations in coherent lightwave transmission systems". In: *Journal of Lightwave Technology* 6.5 (1988), pp. 704–709. DOI: 10.1109/50.4056.

[48] D. J. Elson et al. "Investigation of bandwidth loading in optical fibre transmission using amplified spontaneous emission noise". In: *Optics Express* 25.16 (Aug. 2017), pp. 19529–19537. DOI: 10.1364/OE.25.019529.

[49] R. Enns et al. “Rfc 6241, network configuration protocol (NETCONF)”. In: *Internet Engineering Task Force (IETF), June* (2011).

[50] R. Essiambre and R. W. Tkach. “Capacity trends and limits of optical communication networks”. In: *Proceedings of the IEEE* 100.5 (2012), pp. 1035–1055. DOI: 10.1109/JPROC.2012.2182970.

[51] *Exchange with GNPy to check path feasibility.* https://git.opendaylight.org/gerrit/c/transportpce/+/81785.

[52] A. Ferrari, M. Cantono, and V. Curri. “A networking comparison between multicore fiber and fiber ribbon in WDM-SDM optical networks”. In: *European Conference on Optical Communication (ECOC)*. 2018, pp. 1–3. DOI: 10.1109/ECOC.2018.8535450.

[53] A. Ferrari, M. Cantono, and V. Curri. “Coupled vs. uncoupled SDM solutions: A physical layer aware networking comparison”. In: *20th International Conference on Transparent Optical Networks (ICTON)*. IEEE. 2018, pp. 1–4. DOI: 10.1109/ICTON.2018.8473701.

[54] A. Ferrari, M. Cantono, and V. Curri. “Networking benefits of advanced DSP techniques”. In: *19th Italian National Conference on Photonic Technologies (Fotonica 2017)*. 2017, pp. 1–4. DOI: 10.1049/cp.2017.0182.

[55] A. Ferrari, E. Virgillito, and V. Curri. “Band-division vs. space-division multiplexing: A network performance statistical assessment”. In: *Journal of Lightwave Technology* 38.5 (2020), pp. 1041–1049. DOI: 10.1109/JLT.2020.2970484.

[56] A. Ferrari, E. Virgillito, and V. Curri. “Networking merit of spatial-division and band-division multiplexing: A statistical assessment”. In: *22nd International Conference on Transparent Optical Networks (ICTON)*. IEEE. 2020, pp. 1–4. DOI: 10.1109/ICTON51198.2020.9203172.

[57] A. Ferrari et al. “A two-layer network solution for reliable and efficient host-to-host transfer of big data”. In: *20th International Conference on Transparent Optical Networks (ICTON)*. 2018, pp. 1–4. DOI: 10.1109/ICTON.2018.8473597.

[58] A. Ferrari et al. “Assessment on the achievable throughput of multi-band ITU-T G.652.D fiber transmission systems”. In: *Journal of Lightwave Technology* 38.16 (2020), pp. 4279–4291. DOI: 10.1109/JLT.2020.2989620.

[59] A. Ferrari et al. “Assessment on the in-field lightpath QoT computation including connector loss uncertainties”. In: *Journal of Optical Communications and Networking* 13.2 (Feb. 2021), A156–A164. DOI: 10.1364/JOCN.402969.

[60] A. Ferrari et al. “Experimental validation of an open source quality of transmission estimator for open optical networks”. In: *Optical Fiber Communications Conference and Exhibition (OFC)*. 2020, pp. 1–3. DOI: 10.1364/OFC.2020.W3C.2.

[61] A. Ferrari et al. “GNPy: an open source application for physical layer aware open optical networks”. In: *Journal of Optical Communications and Networking* 12.6 (2020), pp. C31–C40. DOI: 10.1364/JOCN.382906.

[62] A. Ferrari et al. “Networking benefits of advanced DSP techniques and hybrid fiber amplification”. In: *19th International Conference on Transparent Optical Networks (ICTON)*. 2017, pp. 1–4. DOI: 10.1109/ICTON.2017.8025170.

[63] A. Ferrari et al. “Physical layer strategies to save lightpath regenerators”. In: *Journal of Optical Communications and Networking* 10.9 (2018), pp. 703–711. DOI: 10.1364/JOCN.10.000703.

[64] A. Ferrari et al. “Power Control Strategies in C+L Optical Line Systems”. In: *Optical Fiber Communications Conference and Exhibition (OFC)*. 2019, pp. 1–3. DOI: 10.1364/OFC.2019.W2A.48.

[65] A. Ferrari et al. “Selection of amplifier upgrades addressed by quality of transmission and routing space”. In: *Optical Fiber Communications Conference and Exhibition (OFC)*. 2019, pp. 1–3. DOI: 10.1364/OFC.2019.M2E.5.

[66] A. Ferrari et al. “Softwarized optical transport QoT in production optical network: A brownfield validation”. In: *European Conference on Optical Communications (ECOC)*. 2020, pp. 1–4. DOI: 10.1109/ECOC48923.2020.9333280.

[67] A. Ferrari et al. “Upgrade capacity scenarios enabled by multi-band optical systems”. In: *21st International Conference on Transparent Optical Networks (ICTON)*. 2019, pp. 1–4. DOI: 10.1109/ICTON.2019.8840550.

[68] H. Fevrier et al. “Facebook perspective on submarine wet plant evolution”. In: *Optical Fiber Communications Conference and Exhibition (OFC)*. 2019, pp. 1–3. DOI: 10.1364/OFC.2019.M2E.4.

[69] R. T. Fielding and R. N. Taylor. *Architectural styles and the design of network-based software architectures*. Vol. 7. University of California, Irvine Doctoral dissertation, 2000.

[70] M. Filer et al. “Multi-Vendor experimental validation of an open source QoT estimator for optical networks”. In: *Journal of Lightwave Technology* 36.15 (2018), pp. 3073–3082. DOI: 10.1109/JLT.2018.2818406.

[71] J. K. Fischer et al. "Maximizing the capacity of installed optical fiber infrastructure via wideband transmission". In: *20th International Conference on Transparent Optical Networks (ICTON)*. 2018, pp. 1–4. DOI: 10.1109/ICTON.2018.8473994.

[72] M. Flammini et al. "On the complexity of the regenerator placement problem in optical networks". In: *IEEE/ACM Transactions on Networking* 19.2 (2011), pp. 498–511. DOI: 10.1109/TNET.2010.2068309.

[73] I. E. Fonseca et al. "Algorithms for FWM-aware routing and wavelength assignment". In: *Proceedings of the 2003 SBMO/IEEE MTT-S International Microwave and Optoelectronics Conference - IMOC 2003. (Cat. No.03TH8678)*. Vol. 2. 2003, 707–712 vol.2. DOI: 10.1109/IMOC.2003.1242665.

[74] R. Freund et al. "Triple-(S/C/L)-band WDM transmission using erbium-doped fibre amplifiers". In: *European Conference on Optical Communication (ECOC)*. Vol. 1. 2005, 69–70 vol.1. DOI: 10.1049/cp:20050382.

[75] D.-S. Ly-Gagnon et al. "Coherent detection of optical quadrature phase-shift keying signals with carrier phase estimation". In: *Journal of Lightwave Technology* 24.1 (2006), pp. 12–21. DOI: 10.1109/JLT.2005.860477.

[76] A. Giorgetti et al. "Control of open and disaggregated transport networks using the Open Network Operating System (ONOS)". In: *Journal of Optical Communications and Networking* 12.2 (2020), A171–A181. DOI: 10.1364/JOCN.12.00A171.

[77] A. H. Gnauck, R. M. Jopson, and P. J. Winzer. "Demonstration of counter-propagating Raman pump placed near signal-channel wavelengths". In: *IEEE Photonics Technology Letters* 29.1 (2017), pp. 154–157. DOI: 10.1109/LPT.2016.2630603.

[78] J. P. Gordon and H. Kogelnik. "PMD fundamentals: Polarization mode dispersion in optical fibers". In: *Proceedings of the National Academy of Sciences* 97.9 (2000), pp. 4541–4550. ISSN: 0027-8424. DOI: 10.1073/pnas.97.9.4541. eprint: https://www.pnas.org/content/97/9/4541.full.pdf. URL: https://www.pnas.org/content/97/9/4541.

[79] G. Grammel, V. Curri, and J.-L. Auge. "Physical simulation environment of the Telecommunications Infrastructure Project (TIP)". In: *Optical Fiber Communications Conference and Exposition (OFC)*. 2018, pp. 1–3. DOI: 10.1364/OFC.2018.M1D.3.

[80] A. Hagberg, P. Swart, and D. Chult. "Exploring network structure, dynamics, and function using networkX". In: (Jan. 2008).

[81] P.B. Hansen et al. "Rayleigh scattering limitations in distributed Raman pre-amplifiers". In: *IEEE Photonics Technology Letters* 10.1 (1998), pp. 159–161. DOI: 10.1109/68.651148.

[82] I. Hayashi et al. “Junction lasers which operate continuously at room temperature”. In: *Applied Physics Letters* 17.3 (1970), pp. 109–111. DOI: 10.1063/1.1653326.

[83] D. Hicks et al. “PROnet: A programmable optical network prototype”. In: *18th International Conference on Transparent Optical Networks (ICTON)*. 2016, pp. 1–4. DOI: 10.1109/ICTON.2016.7550421.

[84] Y. Hsueh et al. “Passband narrowing and crosstalk impairments in ROADM-enabled 100G DWDM networks”. In: *Journal of Lightwave Technology* 30.24 (2012), pp. 3980–3986. DOI: 10.1109/JLT.2012.2208262.

[85] *IEEE standards association, Link Layer Discovery Protocol*. http://standards.ieee.org/getieee802/download/802.1AB-2009.pdf.

[86] E. Ip and J. M. Kahn. “Digital equalization of chromatic dispersion and polarization mode dispersion”. In: *Journal of Lightwave Technology* 25.8 (Aug. 2007), pp. 2033–2043. DOI: 10.1109/JLT.2007.900889. URL: http://jlt.osa.org/abstract.cfm?URI=jlt-25-8-2033.

[87] D. J. Ives, P. Bayvel, and S. J. Savory. “Adapting transmitter power and modulation format to improve optical network performance utilizing the Gaussian noise model of monlinear impairments”. In: *Journal of Lightwave Technology* 32.21 (Nov. 2014), pp. 3485–3494.

[88] P. Johannisson and E. Agrell. “Modeling of nonlinear signal distortion in fiber-optic networks”. In: *Journal of Lightwave Technology* 32.23 (2014), pp. 4544–4552. DOI: 10.1109/JLT.2014.2361357.

[89] P. Johannisson and M. Karlsson. “Perturbation analysis of nonlinear propagation in a strongly dispersive optical communication system”. In: *Journal of Lightwave Technology* 31.8 (2013), pp. 1273–1282. DOI: 10.1109/JLT.2013.2246543.

[90] R. Jones. *Claude*. https://github.com/Rassibassi/claude.

[91] V. Kamalov et al. “Lessons learned from open line system deployments”. In: *Optical Fiber Communications Conference and Exhibition (OFC)*. IEEE. 2017, pp. 1–3.

[92] V. Kamalov et al. “The subsea fiber as a Shannon channel”. In: *Proceedings of the SubOptic*. 2019.

[93] K. C. Kao and George A. Hockham. “Dielectric-fibre surface waveguides for optical frequencies”. In: *Proceedings of the Institution of Electrical Engineers*. Vol. 113. 7. IET. 1966, pp. 1151–1158.

[94] F. P. Kapron, D. B. Keck, and R. D. Maurer. “Radiation losses in glass optical waveguides”. In: *Applied Physics Letters* 17.10 (1970), pp. 423–425. DOI: 10.1063/1.1653255.

[95] J. Kerr. "A new relation between electricity and light: Dielectrified media birefringent". In: *The London, Edinburgh, and Dublin Philosophical Magazine and Journal of Science* 50.332 (1875), pp. 337–348.

[96] J. Kerr. "A new relation between electricity and light: Dielectrified media birefringent (second paper)". In: *The London, Edinburgh, and Dublin Philosophical Magazine and Journal of Science* 50.333 (1875), pp. 446–458.

[97] Z. K. Khattak, M. Awais, and A. Iqbal. "Performance evaluation of OpenDaylight SDN controller". In: *20th IEEE international conference on parallel and distributed systems (ICPADS)*. IEEE. 2014, pp. 671–676. DOI: 10.1109/PADSW.2014.7097868.

[98] K. Kikuchi. "Fundamentals of coherent optical fiber communications". In: *Journal of Lightwave Technology* 34.1 (2016), pp. 157–179. DOI: 10.1109/JLT.2015.2463719.

[99] H. Kogelnik, R. M. Jopson, and L. E. Nelson. "Polarization-mode dispersion". In: *Optical Fiber Telecommunications IV-B (Fourth Edition)*. Ed. by Ivan P. Kaminow and Tingye Li. Fourth Edition. Optics and Photonics. Burlington: Academic Press, 2002, pp. 725–861. DOI: 10.1016/B978-012395173-1/50015-3.

[100] J. Kundrát et al. "Opening up ROADMs: Let us build a disaggregated open optical line system". In: *Journal of Lightwave Technology* 37.16 (Aug. 2019), pp. 4041–4051. ISSN: 0733-8724. DOI: 10.1109/JLT.2019.2906620.

[101] J. Kundrát et al. "Physical-layer awareness: GNPy and ONOS for end-to-end circuits in disaggregated networks". In: *Optical Fiber Communications Conference and Exhibition (OFC)*. 2020, pp. 1–3. DOI: 10.1364/OFC.2020.M3Z.17.

[102] Y. Li et al. "tSDX: enabling impairment-aware all-optical inter-domain exchange". In: *Journal of Lightwave Technology* 36.1 (2017), pp. 142–154. DOI: 10.1109/JLT.2017.2761355.

[103] V. Lopez et al. "Optimized design and challenges for C&L band optical line systems". In: *Journal of Lightwave Technology* 38.5 (2020), pp. 1080–1091. DOI: 10.1109/JLT.2020.2968225.

[104] D. Marcuse, C.R. Manyuk, and P.K.A. Wai. "Application of the Manakov-PMD equation to studies of signal propagation in optical fibers with randomly varying birefringence". In: *Journal of Lightwave Technology* 15.9 (1997), pp. 1735–1746. DOI: 10.1109/50.622902.

[105] D. M. Marom and M. Blau. "Switching solutions for WDM-SDM optical networks". In: *IEEE Communications Magazine* 53.2 (2015), pp. 60–68. DOI: 10.1109/MCOM.2015.7045392.

[106] H. Masuda. "Recent progress on optical fiber amplifiers and their applications". In: *Active and Passive Optical Components for Communications VI*. Ed. by Achyut K. Dutta et al. Vol. 6389. International Society for Optics and Photonics. SPIE, 2006, pp. 8–17. DOI: 10.1117/12.687334.

[107] S. Matsuo et al. "High-spatial-multiplicity multicore fibers for future dense space-division-multiplexing systems". In: *Journal of Lightwave Technology* 34.6 (2015), pp. 1464–1475. DOI: 10.1109/JLT.2015.2508928.

[108] A. Mecozzi and M. Shtaif. "The statistics of polarization-dependent loss in optical communication systems". In: *IEEE Photonics Technology Letters* 14.3 (2002), pp. 313–315. DOI: 10.1109/68.986797.

[109] J. Medved et al. "OpenDaylight: Towards a model-driven SDN controller architecture". In: *Proceeding of IEEE International Symposium on a World of Wireless, Mobile and Multimedia Networks 2014*. 2014, pp. 1–6. DOI: 10.1109/WoWMoM.2014.6918985.

[110] S. Melle et al. "Alien wavelength transport: An operational and economic analysis". In: *National Fiber Optic Engineers Conference*. Optical Society of America. 2009, NThF2. DOI: 10.1364/NFOEC.2009.NThF2.

[111] B. Mirkhanzadeh et al. "Demonstration of an SDN orchestrator for both flow provisioning and fault handling in an Ethernet-over-WDM Network". In: *19th International Conference on Transparent Optical Networks (ICTON)*. 2017, pp. 1–4. DOI: 10.1109/ICTON.2017.8024936.

[112] A. Mitra et al. "Effect of channel launch power on fill margin in C+L band elastic optical networks". In: *Journal of Lightwave Technology* 38.5 (2020), pp. 1032–1040. DOI: 10.1109/JLT.2019.2952876.

[113] T. Miya et al. "Ultimate low-loss single-mode fibre at 1.55 μm". In: *Electronics Letters* 15.4 (1979), pp. 106–108.

[114] T. Naito et al. "A broadband distributed Raman amplifier for bandwidths beyond 100 nm". In: *Optical Fiber Communication Conference and Exhibit*. 2002, pp. 116–117. DOI: 10.1109/OFC.2002.1036244.

[115] A. Napoli et al. "Towards multiband optical systems". In: *Photonic Networks and Devices*. Optical Society of America, 2018, NeTu3E.1. DOI: 10.1364/NETWORKS.2018.NeTu3E.1.

[116] A. Nespola et al. "Extensive fiber comparison and GN-model validation in uncompensated links using DAC-generated Nyquist-WDM PM-16QAM channels". In: *Optical Fiber Communication Conference and Exposition and the National Fiber Optic Engineers Conference (OFC/NFOEC)*. 2013, pp. 1–3. DOI: 10.1364/OFC.2013.OTh3G.5.

[117] A. Nespola et al. “GN-model validation over seven fiber types in uncompensated PM-16QAM Nyquist-WDM links”. In: *IEEE Photonics Technology Letters* 26.2 (2014), pp. 206–209. DOI: 10.1109/LPT.2013.2292330.

[118] *Nippon telegraph and telephone corporation, RYU network operating system*. http://osrg.github.com/ryu.

[119] S. Okamoto et al. “A study on the effect of ultra-wide band WDM on optical transmission systems”. In: *Journal of Lightwave Technology* 38.5 (2020), pp. 1061–1070. DOI: 10.1109/JLT.2019.2962178.

[120] ONF. *Software-defined networking: the new norm for networks*. white paper.

[121] OpenConfig. *Vendor-neutral, model-driven network management designed by users*. http://openconfig.net.

[122] A. E. Ozdaglar and D. P. Bertsekas. “Routing and wavelength assignment in optical networks”. In: *IEEE/ACM Transactions on Networking* 11.2 (2003), pp. 259–272. DOI: 10.1109/TNET.2003.810321.

[123] J. Pan et al. “Comparison of ROADM filter shape models for accurate transmission penalty assessment”. In: *IEEE Photonics Conference (IPC)*. 2016, pp. 550–551. DOI: 10.1109/IPCon.2016.7831225.

[124] P. Papanikolaou, K. Christodoulopoulos, and E. Varvarigos. “Multilayer flexgrid network planning”. In: *International Conference on Optical Network Design and Modeling (ONDM)*. 2015, pp. 151–156. DOI: 10.1109/ONDM.2015.7127290.

[125] P. Papanikolaou et al. “Minimizing energy and cost in fixed-grid and flexgrid networks”. In: *Journal of Optical Communications and Networking* 7.4 (Apr. 2015), pp. 337–351. DOI: 10.1364/JOCN.7.000337.

[126] D.F. Parker and G.K. Newboult. “Coupled nonlinear Schrödinger equations arising in fibre optics”. In: *Le Journal de Physique Colloques* 50.C3 (1989), pp. C3–137. DOI: 10.1051/jphyscol:1989322.

[127] R. Pastorelli et al. “Network planning strategies for next-generation flexible optical networks”. In: *Journal of Optical Communications and Networking* 7.3 (2015), A511–A525. DOI: 10.1364/JOCN.7.00A511.

[128] F. Pederzolli et al. “Improving performance of spatially joint-switched space division multiplexing optical networks via spatial group sharing”. In: *Journal of Optical Communications and Networking* 9.3 (2017), B1–B11. DOI: 10.1364/JOCN.9.0000B1.

[129] D. Pilori. *DSP library*. https://github.com/dario-pilori/dsp-library.

[130] D. Pilori et al. “FFSS: The fast fiber simulator software”. In: *19th International Conference on Transparent Optical Networks (ICTON)*. 2017, pp. 1–4. DOI: 10.1109/ICTON.2017.8025002.

[131] D. Pilori et al. “Non-linear phase noise mitigation over systems using constellation shaping”. In: *Journal of Lightwave Technology* 37.14 (2019), pp. 3475–3482. DOI: 10.1109/JLT.2019.2917308.

[132] E. Pincemin et al. “Raman gain efficiencies of modern terrestrial transmission fibers in S-, C- and L-band”. In: *Nonlinear Guided Waves and Their Applications*. Optical Society of America, 2002, NLTuC2. DOI: 10.1364/NLGW.2002.NLTuC2.

[133] P. Poggiolini. “The GN model of non-linear propagation in uncompensated coherent optical systems”. In: *Journal of Lightwave Technology* 30.24 (Dec. 2012), pp. 3857–3879. DOI: 10.1109/JLT.2012.2217729.

[134] P. Poggiolini and Y. Jiang. “Recent advances in the modeling of the impact of nonlinear fiber propagation effects on uncompensated coherent transmission systems”. In: *Journal of Lightwave Technology* 35.3 (Feb. 1, 2017), pp. 458–480. ISSN: 0733-8724, 1558-2213. DOI: 10.1109/JLT.2016.2613893.

[135] P. Poggiolini et al. “Analytical modeling of nonlinear propagation in uncompensated optical transmission links”. In: *IEEE Photonics Technology Letters* 23.11 (2011), pp. 742–744. DOI: 10.1109/LPT.2011.2131125.

[136] P. Poggiolini et al. “The GN-Model of Fiber Non-Linear Propagation and Its Applications”. In: *Journal of Lightwave Technology* 32.4 (Feb. 2014), pp. 694–721. ISSN: 0733-8724, 1558-2213. DOI: 10.1109/JLT.2013.2295208.

[137] P. Poggiolini et al. “The GN-model of fiber non-linear propagation and its applications”. In: *Journal of Lightwave Technology* 32.4 (2014), pp. 694–721. DOI: 10.1109/JLT.2013.2295208.

[138] P. Poggiolini et al. “The LOGON strategy for low-complexity control plane implementation in new-generation flexible networks”. In: *Optical Fiber Communication Conference and Exposition and the National Fiber Optic Engineers Conference (OFC/NFOEC)*. 2013, pp. 1–3. DOI: 10.1364/OFC.2013.OW1H.3.

[139] *Project Floodlight*. http://floodlight.openflowhub.org.

[140] A. G. Rahbar. “Review of dynamic impairment-aware routing and wavelength assignment techniques in all-optical wavelength-routed networks”. In: *IEEE Communications Surveys Tutorials* 14.4 (2012), pp. 1065–1089. DOI: 10.1109/SURV.2011.101911.00023.

[141] T. Rahman et al. “On the mitigation of optical filtering penalties originating From ROADM cascade”. In: *IEEE Photonics Technology Letters* 26.2 (2014), pp. 154–157. DOI: 10.1109/LPT.2013.2290745.

[142] C. V. Raman. “A new radiation”. In: *Indian Journal of physics* 2 (1928), pp. 387–398.

[143] I. Recommendation. "G. 694.1 Spectral grids for WDM applications: DWDM frequency grid". In: *International Telecommunications Union, Tech. Rep* (2012).

[144] J. Renaudier. "100nm ultra-wideband optical fiber transmission systems using semiconductor optical amplifiers". In: *European Conference on Optical Communication (ECOC)*. 2018, pp. 1–3. DOI: 10.1109/ECOC.2018.8535354.

[145] J. Renaudier et al. "First 100-nm continuous-band WDM transmission system with 115Tb/s transport over 100km using novel ultra-wideband semiconductor optical amplifiers". In: *European Conference on Optical Communication (ECOC)*. 2017, pp. 1–3. DOI: 10.1109/ECOC.2017.8346084.

[146] J. Renaudier et al. "Recent advances in 100+nm ultra-wideband fiber-optic transmission systems using semiconductor optical amplifiers". In: *Journal of Lightwave Technology* 38.5 (2020), pp. 1071–1079. DOI: 10.1109/JLT.2020.2966491.

[147] I. Roberts et al. "Channel power optimization of WDM systems following Gaussian noise nonlinearity model in presence of stimulated Raman scattering". In: *Journal of Lightwave Technology* 35.23 (Dec. 2017), pp. 5237–5249. DOI: 10.1109/JLT.2017.2771719.

[148] J. B. Rosolem et al. "S-C-L triple-band double-pass Erbium-doped silica fiber amplifier with an embedded DCF module for CWDM applications". In: *Journal of lightwave technology* 24.10 (Oct. 2006), pp. 3691–3697. DOI: 10.1109/JLT.2006.881846.

[149] R. Rumipamba-Zambrano et al. "Assessment of flex-grid/MCF optical networks with ROADM limited core switching capability". In: *International Conference on Optical Network Design and Modeling (ONDM)*. IEEE. 2017, pp. 1–6. DOI: 10.23919/ONDM.2017.7958556.

[150] R. Ryf et al. "Long-distance transmission over coupled-core multicore fiber". In: *European Conference on Optical Communication (ECOC)*. VDE. 2016, pp. 1–3.

[151] Jochen S. and Mikael M. *QAMPy a DSP chain for optical communications*. https://github.com/ChalmersPhotonicsLab/QAMpy. DOI: 10.5281/zenodo.1195720.

[152] A. M. Saleh and J. Simmons. "All-optical networking-evolution, benefits, challenges, and future vision". In: *Proceedings of the IEEE* 100.5 (2012), pp. 1105–1117. DOI: 10.1109/JPROC.2011.2182589.

[153] S. J. Savory. "Approximations for the nonlinear self-channel interference of channels with rectangular spectra". In: *IEEE Photonics Technology Letters* 25.10 (2013), pp. 961–964. DOI: 10.1109/LPT.2013.2255869.

[154] S.J. Savory. "Digital coherent optical receivers: Algorithms and subsystems". In: *IEEE Journal of Selected Topics in Quantum Electronics* 16.5 (2010), pp. 1164–1179. DOI: 10.1109/JSTQE.2010.2044751.

[155] D. Semrau, R. I Killey, and P. Bayvel. "A closed-form approximation of the Gaussian noise model in the presence of inter-channel stimulated Raman scattering". In: *Journal of Lightwave Technology* 37.9 (2019), pp. 1924–1936. DOI: 10.1109/JLT.2019.2895237.

[156] D. Semrau, R. I Killey, and P. Bayvel. "The Gaussian noise model in the presence of inter-channel stimulated Raman scattering". In: *Journal of Lightwave Technology* 36.14 (July 2018), pp. 3046–3055. DOI: 10.1109/JLT.2018.2830973.

[157] D. Semrau et al. *Implementation of the ISRS GN model*. https://github.com/dsemrau/ISRSGNmodel. 2019.

[158] S. Sezer et al. "Are we ready for SDN? Implementation challenges for software-defined networks". In: *IEEE Communications Magazine* 51.7 (2013), pp. 36–43. DOI: 10.1109/MCOM.2013.6553676.

[159] G. Shen and R. S. Tucker. "Energy-minimized design for IP over WDM networks". In: *Journal of Optical Communications and Networking* 1.1 (2009), pp. 176–186. DOI: 10.1364/JOCN.1.000176.

[160] G. Shen et al. "Efficient heuristic algorithms for light-path routing and wavelength assignment in WDM networks under dynamically varying loads". In: *Computer Communications* 24.3 (2001), pp. 364–373. ISSN: 0140-3664. DOI: 10.1016/S0140-3664(00)00236-X.

[161] J. Simmons. "A Closer Look at ROADM Contention". In: *IEEE Communications Magazine* 55.2 (2017), pp. 160–166. DOI: 10.1109/MCOM.2017.1600829CM.

[162] J. M. Simmons. *Optical network design and planning*. Springer, 2014.

[163] K. Slavicek and V. Novak. "Introduction of alien wavelength into Cesnet DWDM backbone". In: *6th International Conference on Information, Communications & Signal Processing*. IEEE. 2007, pp. 1–5. DOI: 10.1109/ICICS.2007.4449739.

[164] I. Szczesniak, A. Jajszczyk, and B. Wozna-Szczesniak. "Generic Dijkstra for optical networks". In: *Journal of Optical Communications and Networking* 11.11 (2019), pp. 568–577. DOI: 10.1364/JOCN.11.000568.

[165] T. Takagi et al. "Algorithms for maximizing spectrum efficiency in elastic optical path networks that adopt distance adaptive modulation". In: *European Conference on Optical Communication (ECOC)*. 2010, pp. 1–3. DOI: 10.1109/ECOC.2010.5621146.

[166] M. A. Taubenblatt. "Optical interconnects for high performance computing". In: *IEEE Photonic Society 24th Annual Meeting*. 2011, pp. 668–669. DOI: 10.1109/PHO.2011.6110726.

[167] B. Taylor et al. "Towards a route planning tool for open optical networks in the Telecom Infrastructure Project". In: *Optical Fiber Communications Conference and Exposition (OFC)*. 2018, pp. 1–3. DOI: 10.1364/OFC.2018.Tu3E.4.

[168] M.G. Taylor. "Coherent detection method using DSP for demodulation of signal and subsequent equalization of propagation impairments". In: *IEEE Photonics Technology Letters* 16.2 (2004), pp. 674–676. DOI: 10.1109/LPT.2003.823106.

[169] *The Links foundation website*. http://linksfoundation.com.

[170] *The OpNeAR web page*. https://opnear.utdallas.edu.

[171] S. Tibuleac and M. Filer. "Transmission impairments in DWDM networks with reconfigurable optical add-drop multiplexers". In: *Journal of Lightwave Technology* 28.4 (2010), pp. 557–598. DOI: 10.1109/JLT.2009.2037832.

[172] D. Ventorini et al. "Demonstration and evaluation of IP-over-DWDM networking as "alien-wavelength" over existing carrier DWDM infrastructure". In: *National Fiber Optic Engineers Conference*. Optical Society of America. 2008, NME3. DOI: 10.1109/OFC.2008.4528272.

[173] J. López Vizcaíno, Y. Ye, and I. Tafur Monroy. "Energy efficiency analysis for flexible-grid OFDM-based optical networks". In: *Computer Networks* 56.10 (2012). Green communication networks, pp. 2400–2419. ISSN: 1389-1286. DOI: 10.1016/j.comnet.2012.03.012.

[174] V. Vusirikala et al. "Scalable and flexible transport networks for inter-datacenter connectivity". In: *Optical Fiber Communications Conference and Exhibition (OFC)*. IEEE. 2015, pp. 1–3. DOI: 10.1364/OFC.2015.Tu3H.1.

[175] S. Walker. "Rapid modeling and estimation of total spectral loss in optical fibers". In: *Journal of Lightwave Technology* 4.8 (1986), pp. 1125–1131. DOI: 10.1109/JLT.1986.1074874.

[176] R. Wallner and R. Cannistra. "An SDN approach: quality of service using big switch's floodlight open-source controller". In: *Proceedings of the Asia-Pacific Advanced Network* 35.14-19 (2013), pp. 10–7125.

[177] A. Wang et al. "Network virtualization: Technologies, perspectives, and frontiers". In: *Journal of Lightwave Technology* 31.4 (2013), pp. 523–537. DOI: 10.1109/JLT.2012.2213796.

[178] G. Wellbrock and T. J. Xia. "How will optical transport deal with future network traffic growth?" In: *European Conference on Optical Communication (ECOC)*. 2014, pp. 1–3. DOI: 10.1109/ECOC.2014.6964248.

[179] P. J. Winzer. "Optical networking beyond WDM". In: *IEEE Photonics Journal* 4.2 (2012), pp. 647–651. DOI: 10.1109/JPHOT.2012.2189379.

[180] Y. Xiong et al. "Lightpath management in SDN-based elastic optical networks With power consumption considerations". In: *Journal of Lightwave Technology* 36.9 (May 2018), pp. 1650–1660. DOI: 10.1109/JLT.2017.2785410.

[181] T. Xu et al. "Chromatic dispersion compensation in coherent transmission system using digital filters". In: *Optics Express* 18.15 (July 2010), pp. 16243–16257. DOI: 10.1364/OE.18.016243.

[182] Y. Xu, E. Agrell, and M. Brandt-Pearce. "Cross-layer static resource provisioning for dynamic traffic in flexible grid optical networks". In: *Journal of Optical Communications and Networking* 13.3 (Mar. 2021), pp. 1–13. DOI: 10.1364/JOCN.404693.

[183] L. Yan et al. "Robust regenerator allocation in nonlinear flexible-grid optical networks with time-varying data rates". In: *Journal of Optical Communications and Networking* 10.11 (2018), pp. 823–831. DOI: 10.1364/JOCN.10.000823.

[184] S. Yan et al. "Field trial of machine-learning-assisted and SDN-based optical network planning with network-scale monitoring database". In: *European Conference on Optical Communication (ECOC)*. IEEE. 2017, pp. 1–3. DOI: 10.1109/ECOC.2017.8346091.

[185] Z. Zhong et al. "BOW: First real-world demonstration of a Bayesian optimization system for wavelength reconfiguration". In: *Optical Fiber Communications Conference and Exhibition (OFC)*. 2021.

This Ph.D. thesis has been typeset by means of the TEX-system facilities. The typesetting engine was pdfLATEX. The document class was `toptesi`, by Claudio Beccari, with option `tipotesi=scudo`. This class is available in every up-to-date and complete TEX-system installation.